SLAC-J-ICFA-22
Spring 2001
SLAC-R-653

HOME PAGE

http://www.slac.stanford.edu/pubs/icfa/

ICFA INSTRUMENTATION BULLETIN*

The publication of the ICFA Instrumentation Bulletin is an activity of the Panel on Future Innovation and Development of ICFA (International Committee for Future Accelerators).

Volume 22

Spring 2001 Issue

* Supported by the Department of Energy, contract DE-AC03-76SF00515.

ICFA INSTRUMENTATION BULLETIN

The publication of the ICFA Instrumentation Bulletin is an activity of the Panel on Future Innovation and Development of ICFA (International Committee for Future Accelerators). The Bulletin reports on research and progress in the field of instrumentation with emphasis on application in the field of high-energy physics. It encourages issues of generic instrumentation.

Publisher : Stanford Linear Accelerator Center
SLAC Publications Department
Stanford, CA 94309, U.S.A.

Editor : J. Va'vra

Web Technical Advisers : J. Schwiening

The views expressed in this Bulletin do not necessarily represent those of the ICFA Panel or the editor. In all cases, the authors are responsible for their manuscripts. The printed version is mailed out in limited numbers to institutions on the SLAC Instrumentation mailing list. Issues of the ICFA Instrumentation Bulletin are accessible electronically on our Web site:

http://www.slac.stanford.edu/pubs/icfa/

Cover: The illustration depicts L. J. Waghenaer's marine atlas, "The Mariner's Mirror," published in 1588. Lucas Janszoon Waghenaer was born in Holland in the 1530s. He became a famous ship pilot in his time. In 1584, he published the atlas ("Spieghel der Zeevaerdt") which was greatly valued among mariners for centuries. This was not due only to the map content, but also to the detailed knowledge of navigation techniques of that time. The atlas, as it appears on our page, is the same one used for the Dutch to English translation.

Conference List

- International Workshop on Aging Phenomena in Gaseous Detectors, DESY, Hamburg, Germany, October 2-5,2001.

- The Nuclear Science Symposium and Medical Imaging Conference, San Diego, CA, **USA,** November 4-10, 2001.

- "RPC2001 - Sixth Workshop on Resistive Plate Chambers and Related Detectors," Coimbra, Portugal, 26-27 November 2001.

Table of Contents

Gaseous Micropattern Detectors: High-Energy Physics and Beyond

Archana Sharma[1]
University of Maryland, College Park, 20742 MD, USA

Abstract

Multiwire gaseous detectors have matured in the last few decades with major implications in particle physics experiments. They have also been successfully refined for use in other fields: X-rays for medical imaging, UV and single photon detection, neutron and crystal diffraction studies, etc. Their major limitation has been a modest rate capability (10^3/mm^2). In the last decade, several micropattern position sensitive gas devices have been introduced with an inherently improved rate capability (few MHz/mm^2) and a localization accuracy of 40-50 µm. They are being extensively pursued for their application in several fields. The state-of-the-art of this new generation of gaseous detectors will be reviewed.

INTRODUCTION

The pioneering work done at the beginning of the twentieth century by Thomson, Rutherford, and Geiger [1] just after the discovery of electromagnetic radiation, focussed attention to the development of tools to detect radiation. The Single Wire Proportional Counter (SWPC) was one of the essential tools in the early part of the last century.

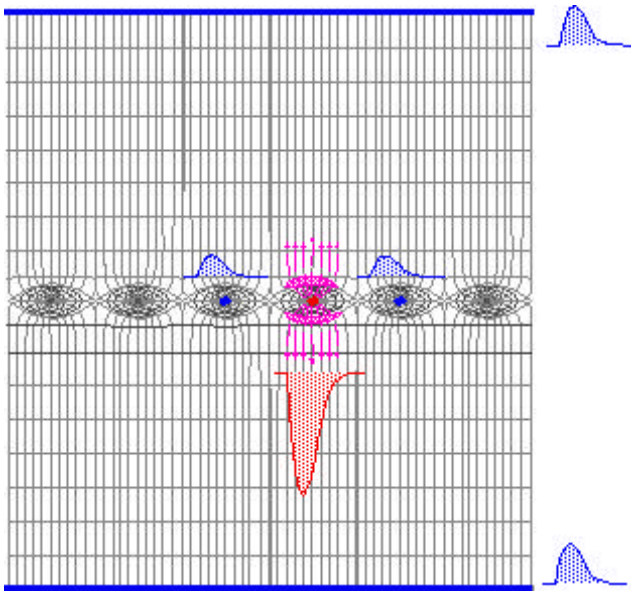

Fig. 1. Principle of the Multi-Wire Proportional Chamber (MWPC).

[1] Presently at CERN, CH 1211, Geneva, Switzerland. E-mail: Archana.Sharma@cern.ch

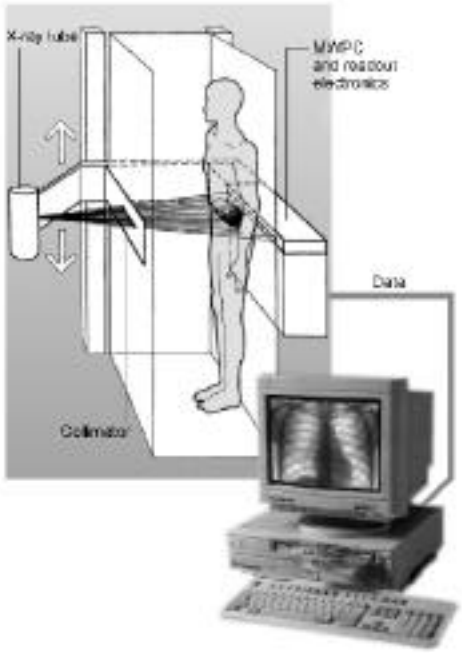

Fig. 2. The Siberian digital radiography device using MWPC [4].

It was not until the invention by Charpak in 1968 of the Multi-Wire Proportional Chamber (MWPC), see fig. 1 and Ref. 2, that a new era was ushered in this field. The main performance features of the MWPC are a space resolution of few hundred μm, two- and three-dimensional localization of incident radiation, excellent energy resolution, rate capabilities of a few kHz/mm^2. Two track separations of the order of 2 mm have been measured and very large active areas and volumes have been effected over the last three decades for charged particle tracking in medium and high-energy physics. Several excellent review articles have been written on the subject; a selection is given in Ref. [3].

Some applications of MWPCs may be cited as crystal diffraction, beta chromatography, and dual energy angiography. A low dose X-ray digital radiography scanner based on the MWPC (see Fig. 2) was invented by the BINP Novosibirsk group [4], and is presently being applied routinely to examine patients in hospitals in Russia and in France [5,6]. Fig. 3 taken from [6] shows a film of a congenital hip dislocation (Perthes disease) in a 7-year-old boy with satisfactory visualization of the femoral architecture and bone texture. Upgrades of this device for improved resolution and dose reduction are still in progress [6,7].

Fig. 3. Digital Radiography of a child with congenital hip dislocation using MWPC Scanner.

Despite their success, some fundamental limitations of multiwire proportional chambers restrict their use for high-rate application. Detailed discussions of these characteristics may be found in the cited literature: the wire spacing limits the position accuracy and two-track resolution to ~ 1mm. The electrostatic instability limits the wire lengths. The widths of the induced signal define the pad response function, and most importantly at high rates, accumulation of positive ions restrict the rate capabilities of MWPCs as shown in fig. 4.

The advent of high luminosity colliders [8] demands fast, highly performing position sensitive detectors. Ever more stringent, unsurpassed position, two-track, two-dimensional and time resolutions, ability to operate withstanding long-term radiation and background environment are key requirements.

A concept worth mentioning here is that employed by the Multi-Step Chamber, which was introduced by Charpak and Sauli [3]. It comprises dividing the total gain of the MWPC into two smaller sub critical parts by first allowing the electrons produced by ionizing particles to multiply in the pre-amplification region and then proceed to the anode for further amplification, In this way, the chamber operation was found to be more stable and provided higher gain, as shown in fig 5.

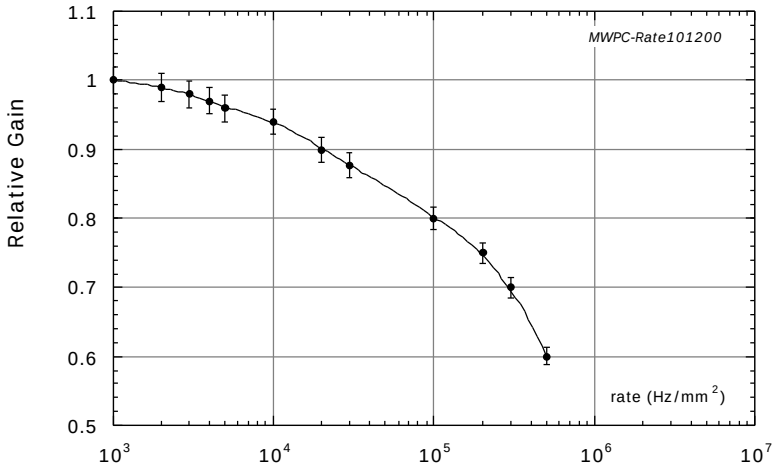

Fig. 4. Rate capability of a Multiwire Proportional Chamber.

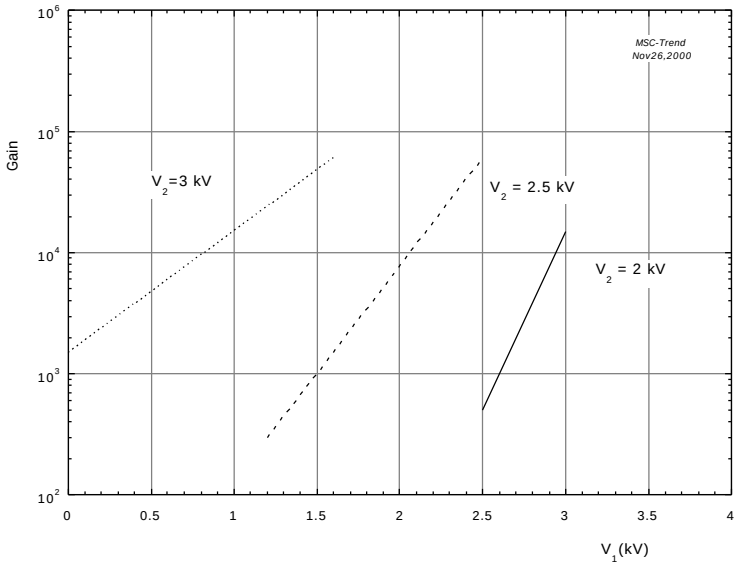

Fig. 5. High gain in a Multi-Step Chamber.

The invention of the Micro-Strip Gas Chamber (MSGC) by Oed [9] ushered another new era of gaseous detectors. A recent review [10] summarizes in detail the MSGCs and its derivatives, here I will briefly mention their key features and some applications.

A. THE MICRO STRIP GENERATION

An MSGC consists of a pattern of thin anodes and cathode strips laid on an insulating substrate with a pitch of a few hundred μm as sketched in fig. 6(a). Delimited by a drift electrode above and appropriate potentials applied, the resulting electric field[2] is as shown in Fig. 6(b). The design itself removes the positive ions from the vicinity of the avalanches, thereby lending high rate capability to this device almost two orders of magnitude higher (~ 10^6/mm^{2}s) than MWPCs (~10^3/mm^{2}s).

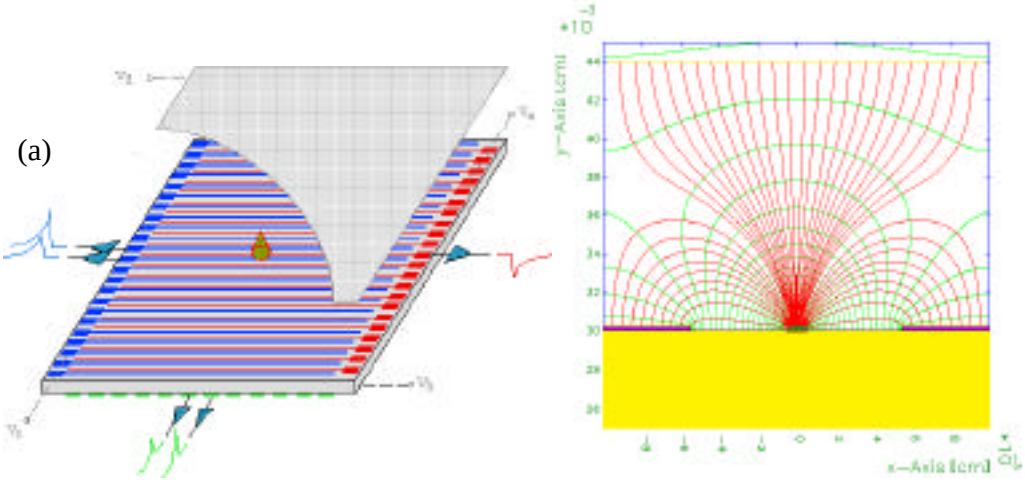

Fig. 6. (a) Principle and (b) Field configuration in an MSGC with typical voltage settings.

The salient features of its operation are localization accuracies ~ 30 μm rms, double track resolution of 400 μm, and good energy resolution. Long-term and magnetic field operations have been demonstrated, and apart from high-energy physics [11], these devices have found application in many varied fields of X-ray spectrometry and digital radiography.

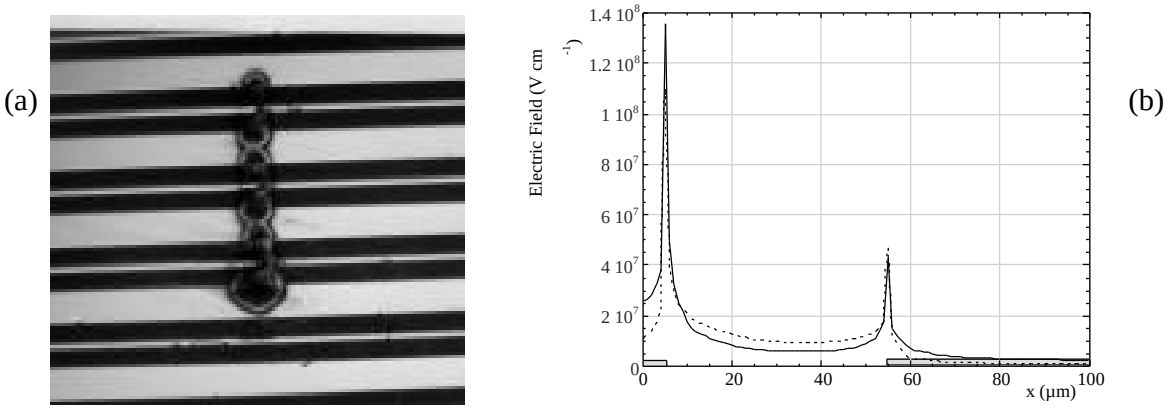

Fig. 7. (a) Damage in an MSGC and (b) Field along the surface of an MSGC.

[2] All electric fields and simulations presented in this work are taken from Ref. 10 or are unpublished work of the author.

The difficulties associated with operating MSGCs [12] began when they were exposed to highly ionizing particles, usually present in a high luminosity machine backgrounds from low energy γ's, proton conversions, and nuclear fragments. The highly ionizing particles deposit almost three orders of magnitude more charge in the detection volume as compared to a minimum ionizing particle. In such a circumstance the avalanche to streamer, and avalanche to gliding discharge, transitions are more likely damaging the strips (see fig. 7a). Several groups dedicated themselves to examine and understand these defects [13-17]. What emerges is that the streamer mode of operation in the case of an MWPC is stable due to the fact that the electric field, shown in fig. 7(b), in the direction of the propagation of the streamer is increasingly weak (between the anode and cathode). In the case of micro-strip detectors, the anode-cathode distance is very small (~50-100 μm). The electric field at the tip of the streamer and that along the surface being high, the streamer is most likely to be followed by a voltage and ionization density dependent discharge. Charging up of surface defects, long-lived excited states, and overlapping avalanches seem to be the culprit lowering the discharge limits of operation of these devices. With this insight, several novel designs appeared on the horizon, some of which are discussed below.

III. THE 'NEW MICROPATTERN' ERA

B. MICRO-DOT AND MICRO-MEGAS

Early attempts to create the first micro-needle structure were done by Spindt et al. as early as 1976. Spindt used them successfully to emit electrons towards the phosphor screen in high vacuum, for the purpose of creation of the flat TV screens. Soon, several people [18], for example Va'vra and later on Oed with his own design of the micro-needle array, have tried to use them as the electron amplifiers in the gas.

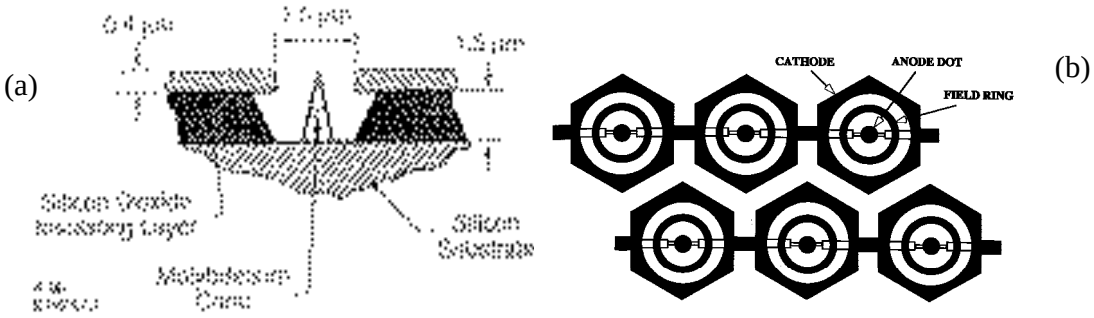

Fig. 8. (a) The micro-needle structure produced by Spindt et al., (b) Schematic of a Microdot Chamber.

However, no observable gas gain was measured at normal pressure due to the extremely fine needles [<<1μm radius and ~1.2 μm high; see fig. 8(a)], and resulting in very small amplification region. Advances in photolithography and application of silicon foundry techniques heralded a new era in the design and fabrication of "Micropattern Detectors". The Microdot detector (μDOT), sketched in fig. 8, and operated successfully by Biagi [19], is the ultimate gaseous pixel device with anode dots surrounded by cathode rings. The chamber could reach very high gas gains of ~10^6 without a discharge [20].

(a)

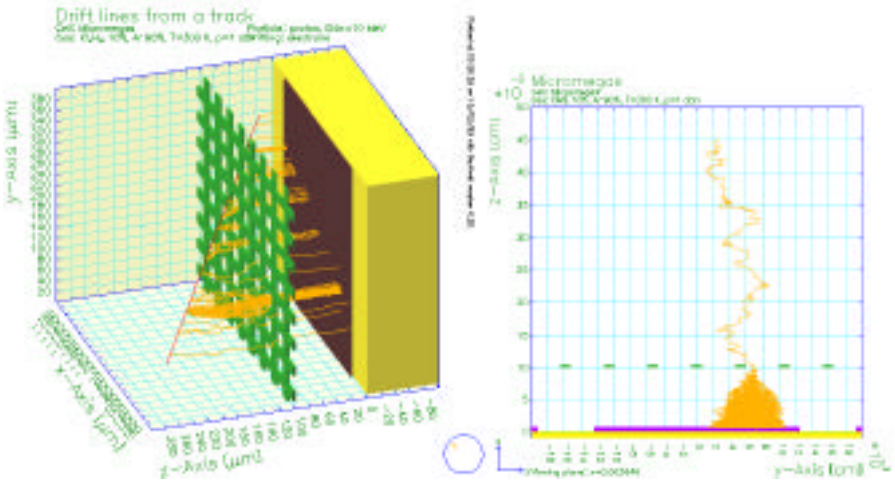

(b)

Fig. 9. (a) Electrons drifting from the sensitive volume into the amplification volume of a MICROMEGAS, (b) An avalanche in a MICROMEGAS detector.

A very asymmetric parallel plate chamber, the MICROMEGAS detector invented by Charpak and Giomataris [21], takes advantage of the semi-saturation of the Townsend coefficient at high fields ~ 100 kV/cm in several gas mixtures [22], thus being stable in its operation with minimum ionizing particles. Fig. 9 shows electrons drifting from the sensitive volume into the amplification volume and an avalanche in the thin multiplying gap. Figure 10 shows the excellent energy resolution of this device. Large area, 40 x 40 cm^2 MICROMEGAS detectors are being made and tested [23] for the COMPASS experiment at CERN; see fig. 11.

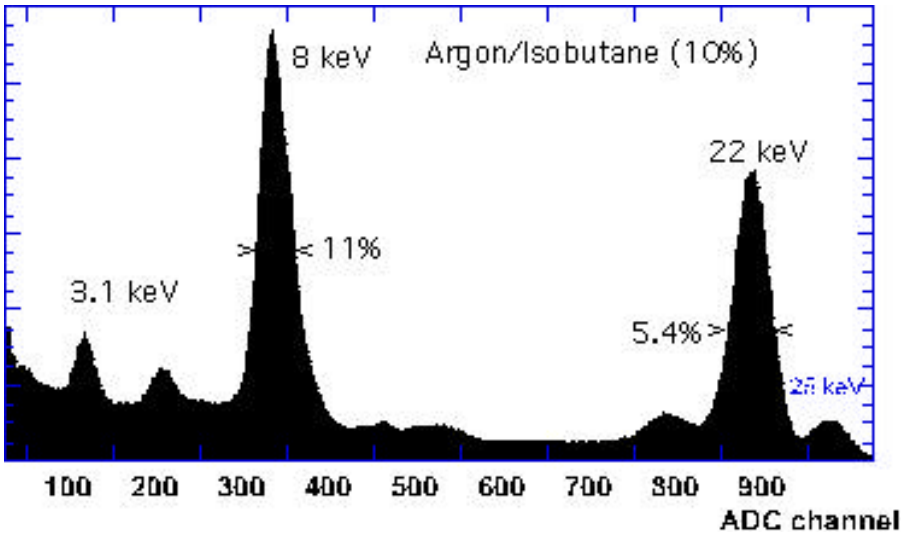

Fig.10. Energy resolution with a MiCROMEGAS detector.

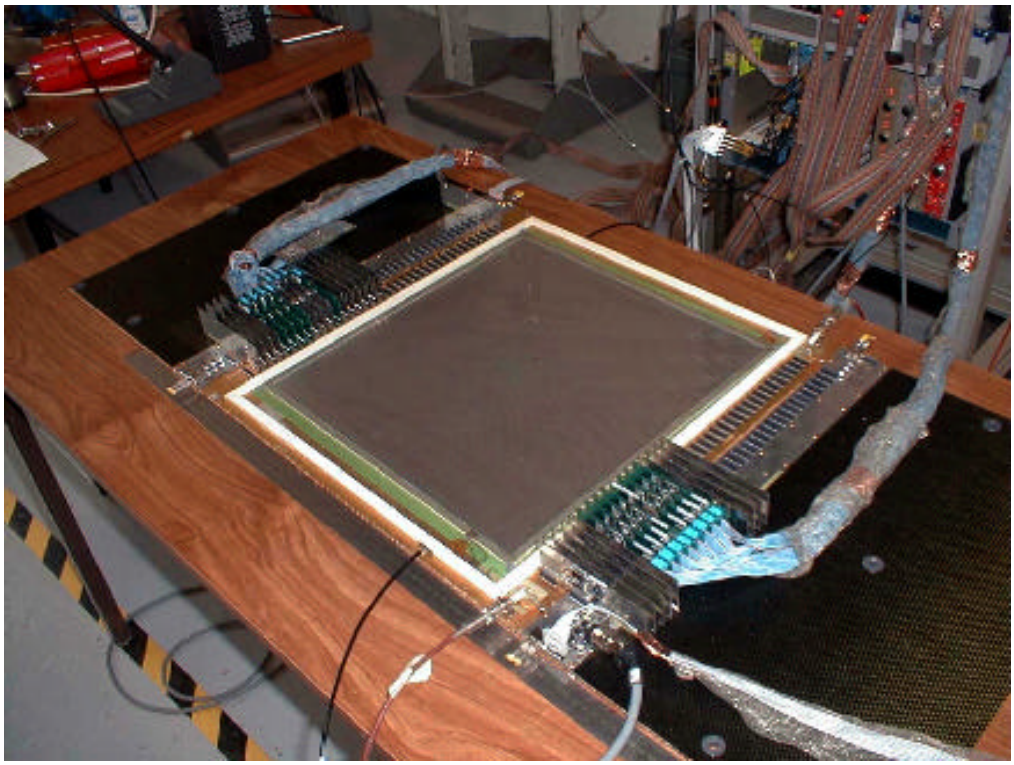

Fig. 11. Large size COMPASS MICROMEGAS prototype.

B. CAT detectors

A new kind of detector was invented by Lemonnier et al. during the same era as the detectors discussed so far, called the CAT or "Compteur A Trous"[3] [24]. It consists of a narrow hole micro-machined in an insulator metallized on the surface as the cathode.

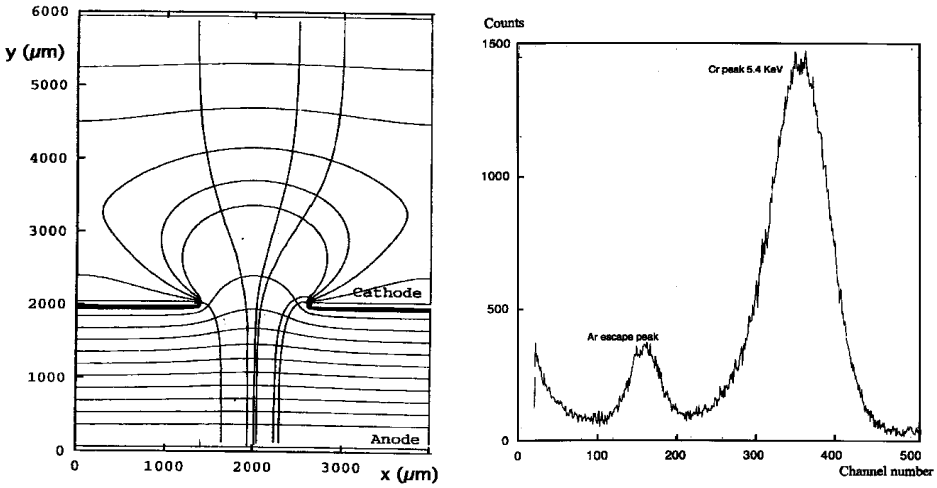

Fig. 12 (a) Electric Field in a CAT, (b) energy resolutio

[3] Patent No. 2727525 dated 25.11.94

The metal at the bottom of the hole constitutes the anode. With appropriate potentials and a drift electrode, this scheme acts as a focussing lens for the drifting electrons left in the wake of ionizing radiation as shown in fig. 12(a). Figure 12(b) shows the typical energy resolution measured with this kind of a device. Removing the insulator in between leaves the cathode as a micro-mesh, which when placed with a thin gap above the readout electrode, emulates the CAT operation hence named micro-CAT or µCAT, see Fig. 13 (a)[25]. This structure could reach gas gain of several 10^4. With an ingenious scheme of readout from virtual pixels made by current sharing, offering 20 times finer resolution as compared to the readout cell (Fig. 13(b)), the µCAT combined with the Virtual pixels is renamed the VIP [26].

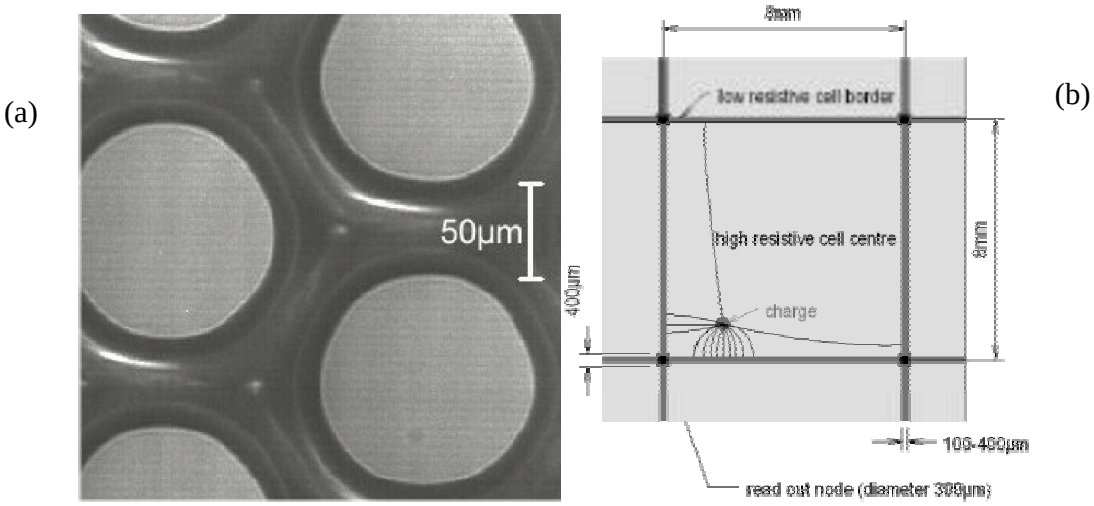

Fig. 13. (a) Microphotograph of a CAT mesh, (b) Virtual Pixel readout scheme.

C. GEM detectors

A new concept of gas amplification was introduced in 1996 by Sauli, the Gas Electron Multiplier (GEM) [27] manufactured by using standard printed circuit wet-etching techniques[4] schematically shown in Fig. 14(a). Comprising a thin (~50 µm) Kapton foil, double-sided clad with Copper, holes are perforated through (Fig. 15b).

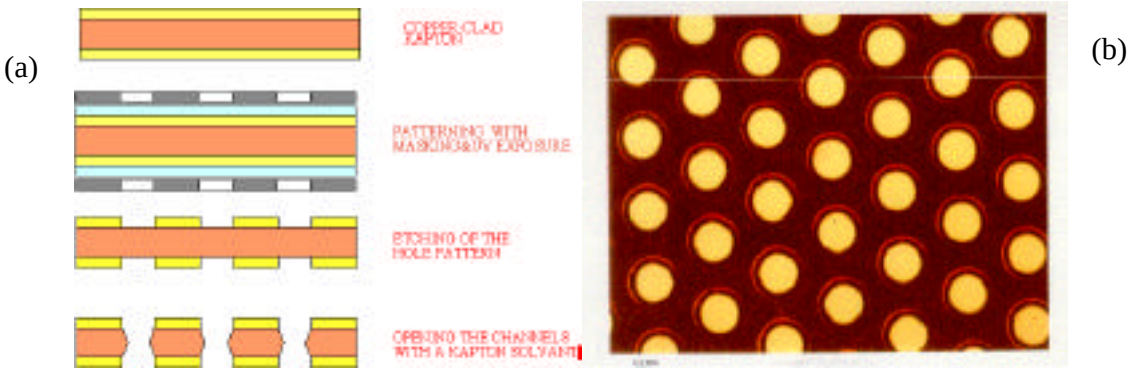

Fig. 14 (a) Chemical etching process of a GEM and (b) A GEM foil

The two surfaces are maintained at a potential gradient, thus providing the necessary field for electron amplification, as shown in Fig. 15(a), and an avalanche of electrons as in Fig. 15(b).

[4] At the Printed Circuit & Surface Treatment Workshop at CERN, Geneva, Switzerland.

(a)

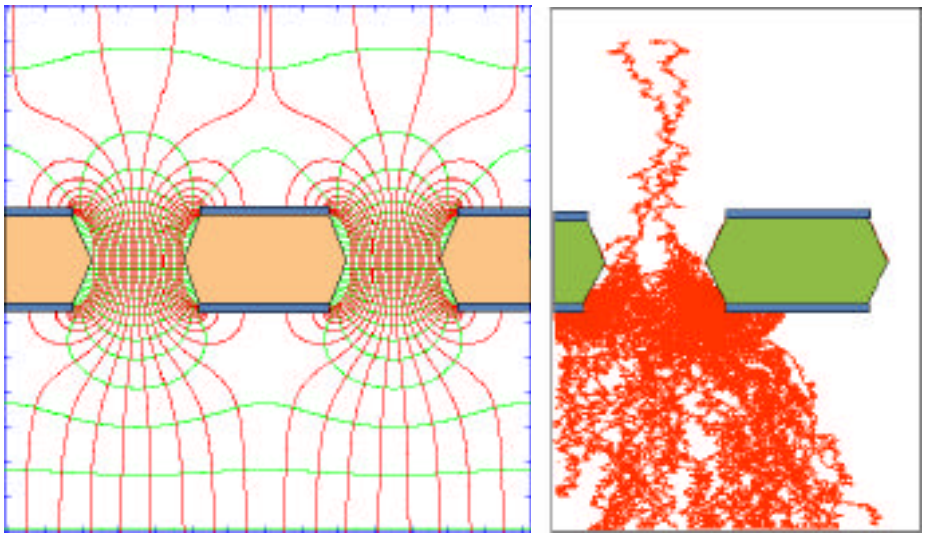

(b)

Fig. 15(a) Electric field and (b) Avalanches across a GEM channel.

Coupled with a drift electrode above and a readout electrode below, it acts as a highly performing micropattern detector. The essential and advantageous feature of this detector is that amplification and detection are decoupled, and the readout board is at zero potential. Permitting charge transfer to a second amplification device, this opens up the possibility of using a GEM in tandem with an MSGC or a second GEM.

D. Other MICROPATTERNS detectors

Following the GEM concept and better understanding of the discharge phenomena, several new 'micro'-detectors have appeared on the scene: Micro-Wire [28], an extension of the µDOT in the third dimension, Micro-Pin Array (MIPA) [29] (see figs. 16a and b), the Micro-Tube [30], Micro-Well [31], Micro-Trench [32] and Micro-Groove [33].

(a)

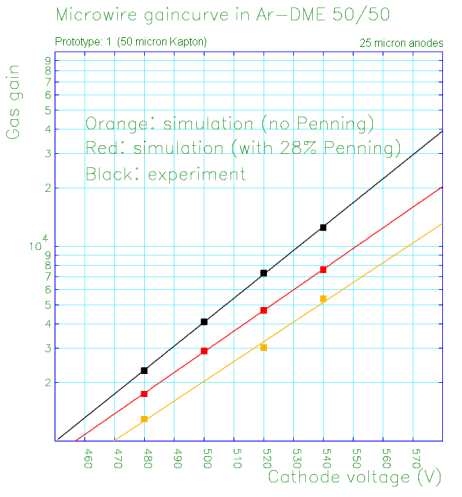

(b)

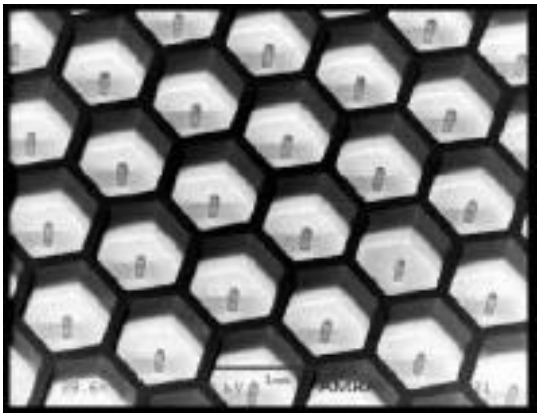

Fig. 16. (a) Gain with a Micro-Wire Detector (b) The MIPA Array.

All these authors have tried to minimize the presence of insulators in between the anode and cathode, which is the culprit for gliding discharges along the surface. Figure 17(a) shows a microphotograph of the Micro-Tube detector, with a field map in Fig. 17(b) [30]. Fabricated using combination of laser micro-

machining and nickel electroplating, it consists of ~150 µm diameter cathode and an anode tube, which is machined through the well and plated alongside.

(a) 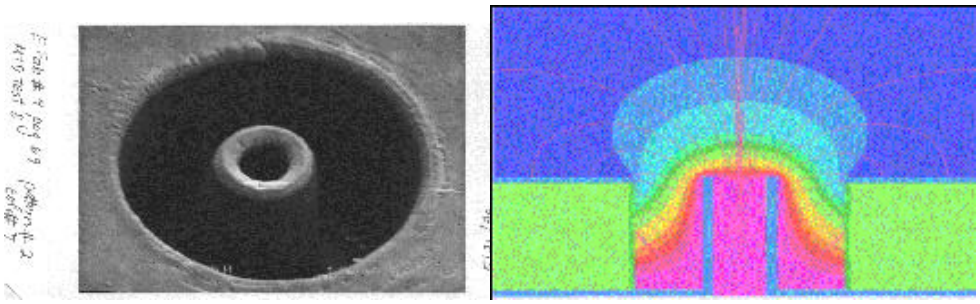 (b)

Fig. 17. (a) The Microtube: the central pin is metallized on the outside, emulating an anode wire, (b) Field across a Microtube.

This structure results in an electric field that increases rapidly at the anode, similar to the µDOT. However, there is no insulating material on the direct line of sight from the cathode to the anode. These design features are predicted to lead to higher gas gains, better stability with fewer discharges, and the reduction of charging effects. An investigation of the effects of detector geometry upon Microtube performance shows similar performance to the µDOT and µCAT detectors, it also predicts large gains ~ 10^4 [30].

As mentioned above, detailed studies have shown that discharges in the presence of highly ionizing particles appear in all micro-pattern detectors at gains of a few thousands [19]. It is possible to obtain higher gains with poorly quenched gases, since they permit a lower operating voltage, and have a higher diffusion, thus lowering the charge density and photon feedback probability. Combining the MSGC with a GEM, safe operation has been demonstrated up to gains of few ten thousands; ~200 of such detectors are operating at HERA-B [34]. The DIRAC [35] experiment at the CERN PS also employs MSGC + GEM detectors, which have permitted to improve the momentum resolution by a factor of two; Fig. 18 (a and b) shows an assembled GEM + MSGC, and is a fine example of vertex reconstruction using this detector.

(a) 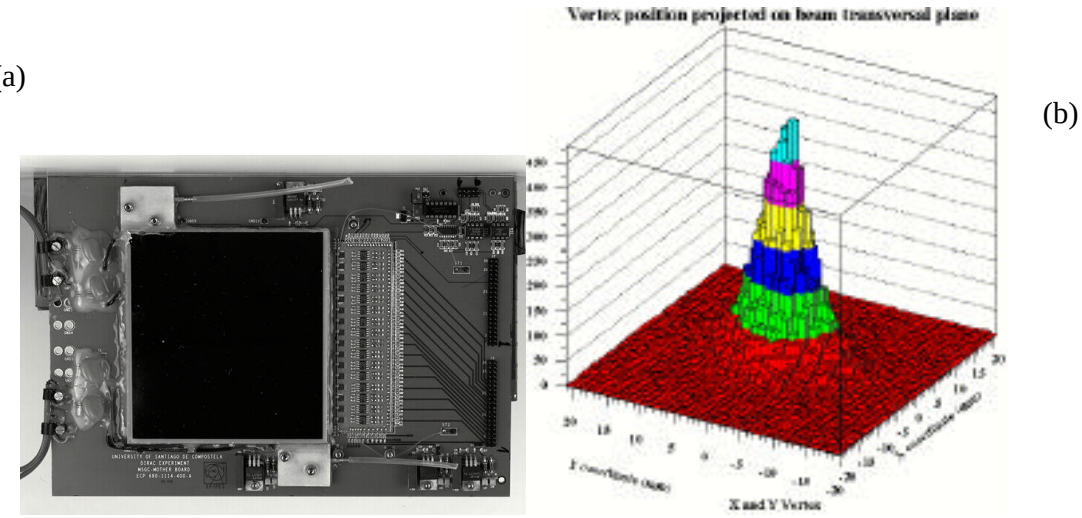 (b)

Fig. 18. (a) An MSGC + GEM assembly for DIRAC tracker, and (b) Vertex reconstruction.

Putting two GEMs in tandem offers a robust detector, which has been studied in detail [36], and large size devices are being built for the COMPASS experiment [37], Carrying the concept further, adding a

third GEM offers an even more stable operation in the worst hadronic beam environment, as demonstrated in Ref. [38]. At gains of ~10^4, spark probabilities (~10^{-10}) have been measured.[5] Figure 19 shows the probabilities of discharges in a single, double and triple GEM detector [37]. For large sizes, the GEMs are segmented in order to reduce the capacity, thus limiting the energy in a discharge.

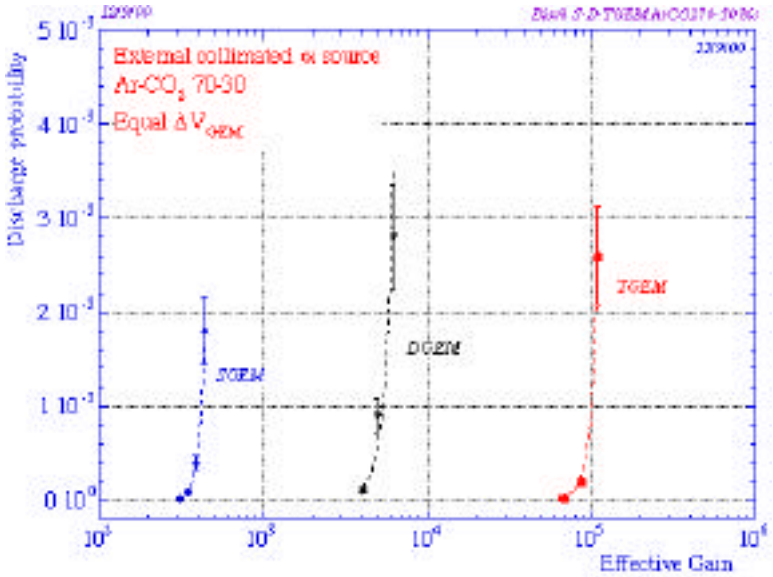

Fig. 19. Probability of a discharge, normalized to the number of heavily ionizing tracks, versus gain for single, double and triple GEM detectors.

IV POTENTIAL APPLICATIONS OF THE "MICRO-GENERATION"

A. MSGCs for X-Ray Imaging

Conventional film radiography has very good spatial resolution, but limited dynamic range. For radiographic film, the storage and display media are the same. For film storage media, dynamic range means that the film image saturates (additional photons do not cause proportional film darkening). The display contrast is fixed at the time of film exposure. One does not see much difference in visible contrast in different parts of a film image, which can have widely different number of photons/pixels. Whereas in a digital system, the storage medium (computer) does not saturate and has infinite dynamic range. The display media being different from storage can be varied at will, i.e., the available display dynamic can be chosen to cover the number N photons/pixel from any N (min) to N(max). The image can be further enhanced using photon energy information. This has been made possible by using the MSGCs with Xe-CH_4 at high pressures; an example of an image is shown in Fig. 20 [39].

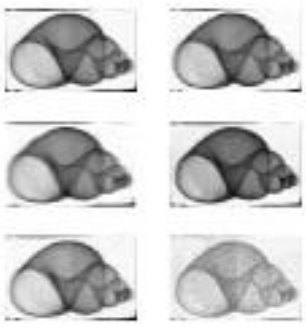

Fig. 20. Images of a snail shell taken with an MSGC operating with Xe-CH_4 at four bar [43].

[5] Defined as sparking rate divided by flux

B. TPC Readout

For the TESLA experiment at the future Linear Collider [40], a double or triple GEM configuration is under consideration [41,42] owing to its fast electron signal, minimal magnetic distortion effects, and suppression of ion feedback by design. Figure 21 shows some measurements and simulation of the fractional positive ion feedback in a double GEM [43].

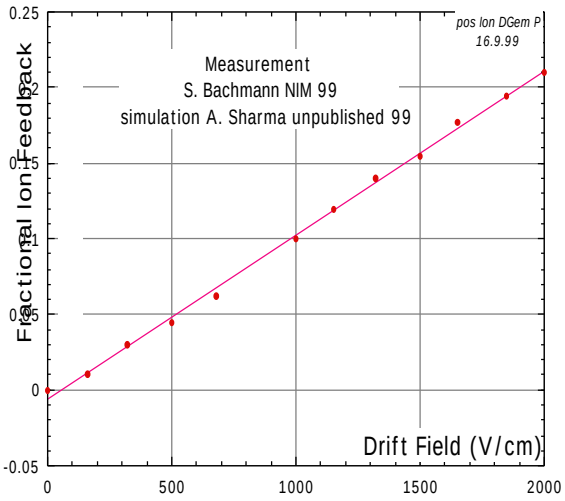

Fig. 21. Fractional ion feedback in the TPC drift volume (points are measurements [42], and a solid line is a computation).

Special hexagonal pads are being developed [41] proving unprecedented resolution of 50-60 μm in a TPC, using charge sharing and induction signals.

C. The MICROMEGAS X-ray Gallery

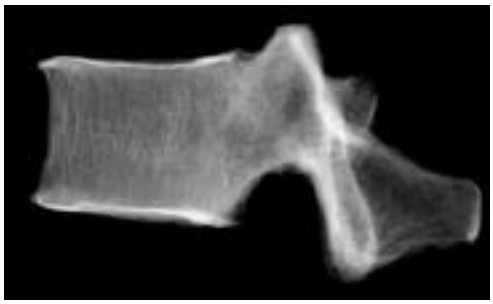

Fig. 22. The Radiographic image of a vertebra taken by MICROMEGAS.

Operating in pure Xenon at atmospheric pressure, the MICROMEGAS detectors have been developed for X-ray imaging. Figure 22 [45] shows an exampleof a vertebra scanned by MICROMEGAS.

D. Protein Crystallography SAXS (Small Angle X-Ray Scattering)

X-ray diffraction studies using MSGCs have yielded rapid analysis of single crystal structures by using the information of position and time of the incident X-rays: crystal structures of organic molecules can be obtained in a matter of minutes [46]. Fast time resolved X-ray diffraction measurements offer a time

variation of the SAXS pattern of a protein solution for example, shown in Fig. 23, within a frame time of 10 ms.

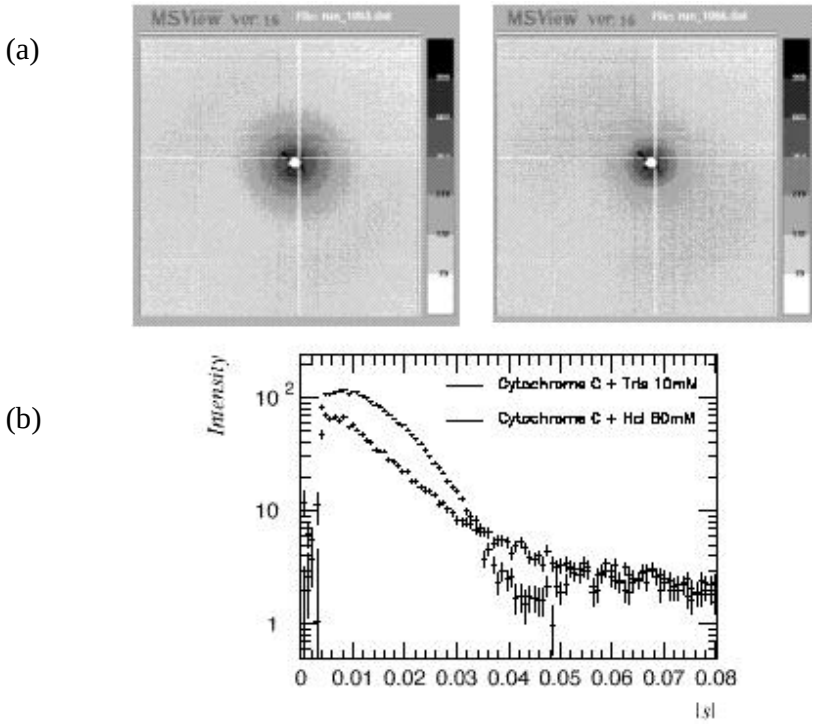

Fig. 23. (a) X-ray diffraction patterns of Cytochrome shows different concentrations of contamination molecules. (b) X-ray diffraction intensities of the same, measured more than a minute after mixing the solutions.

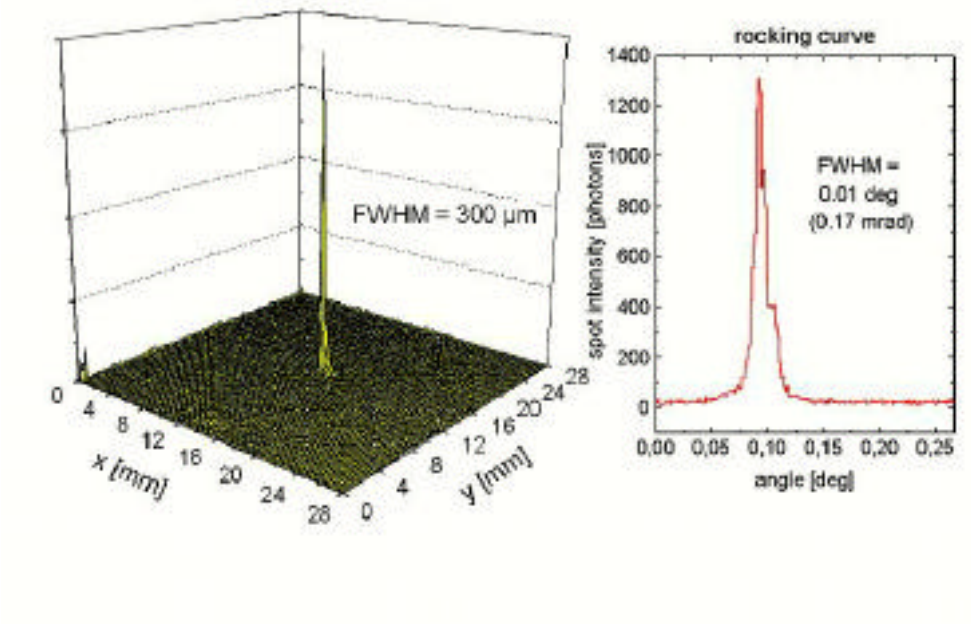

Fig. 24. A single intensive spot in the crystallogram of a protein crystal, collagen using VIP.

A diffraction pattern of a lipid membrane is shown in Fig. 24. The membrane was made with a VIP detector at Elettra (see section III.B above), a synchrotron source in Trieste, Italy. With complex algorithms, especially made for the readout cell border, and superimposing several shots of images, a high degree of detail may be obtained from diffraction patterns; see Fig. 25 and Ref. 26.

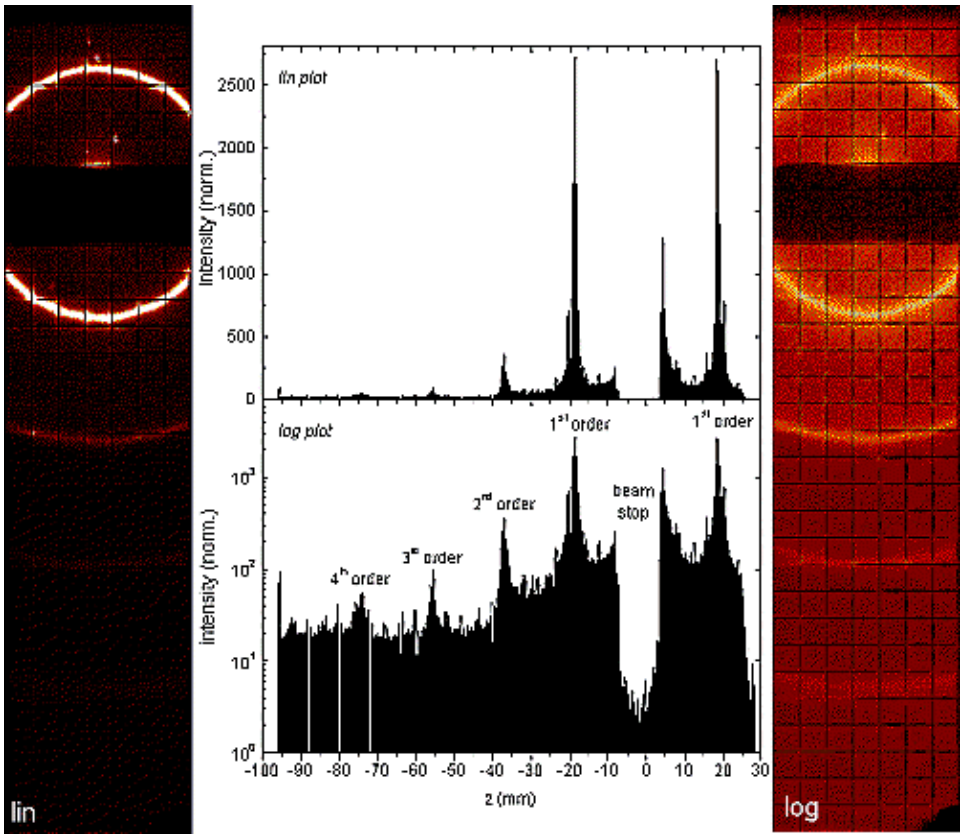

Fig. 25. Scan of the diffraction pattern of the lipid with a VIP; the middle part shows linear and logarithmic profiles of the pattern.

E. Digital Mammography UV and Visible Photomultipliers using GEM

The importance of early detection of cancer is obvious, small tumors are usually detected in routine radiographic scanning of the human body. Current radiographic equipment is limited in its detection capability by the limited contrast difference exhibited by malignant and benign tissues under given radiation doses. A combination of an x-ray converter, a MSGC, and a visible photocathode, shows great promise for a detector for digital mammography [47]. The essential features are a large flat area and high resolution. With a photocathode (UV, visible) coupled to a micropattern detector, the sealed gas avalanche photomultipliers are being developed for fast imaging of UV and visible light, as well as flat readout devices for scintillator and scintillating fiber arrays, and as medical imaging. Photocathodes have also been attempted by combining them with the Glass Capillary Plate (GCP) detectors [48], with the advantages of reduced photon-photon feedback and the high level of cleanliness necessary for the manufacture of high efficiency of photocathodes/secondary photon emitters.

To this end, single-photon detection has been actively pursued using a CsI photocathode coupled to three or four GEMs in tandem, and very large gains ~ 10^5 have been obtained in pure noble gas (Ar), and 10^6 with an admixture of few percent CH_4. [47]. With a small preamplification in the drift region, combined with high diffusion, fully efficient single-photon detection is predicted and measured [49,50] as demonstrated in figs. 26 (a and b). Fig. 27 shows an example of a large single-photon signal in Ar-CH_4 (95-5) with a three GEM combination [51].

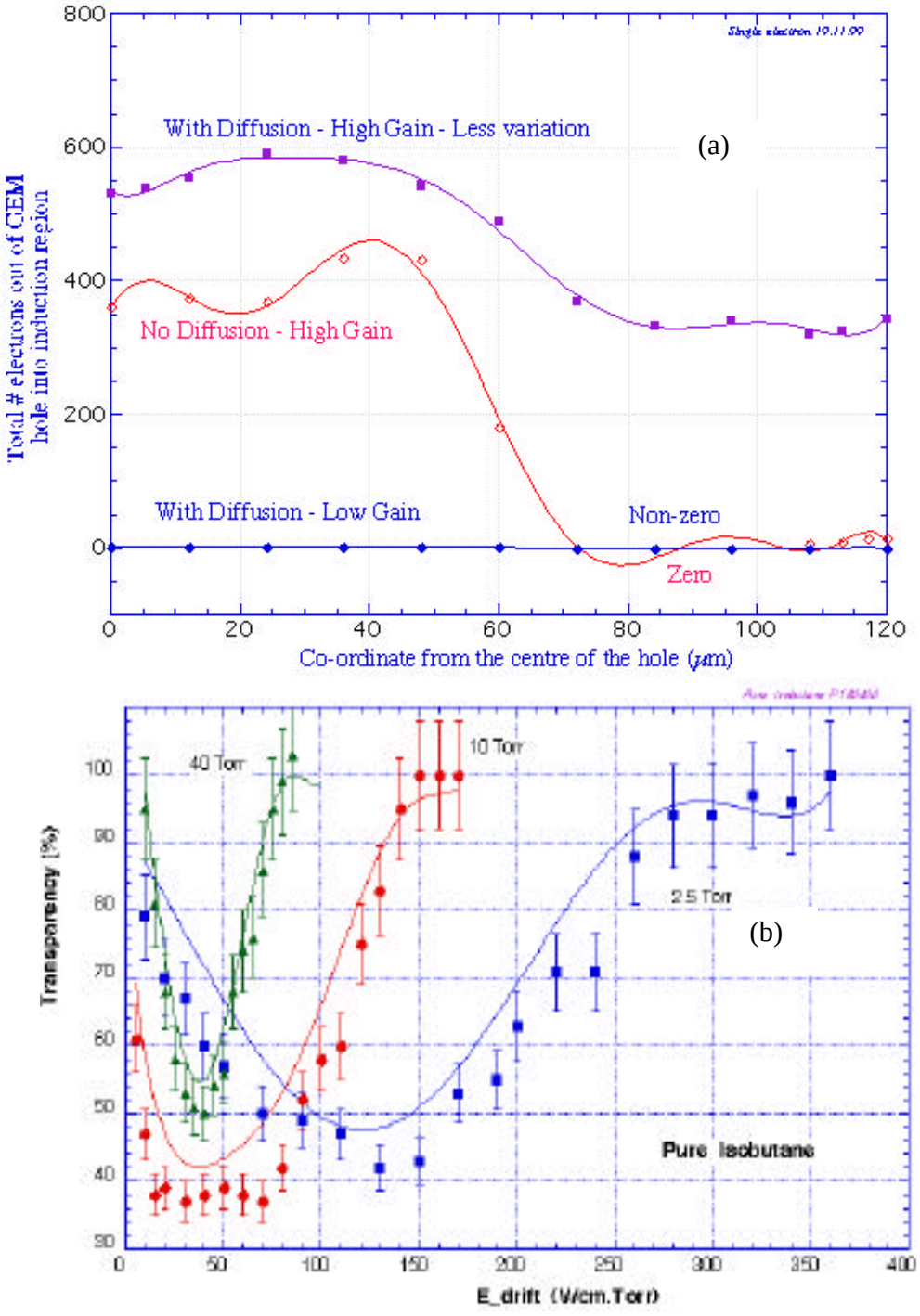

Fig. 26. (a) Transmission of single electrons amplified in a GEM, (b) Full efficiency of single electrons in a GEM with a transmissive photocathode and preamplification in the drift region.

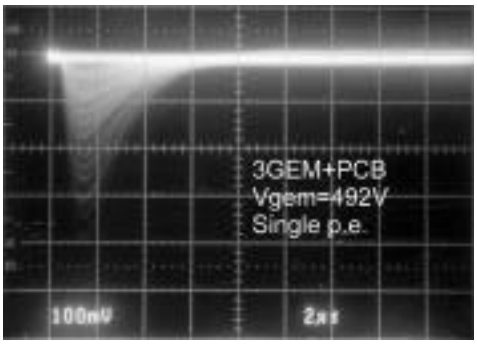

Fig. 27. Single-photon signals with a Triple GEM and CsI photocathode.

F. Cherenkov Ring Imaging (RICH/DIRC)

A feasibility study aimed at improving the detection of photons emitted by Cherenkov light, for example, for an upgrade of the existing SLD CRID at SLAC was made. Using a cascade of four GEMs and an operating gas as pure ethane, very high gains have been observed [49,52], as shown in Fig. 28.

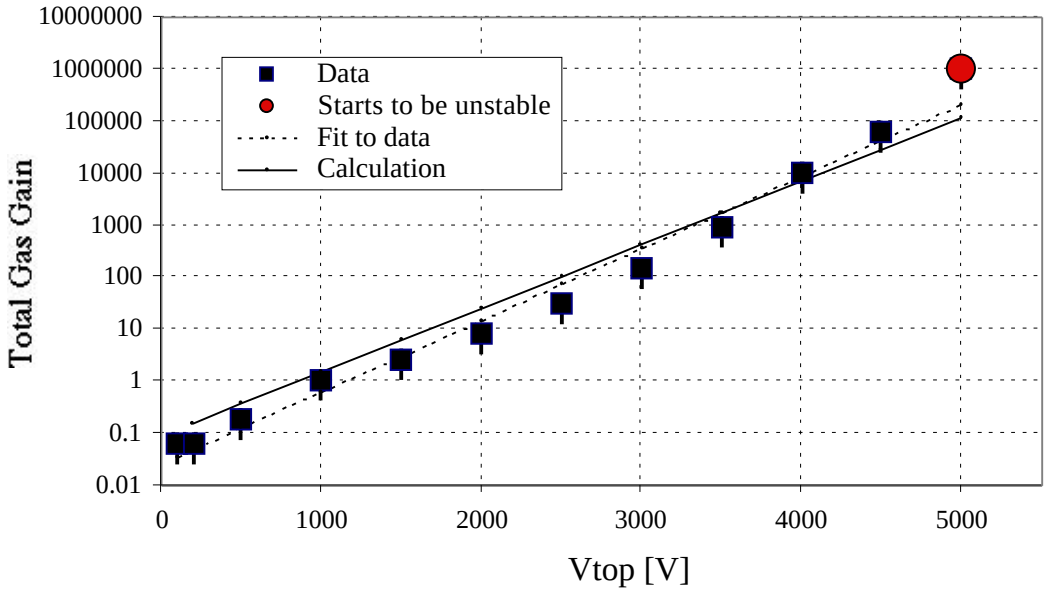

Fig. 28. Gain in a Quadruple GEM cascade in ethane gas at 1 bar and room temperature.

G. Scintillation Light Imaging

A novel application of micro-pattern technology was developed by integrating a MSGC in a gas proportional scintillation counter (GPSC) [53]. Instead of the usual photomultiplier tube, a reflective CsI photocathode was deposited on the microstrip plate surface of the MSGC that serves as the VUV photosensor for the scintillation light from xenon GPSC. This hybrid detector will be used to measure the Lamb shift in muonic hydrogen by detecting the 1.9-keV x-ray from the 2P-1S de-excitation, in a 5-T magnetic field [54].

With a GEM as amplifier and a CCD camera, images of individual projected alpha tracks are visible using the scintillation properties of Ar and CF_4, as shown in Fig. 29 [55]. The spectral distribution of the emitted light is analyzed in terms of the number of photons emitted per electron in the visible and near-infrared regions ($400<\lambda<1000$nm). The maximum number of photons emitted decreases with pressure.

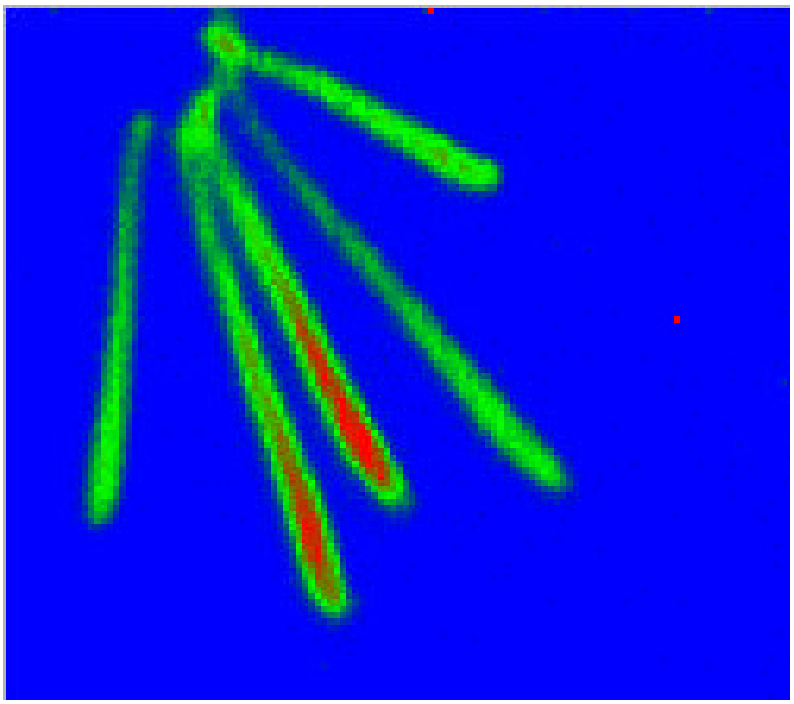

Fig. 29. Scintillation images of alpha tracks in Ar-CF_4.

H. X-ray imaging: Radiology and diagnostics

With a GEM + MSGC combination operating in Xe-CH_4 at 4 atm. X-ray images have been taken as an excellent example of imaging for diagnostics with a micro-pattern detector; see Fig. 30 and Ref. 41.

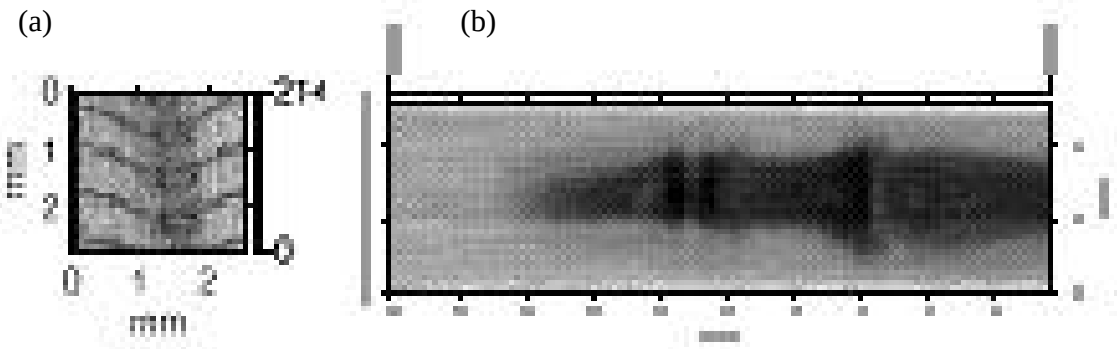

Fig. 30. (a) A 3 mm x 3 mm 13 kV X-ray absorption radiography of a fish bone taken at 2 atm. (b) a 3 mm x 10 mm 50 kV x-Ray digital image of a mouse.

Specialized two-dimensional readout boards have been manufactured using the GEM technology. Operating at ground potential, these boards, in conjunction with GEMs, have been developed for digital absorption radiography [43]. With a pixel size of 50 μm, the image of a mammal (small bat, width 32 mm) is shown in Fig. 31 taken from Ref. [42].

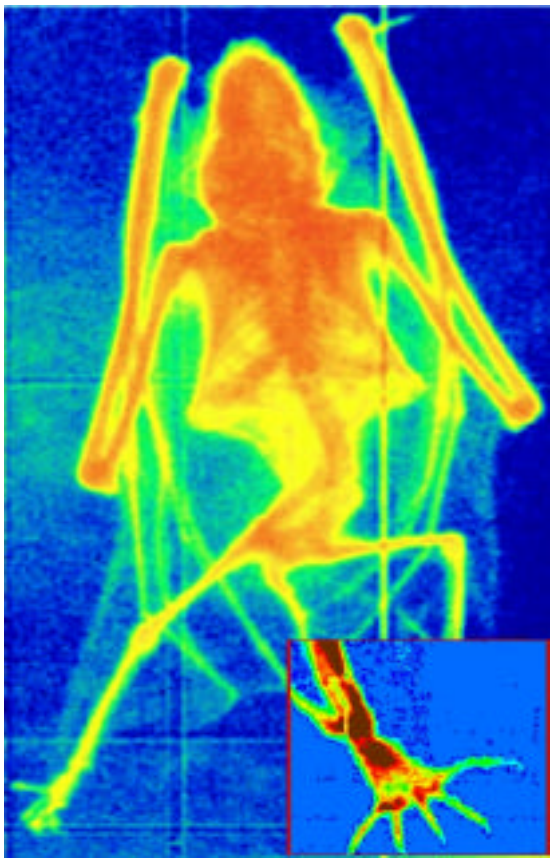

Fig. 31. Radiography of a small bat using GEM and 50μm x 50 μm 2D-readout.

I. Imaging of Polarized X-Rays

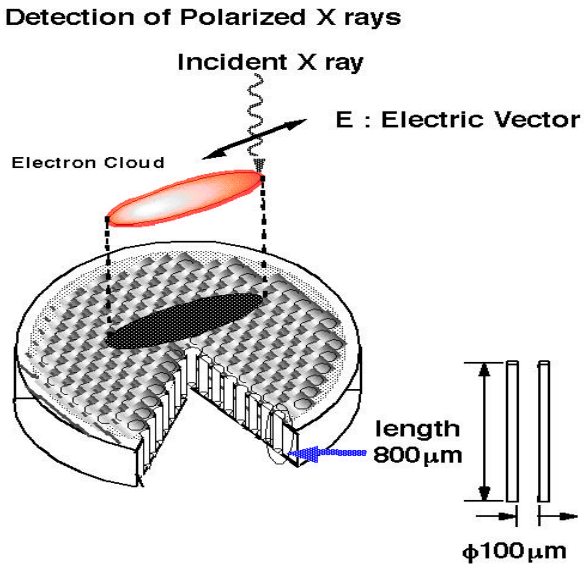

Fig. 32. Detection of polarized photons with a Glass Capillary Imaging Gas Proportional Counter.

In X-ray astronomy, measurements of X-ray polarization are useful to investigate features of magnetic fields such as pulsars, synchrotron nebulae, and so on. Some X-ray polarimeters have been developed using GCPs and GEMs [56-57] as exemplified in fig. 32. Because the emission direction of the primary electron depends on the polarization of the incident X-rays, the information on the polarization can be deduced, acquiring the information on the shape of electron clouds. The performance of the Polarimeter is expressed as the function of detection efficiency and modulation factor, and hence these parameters depend on gas pressure and gas depth. Figure 33 shows some images of tracks from a GCP [57].

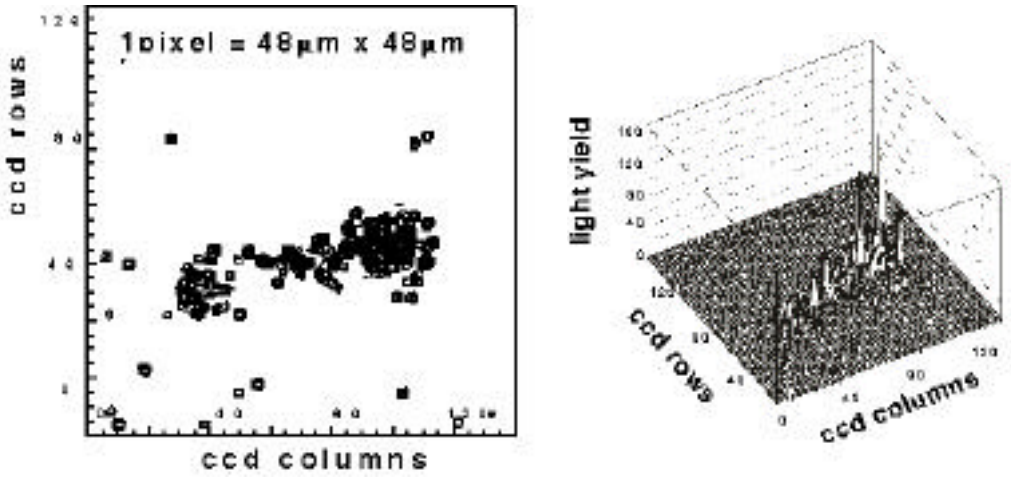

Fig. 33. Photoelectrons from a GCP Polarimeter.

J. GEM for Plasma Diagnostics

Exploiting the selective sensitivity and the high rate capability of GEM to soft X-rays, imaging the dynamics of fusion plasmas has been attempted by the Frascati and Pisa groups for the Frascati Tokamak Upgrade (FTU). With a GEM and individual pixel readout, time resolved plasma diagnostics are made giving information about temperature and turbulence effects. Figure 34 exemplifies the recognition of a steady state and collapsed plasma [58] by integrating counts over 50 μs in four adjacent channels.

(a)

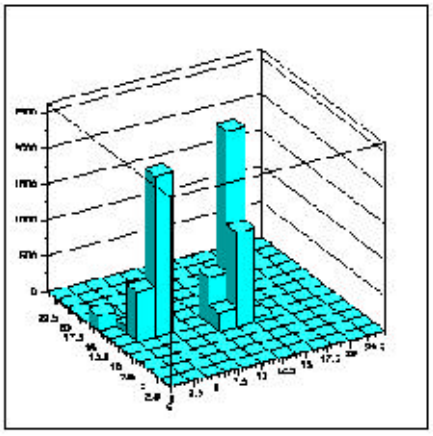

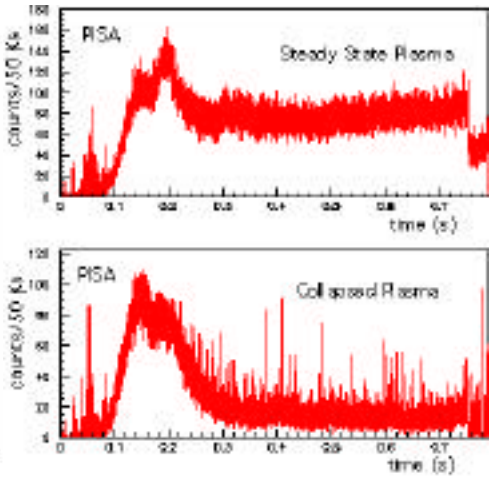

(b)

Fig. 34. (a) Reconstruction of photoelectrons with a GEM + micropixel readout, (b) Counts integrated in 50 μs for four adjacent pixels at the Frascati Toakamak [56].

V CONCLUSIONS AND OUTLOOK

Multiwire chambers have matured since their introduction over the last few decades, with several applications in particle physics and diagnostics of various kinds. The last decade has seen several novel developments in Micropattern Gaseous Detectors of which some have been summarized in this overview. Basic understanding of the discharge mechanisms in these devices has also improved, allowing amelioration of their design. Progress in the manufacture of customized readout boards has evolved, revolutionizing the potential applications of these detectors in radiology, diagnostics, astrophysics, and other fields.

VI REFERENCES

[1] Phil. Mag. Xiii(1896)392; Townsend and Raether, Conduction of electricity through gases (Ist ed, 1903); Proc. Of Royal Society, A81(1908)141

[2] G. Charpak et al Nucl. Instr. And Meth. 62(1968)262-268

[3] A. Breskin et al, Nucl. Instr. And Meth 161(1979)19; F. Sauli Physica Scripta 23(1981)526; G. Charpak and F. Sauli Ann. Rev. 34(1984)285, See also C. Grupen, Particle Detectors, Cambridge Press, 1996

[4] E. Babichev et al (1992) Nucl Instrum Methods Phys Res A323: 49, and references therein, S. Baru et al, Novosibirsk Preprint 35(1989) 98-39

[5] G. Kalifa et al, Pediatric. Radiology 28(1998)557

[6] E. Babichev et al in the Proceedings of Frontier Detectors for Frontier Physics Elba, Italy May 2000 & A. Porosev, in Proceeding of Frontier Detector for Frontier Physics, Elba May 2000.

[7] Martinez-Davalos et al, Evaluation of a new low-dose digital x-ray system. Phys Med Biol 38(1993)141

[8] Large Hadron Collider (LHC) at CERN

[9] A. Oed, Nucl. Instr. And Meth. A263(1988)35

[10] F. Sauli and A. Sharma, Annual Rev. of Nucl. Sci. 49(1999)41

[11] R. Bouclier et al Nuclear Physics B 61B (1998)315

[12] B. Boimska et al Nuclear Physics B 61B (1998) 498

[13] B. Schmidt , Nucl. Instr. And Meth. A419(1998)230

[14] V. Peskov et al, IEEE Transactions, Nucl. Sci. NS 45(1998)244

[15] A. Bressan et al Nucl. Instr. And Meth. A 424(1998)321

[16] P. Fonte et al Nucl. Instr. And Meth. A 419(1998) 405

[17] J. Kadyk et al Nuclear Physics B 61B (1998) 258

[18] C. A. Spindt et al., The Micro-needle Concept, J. Appl. Phys. 47(1976)5248; both experimental attempts of Va'vra and Oed were unpublished; see J. Va'vra, SSC Proposal 81187, 1987.

[19] S.F. Biagi et al, Nucl. Instrum. Methods A371(1995)12

[20] A. Bressan, A. Buzulutskov, L. Ropelewski, F.Sauli and L. Shekhtman, Nucl. Instr. And Meth. A 432(1999)119-124

[21] Y. Giomataris et al Nucl. Instr. And Meth. A 376(1996)29

[22] A. Sharma, ICFA Bulletin Fall 1999 http://www.slac.stanford.edu/pubs/icfa

[23] F. Kuune in Proceeding of Frontier Detector for Frontier Physics, Elba May 2000

[24] F. Bartol et al., J. Phys. III France 6 (1996)337, G. Chaplier et al Nucl. Instr. And Meth A426(1999)

[25] A. Sarvestani et al Nucl. Instr. And Meth. A 419(1998)444

[26] N. Pavel, Siegen, Priv. Com. Oct 2000

[27] F. Sauli Nucl. Instr. And Meth. A 386(1997)531

[28] B. Adeva et al., Nucl. Instr. And Meth A 419(1998)405

[29] P. Rehak et al Proceedings IEEE Nuclear Science Symposium 1999, Seattle USA

[30] W. K. Pitts et al Nucl. Instr. And Meth A438(1999)277

[31] W. K. Pitts See also Proceedings, IEEE Nuclear Science Symposium 1999, Seattle USA

[32] R. Bellazzini et al, Nucl. Instr. And Meth. A 423(1998)125

[33] R. Bellazzini et al, Nucl. Instr. And Meth. A 424(1998)444

[34] C. Richter, PhD. Thesis October 2000 submitted to University of Heidelberg, Germany.

[35] F. Gomez Private Communication and Internal Notes. T. Nunez, and P. Vasquez Theses 1999, Santiago University, Spain.

[36] J. Benlloch et al, IEEE trans NUCl. Sci. NS-45(1998) 234, J. Benlloch et al NIMA 419 (1998) 410
[37] B. Ketzer, Contribution to this Conference
[38] M. Ziegler et al hep-ex/0007007/July 2000, LHC-B Internal Tracking Notes: 99-024, 2000-013, 2000-15, 2000-056, U. Straumann Proceedings, Imaging 2000, Stockholm.
[39] M. Dixit et al, IEEE Trans. 47(1998)809; D. G. Gobbi et al, Phys. Med. Biol. 44(1999)1317
[40] The future TESLA Linear Collider at DESY Hamburg, DESY 97/048
[41] M. Dixit in Proceedings of Imaging 2000, Stockholm.
[42] A.Bressan et al Nucl. Instr. And Meth. A 425(1999)254, 262
[43] A. Bressan et al Nucl. Instr. And Meth. A 423(1999)424
[44] A. Sharma, Nucl. Instr. and Meth. A454(2000)267 Proceedings of Symposium on Applications of Particle Detectors in Medicine, Biology and Astrophysics, 5-8 October 1999, Siegen, Germany, also printed as CERN-OPEN-99/373.
[45] G. Charpak and M. Meynadier Priv. Com. Oct. 2000
[46] S. Ochi et al, SPIE Proceedings 5(1998)324
[46] DIGITAL MAMMOGRAPHY Project MICADO within Weizman, Pisa, Brussels, and Agfa Gaevert.
[47] A. Breskin et al NIM A 442(2000)58
[48] V. Peskov et al NIM A433(1999)492,V. Peskov etal IEEE Trans. Nucl. Science NS-45(1999)244, and contribution to this conference.
[49] A. Sharma CERN Preprint 99/372, Submitted for publication to Nucl. Instr. & Meth. (1999), See also Proceedings of Imaging 2000, Stockholm, June 2000.
[50] C. Richter et al To Appear in the Proceedings of Frontier Detectors for Frontier Physics, Elba 2000. Submitted Nucl. Instr. And Meth.
[51] A.Buzulutskov et al. Nucl. Intr. And Meth A443(2000)164-180, A 433(1999)471, andContribution to Nuclear Science Symposium and Medical Imaging conference, Oct 2000
[52] J. Va'vra Priv. Com. April 2000, and [49]
[53] J.F.C.A. Veloso et al Nucl. Instr. And Meth. A In Press
[54] J.F.C.A.Veloso et al Nuc. Instr. And Meth A In Press
[55] F. Fraga et al, in Nuclear Science Symposium and Medical Imaging conference, Oct 2000, Lyon
[56] H. Sakurai et al. "A new type of proportional counter using a capillary plate" NIM A374(1996)341-344,
[57] T.Masuda et al. IEEE Trans NS 47, 2000.
[58] R. Bellazzini et al, Proceedings of Imaging 2000, Stockholm.

DIRC DREAMS REDUX: RESEARCH DIRECTIONS FOR THE NEXT GENERATION OF INTERNALLY REFLECTED IMAGING COUNTERS*

Blair N. Ratcliff

Stanford Linear Accelerator Center, Stanford University, Stanford, California 94309, USA

Abstract

Some general conceptual design features of total internally reflecting, imaging Cherenkov counters (DIRCs) are described. Limits of the DIRC approach to particle identification and a few features of alternative DIRC designs are briefly explored.

1. Introduction and Scope

The DIRC, for **D**etection of **I**nternally **R**eflected **C**herenkov (Light), is a subtype of **R**ing **I**maging **Ch**erenkov counter (RICH). It "inverts" the usual principle for use of light from the radiator of a RICH by collecting and imaging the total internally reflected light, rather than the transmitted light. In so doing, a DIRC utilizes the optical material of the radiator in two ways, simultaneously; first, as a Cherenkov radiator, and second, as a light pipe for the Cherenkov light trapped in the radiator by total internal reflection. The high reflection coefficients inherent in the total internal reflection process, and the fact that the magnitudes of angles are conserved during reflection from a flat surface allow the photons of the ring image to be transported to a detector outside the path of the radiating particle, where they may be imaged [1-2].

A number of DIRC prototypes have been constructed and tested over the past few years [3-8]. The first large-scale DIRC detector designed for physics is now running in the BABAR detector at PEP-II [9]. This detector uses a radiator of 144-long fused silica bars ($1.7 \times 3.5 \times 490$ cm^3) arrayed as a

*Work supported by Department of Energy contract DE-AC03-76SF00515.

12-sided polygon around the PEP-II interaction region. These bars are coupled to an ~11,000 photo-multiplier tube (PMT) array through a 120 cm long standoff region filled with purified water. Though the performance of this device is excellent and well-matched to the particular requirements of an asymmetric B-factory like PEP-II, some design features, particularly the very long bars and the large water-coupled detection system, are less than ideal (at least aesthetically). The large water tank increases the susceptibility of the device to soft gamma background from the machine, and the overall design is rather inflexible geometrically. The basic features of this design were driven by "practical" compromises between detector performance on the one hand, and availability, timeliness, risk, and cost of components on the other. In particular, although reflectively focused schemes with better timing resolution were considered [10], the lack of any well-validated, cost-effective alternative to "standard" PMTs as the photon detector was a determining factor in reaching this design. With "standard" PMTs, one is naturally led to a large photon detection plane, water coupling, and the long bars to bring the light to the PMTs in a region that can be shielded from the magnetic field. During the intervening years, photon detectors have evolved, and it is interesting to look at how this evolution might affect some of the practical possibilities for DIRC, and what continued developments might portend for the future. This paper will attempt to clarify some of the issues discussed previously (see, e.g., the talk at RICH98 [11]), and in particular, will include a more complete, pedagogical discussion of the role of time resolution in DIRC counters.

2. Basic Cherenkov Equations

As is well-known, Cherenkov radiation is emitted at polar angle (θ_c), uniformly in azimuthal angle (φ_c), with respect to the particle path

$$\cos\theta_c = \frac{1}{\beta\, n(\lambda)}, \qquad (1)$$

where $\beta = v_p/c$. v_p is the particle velocity, c is the speed of light, and $n(\lambda)$ is the index of refraction of the material. Since the index of refraction is a function of the photon wavelength, in normal optical materials there is an "intrinsic" Cherenkov angle resolution limit that depends on the detected photon bandwidth.

The number of photoelectrons observed (N_{pe}) is given by the Frank-Tamm equation,

$$N_{pe} = 370L\int \varepsilon \sin^2\theta_c dE\,, \tag{2}$$

where L is the length of the particle through the radiator in cm, ε(E) is the overall collection efficiency for the Cherenkov photons multiplied by the detection efficiency for observing these photons as photoelectrons, and E is the photon energy in eV.

Although it was first discussed in a classical paper by Tamm in 1939 [12], it seems to be little appreciated that the conical Cherenkov radiation shell is not perpendicular to the Cherenkov propagation angle in a dispersive medium. The half-angle of the cone opening (η) is given by,

$$\cot\eta = \left[\left(n(\omega_0)\beta\right)^2 - 1\right]^{1/2} + \omega_0 n(\omega_0)\beta^2 \left(dn/d\omega\right)_0 \left[\left(n\beta\right)^2 - 1\right]^{-1/2}\,, \tag{3}$$

where the index of refraction $n(\omega)$ is written as a function of the angular frequency of the Cherenkov light (ω), and the frequency range is centered at ω_0. As Motz and Schiff pointed out in 1953 [13], the presence of the second term means that the cone angle (η) is the complement of the Cherenkov angle (θ_c) only for a nondispersive medium where $dn/d\omega = 0$. In dispersive optical material, the Cherenkov cone is no longer perpendicular to the direction of photon propagation, but can instead be thought of as side-slipping as it moves along with the charge.

3. The DIRC Principle

The geometry of a single radiator of a reference conceptual DIRC is shown schematically in Fig. 1. Each radiator is a long, thin bar with a rectangular cross section of transverse dimensions (t_x, t_y). A track with velocity β passing through the radiator with refractive index (n_1) emits Cherenkov radiation in a cone around the particle trajectory. The source length of the light emitting region is the particle trajectory length in the radiating material. The angles, positions, momentum (and timing) of the track are normally provided by other detectors, primarily by a tracking device located in front of the radiator, and perhaps by the crossing time of the beams in the machine. If the index of refraction of the radiating material (n_1) substantially exceeds $\sqrt{2}$, and the index of the

surrounding material (n_3) is approximately one, then for a particle close to $\beta = 1$, some portion of the light will always be transported down the bar to the end. Since the radiator cross section is rectangular, the magnitudes of the angles are maintained by reflections at the surfaces of the bar. Thus, in a perfect bar, the portion of the Cherenkov cone that lies inside the total internal reflection angle is transported undistorted down the bar to the end (except for additional up-down/left-right ambiguities).

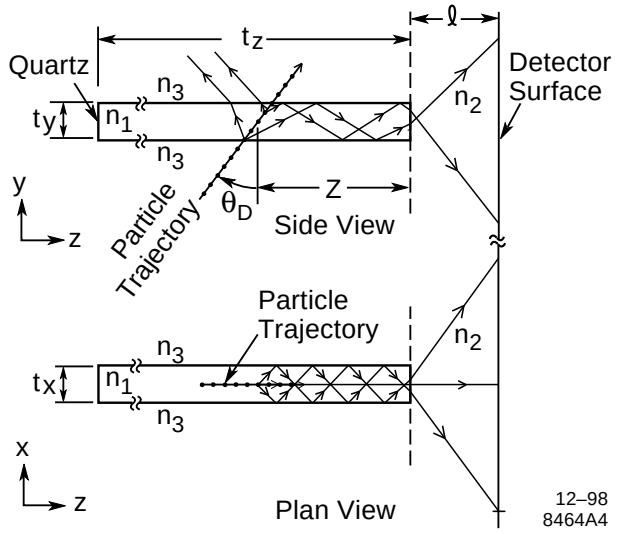

Figure 1. Schematic of a radiator bar illustrating the principle of the DIRC. The particle trajectory is shown as a line connected by dots; representative trajectories of Cherenkov photons are shown by lines with arrows.

The Cherenkov photons are imaged onto a detector located outside the particle path. Although there are only two Cherenkov emission angles (θ_c, ϕ_c) of interest for particle identification, the DIRC is intrinsically a three-dimensional imaging device.[¶] The directly measurable quantities are usually the space-position of each "hit" in a detector "pixel" (e.g., a PMT), and its associated time. The space-position provides a direct measurement of the two normal angles with respect to the end of the bar (α_x, α_y), assumed here to be corrected for refraction so that they are the angles inside the bar material. The third angle (α_z) can be calculated from the constraint. However, because of the long

[¶] A number of DIRC devices have been proposed that use less than three dimensions. For example, a 1-D device (called the CCT) that couples DIRC bars with a non-imaging detection system that times the first photoelectron(s) seen at the bar end was proposed by Honscheid *et al.* [17]. A prototype has been constructed and tested by Kichimi *et al.* [7]. Akatsu *et al.* [8] have proposed and tested a 2-D readout DIRC (one timing dimension and one space dimension) called the TOP counter.

optical delay line, the photon propagation time down the bar [(t_p), see Eq. (6) below] is also directly related to the direction cosine of the photon angle along the bar z axis (α_z). This over constraint is quite powerful in rejecting backgrounds and ambiguous solutions. It is usually only necessary to instrument one end of the bar, and reflect photons heading the "wrong" way back to the detector. The propagation time shift between the forward and backward going photons usually makes them easy to separate.

For pedagogical purposes, it may useful to write down specifically how the measured quantities are related to Cherenkov angles. Consider a frame ($\underline{k}$) where the particle moves along the (z) axis. The direction cosines of the Cherenkov photon emission in this frame ($\underline{k}_x$, $\underline{k}_y$, and $\underline{k}_z$), are related to the Cherenkov angular definition [see Eq. (1)] by,

$$\begin{aligned} \underline{k}_x &= \cos\varphi_c \sin\theta_c, \\ \underline{k}_y &= \sin\varphi_c \sin\theta_c, \\ \underline{k}_z &= \cos\theta_c. \end{aligned} \tag{4}$$

Now consider the right-handed coordinate system attached to the bar frame as indicated in Fig. 1. In this frame, we call the track polar and azimuthal angles (θ_t, φ_t). We then align the $\underline{k}$ frame x-axis such that the direction cosines of the photon emission in the bar frame can be written as

$$\begin{aligned} k_x &= -\underline{k}_x \cos\theta_t \cos\varphi_t + \underline{k}_y \sin\varphi_t + \underline{k}_z \sin\theta_t \cos\varphi_t, \\ k_y &= -\underline{k}_x \cos\theta_t \sin\varphi_t - \underline{k}_y \cos\varphi_t + \underline{k}_z \sin\theta_t \sin\varphi_t, \\ k_z &= \underline{k}_x \sin\theta_t + \underline{k}_z \cos\theta_t. \end{aligned} \tag{5}$$

The photon propagates a length (L_p), in a time (t_p), down a bar length of (L) as is given by

$$t_p = \frac{L_p n_g}{c} = \frac{L\, n_g}{c\, k_z}, \tag{6}$$

where the photon group velocity ($v_{group} = c/n_g$) must be used rather than the photon phase velocity ($v_{phase} = c/n$) since, in a dispersive medium, energy propagates at the photon group velocity. The connection between Eqs. (3) and (6) should be noted. The relationship between group and phase

velocities, as a function of photon wavelength (λ), is usually derived in a simple one-dimensional picture [14], and leads to the following relationship between the group and phase refractive indices:

$$n_g(\lambda) = n(\lambda) - \lambda \, dn(\lambda)/d\lambda \, . \qquad (7)$$

For fused silica, $n_g(\lambda)$ is typically several percent larger than $n(\lambda)$ for photons in the energy range detectable by a bi-alkali photo-cathode. As a particular example, the weighted averaged value $\left\langle \frac{n(\lambda)}{n_g(\lambda)} \right\rangle \sim 0.97$ for photons from a Cherenkov spectrum impinging on a bi-alkali photocathode after passing through a borosilicate window. The dispersion of n_g is also substantially greater.

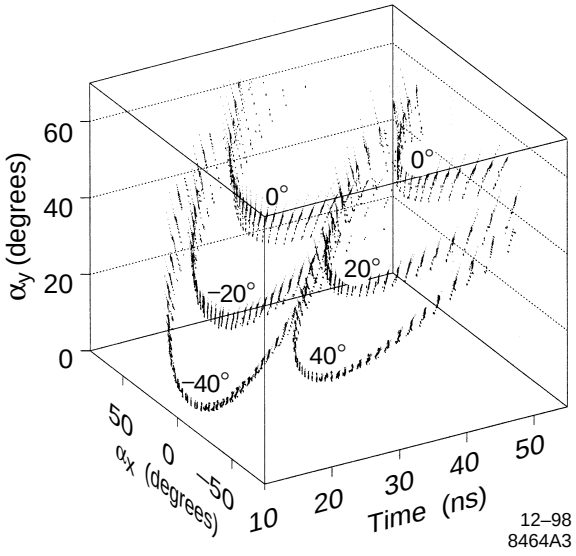

Figure 2. Three-dimensional images (α_x, α_y, t_p) of Cherenkov photons produced by tracks at dip angles of 0^o, $\pm 20^o$, and, $\pm 40^o$ in a 5-m long DIRC. Measurements are made at only one bar end, with photons reflected at the other end. The tracks enter normal to the DIRC bar, so there are no left-right ambiguities.

A simplified view of the measurement space for tracks entering a DIRC bar at three different dip angles (in a DIRC bar similar to that of the BaBar DIRC) is shown in Fig. 2.

4. DIRC Design Choices

The following sections briefly review some of the choices one must make in designing a DIRC, with an eye to providing a framework for considering some possible design directions. The BABAR DIRC design provides a basic reference set of choices. Of course, there are other options and

combinations possible, but only a few can be discussed in any detail. This discussion will focus on choices that appear to be most technically feasible.

4.1 Cherenkov Light Production

Fused silica is the logical material for the radiator, and has been used for all DIRCs built to date. It is very transparent, has a rather uniform index of refraction, modest dispersion in the visible, can be ground with sharp corners, and takes a good polish. Synthetic fused silica is also very hard against ionizing radiation. Its most serious liabilities are that it is expensive to procure and process; it has a rather short radiation length (X_0 = 12.3 cm); and it can also have small periodic fluctuations in index which can lead to diffractive effects at some transmission angles [18]. One potentially promising area to explore would be the use of plastics, particularly in an end-cap or fixed-target environment, where transmission distances can be reasonably short. This might allow a molded radiator to be made at a large savings in cost. In particular, acrylic is known to have transmission coefficients in the 10 m range for photon wavelengths above 400 nm [1,2,7]. It also has fair reflection coefficients provided that the cast surfaces can be used [7,15]. It is inexpensive to procure and has a long radiation length (X_0 = 34.4 cm), so that one can partially compensate for light loss during transmission by making the radiator thicker. However, it remains to be demonstrated whether one can obtain the index uniformity, edge sharpness, and surface and figure quality from cast surfaces to make such a detector feasible. In any case, plastic is radiation soft, which will further limit potential applications.

4.2 Cherenkov Light Transport

The principle design issue is whether the light guide width-to-thickness ratio is such that photons reflect many times in one dimension only, or in two dimensions. This issue has been discussed previously, where the different choices were called “plates” (reflection many times only in one dimension) and “pipes” (reflection many times in two dimensions) [1,2]. In a DIRC of the BaBar type, which uses “pipes,” both transverse dimensions of the radiator bar are small and the length is long, so that the precise photon path and number of bounces are lost, or at least not utilized. The image is then essentially length independent. However, since many bounces occur from all the sides and faces in this approach, a premium is placed on the sharpness of the side/face edges, since photons will get lost in the corners if the edges are not sharp. If there are many bounces from the

sides, one also depends on the orthogonality of the angles between sides and faces. On the other hand, if one dimension of the radiator is sufficiently wide, it is possible to track the photon path from production to detection in the wide dimension. An example of such a situation is an end-cap device [5]. A plate design allows the entire propagation length to be used as the standoff distance. This may improve the resolution, and the properties of the plate sides and side/face edges become less critical. However, one must then keep track of all bounces in this side-to-side plane, and the number of ambiguities will be dependent on the length-to-width ratio. Time information can be useful to help resolve these ambiguities.

4.3 Cherenkov Imaging (Focusing)

As described earlier, the direction of a photon in space is measured and then translated into a measurement of the Cherenkov angles using knowledge of the track direction. In the literature, there are shades of meaning that have been attached to the word "focusing" in the DIRC imaging process. On the one hand, it has been used to refer specifically to an optical system in which light is focused onto the detector by a reflecting lens (see, e.g., Refs. 1,2,5,8,16). On the other hand, it can be argued that all DIRC (indeed all RICH) counters must focus, in that there are no detectors in this energy regime which measure photon angles directly, and so angles must always be derived by a focusing system of some kind. In this view, the differences among imaging systems are more a question of performance properties and complexity of the focusing system employed, rather than differences in basic principles. In any event, the presence of the DIRC light guide does lead to somewhat different considerations for DIRC images than is generally the case for a RICH. In particular, two of the methods described below, the "pinhole" and "time" methods are peculiar to the DIRC.

In Fig. 3, a number of different kinds of DIRC imaging systems are demonstrated schematically, along with a simple "ball park" estimate for the resolution properties of the particular systems. Imaging can be thought of as occurring separately in each of the three dimensions (x,y, and t_p) and different schemes for each dimension can be used in the same counter. Since there are only two Cherenkov angles to be determined, in principle, measurement of only two of these dimensions are

required in any given counter. However, measurement of the third dimension is extremely useful to reject backgrounds and ambiguities, and perhaps provide Cherenkov angle measurement constraints.

The analog of the classic “proximity” focusing scheme, typically used for liquid/solid radiator RICH counters, is shown in Fig. 3(a) for the DIRC. In this scheme, the photon's angles are measured by comparing its detected position with respect to its emission point along the track. This requires knowledge of the position of the input track and the path of the photon to the detector. Note that the relevant “standoff” length may be much longer than the path in the detector box (see method (b) below), so that there could be excellent resolution per photon in the “proximity” focused direction. For example, the “standoff” for the BaBar DIRC is about 117 cm, while the bars are nearly 500 cm long. The price paid for this improved resolution is that the bar bounce ambiguities must be resolved. Excellent time resolution can help. However, to use this method in the DIRC would, in most cases, require a “plate” rather than a “pipe” for light transport.

“Proximity” focusing is related to, yet subtly different than, the “pinhole” focusing method used by the BaBar DIRC, as shown in Fig. 3(b). This later imaging scheme is a direct analogue of the pinhole camera, hence the name. In this case, the path of the photon down the bar is ignored, and the resolution is independent of the precise track location in the bar. It does, however, depend directly on the size of the bar exit aperture. The relevant standoff length becomes the distance from the bar end to the detector plane, rather than the distance from the track to the detector plane. This would normally be shorter than for the “proximity” focused scheme of Fig. 3(a).

Figure 3(c) shows one version (a single reflective lens) of “lens” focusing. Other versions of lens focusing could use refractive, gradient, or diffractive lens, but the reflective system has the advantage that it allows the same material in the focusing region as in the bars, thus maximizing the overall efficiency for photon propagation. The advantage of a focusing scheme of this kind, compared to the pinhole scheme, is that the bar size can, in principle, be removed from the resolution. One can also magnify or de-magnify the image to match the pixel size of a particular detector device.

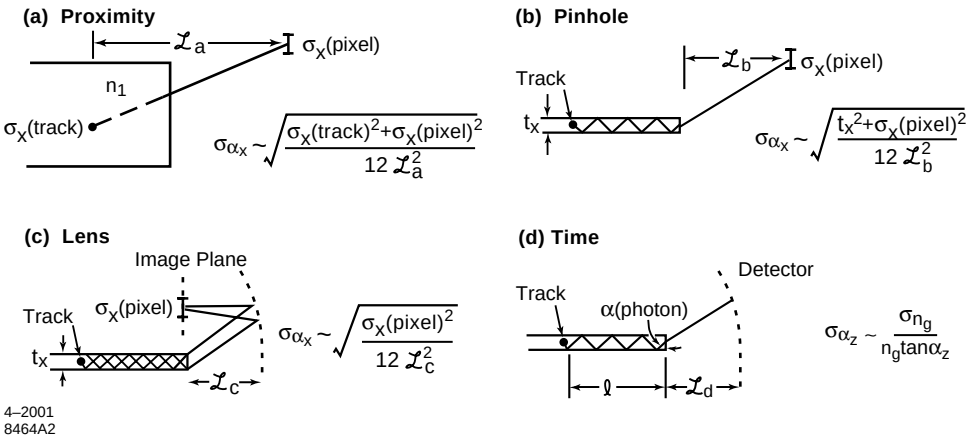

Figure 3. Illustrations of four different DIRC imaging schemes: (a) proximity (b) pinhole (c) lens (d) time. Simple estimates of the imaging and detector part of the resolution obtained on the photon angle in the projection shown are noted for each scheme. These estimates should be treated as pedagogic approximations. For simplicity, all position and detector resolutions are treated as though they are pixelized, and the indices of refraction of the Cherenkov radiator and the imaging region are taken to be the same. The time dimension resolution estimate (d) is given for the dispersion limiting case where the time measurement resolution itself is not the limiting factor. Sec. 4.3 describes the more general case.

Finally, Fig. 3(d) illustrates the principle of the timing dimension. Equation (6) shows that the direction cosine along the z-axis (k_z) is inversely related to the photon propagation time, so that one might naively think that the resolution of such an angle measurement is inversely related to the distance the photon travels down the bar. However, the dispersive component of the group refractive index is large enough to become a dominant component in many real-world cases. In the particular case illustrated in the figure legend, the time resolution per photon is assumed to be so small that the dispersion dominates the resolution of the photon "dip" angle α_z . The fractional resolution on n_g [$\delta(n_g) = \dfrac{\sigma(n_g)}{n_g}$] is about 0.015 for bi-alkali tubes, averaged over the Cherenkov emission spectrum. So in this case, the error $\sigma_{\alpha_z} \sim 0.015/\tan\alpha_z$ varies from a practical minimum of about 9 mrad for large transverse photon propagation angles ($\alpha_z \sim 60^o$) in the bar, to an infinite maximum at $\alpha_z = 0^o$, where the photon travels along the bar axis. For a typical α_z of ~ 30^o, the angular error from dispersion alone is ~ 25 mrad.

4.3.1 Timing Resolution Issues

In cases where one is attempting to use timing, either to measure the Cherenkov angle or to sort out ambiguities, the resolution obtainable can be quite complex to calculate. Not only are the angular dependences large, but there are also correlation terms between production, transport, and length dependent terms (see section 5 below). Understanding the details typically requires a full simulation of the specific counter proposed. However, for pedagogical reasons, it is worth considering a few typical cases in a simplified way to illustrate how some of these effects come into play.

4.3.1.1 BaBar DIRC

For the BaBar DIRC, the timing resolution is generally not competitive with the position resolution for the determination of the Cherenkov angles, unless the number of bounces is very large. Therefore, timing is used primarily as a background and ambiguity resolving measurement, although it is also included directly in the overall PID likelihood. The usual practice for BaBar DIRC is to plot the difference between the measured time and the propagation time (t_p), with corrections for the trigger offset and track travel time to the DIRC bars. The measured time resolution on this difference (σ_t) can then be written as

$$\sigma_t = \sqrt{t_p{}^2[\delta^2(L_p) + \delta^2(n_g)] + \sigma^2{}_{t_0}}\ , \qquad (8)$$

where $\delta(L_p) = \frac{\sigma(L_p)}{L_p}$ is the fractional resolution on the propagation length (L_p), $\delta(n_g) = \frac{\sigma(n_g)}{n_g}$ is the fractional resolution on the group refractive index averaged over the detected Cherenkov photons, and σ_{t_0} is the average resolution of the PMT tubes and electronics system (as calibrated). In the simple picture that follows, σ_{t_0} has been set to a nominal 1.6 ns. The co-variance terms have been neglected, although they could affect the time dependent piece by as much as 30% or so at some angles.

As noted above, the fractional resolution on n_g is about 0.015 for bi-alkali tubes averaged over the Cherenkov emission spectrum. This term is expected to have a small (negative) length dependence (arising from the wavelength dependent loss of photons down the bar) that has also been neglected. In the limit of where the time resolution is dominated by propagation dispersion (see the discussion of Fig. 3(d) above), the fractional time resolution is simply equal to the fractional resolution on n_g (i.e., ~80 ps/m of propagation length).

The fractional resolution on L_p is equal to the fractional resolution in k_z.

$$\delta(L_p) = \delta(k_z) \approx \frac{\sqrt{1 - k_z^2}}{\left(k_z^2\right)} \, k_{xy} \tag{9}$$

However, the analytic calculation, as shown by the last term, in terms of the measured parameters is complex and has been approximated. For simplicity, the effective resolution in the directional cosines as measured in the transverse planes (k_{xy}) has been taken to be a constant and equal in both measurement planes. For Figure 4 below, it is given the value k_{xy} = 0.0083 as derived from averaging over the two space dimensions in a pinhole-focusing model for the BaBar DIRC with a constant standoff from the bar end to the detector. Note that this calculation also requires that the projected photon length along the bar be well-known. In practice, this length is determined from the track position and bar geometry.

Figure 4 shows the resolution growth in this model as a function of propagation length for a detector similar to the BaBar DIRC. In this model, the propagation length is mostly a function of the photon propagation dip angle (k_z). Though the resolution increases substantially for long photon propagation lengths (i.e., as k_z gets smaller) and eventually becomes dominated by the term calculated in Eq. (9), the number of photoelectrons with these very long propagation lengths (>> ~2 times the minimum in each direction) is actually quite small. At a more typical value for the photon

propagation angle of $\alpha_z = 30^o$ ($k_z = 0.867$), the resolution due to the dispersion in n_g is about 5 times larger than the term given by Eq. (9).

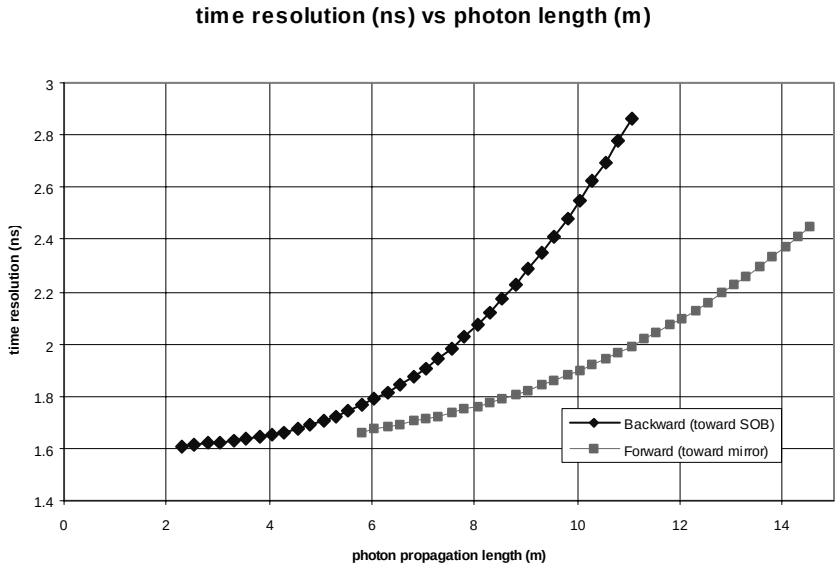

Figure 4. Results of the resolution calculation described in the text for a detector like the BaBar DIRC.

4.3.1.2 Using Time to Measure the Cherenkov Angle

It is worth looking a bit more closely at the way in which the dispersion in the group velocity can effect the measurement of Cherenkov angles when using time imaging. For illustrative purposes, it is useful to consider the special case where the track enters the bar orthogonally in both directions. In the language of equations (4), (5), and (6) we find that

$$k_x = \underline{k}_y = \sin\varphi_c \sin\theta_c,$$

$$k_y = \underline{k}_z = \cos\theta_c,$$

$$k_z = \underline{k}_x = \cos\varphi_c \sin\theta_c.$$

For specificity, consider a device that measures only the propagation time and one (x) angle, e.g.,

$$\tan\alpha_x = \frac{k_x}{k_z},$$

Then,

$$\sin\theta_c = k_z\sqrt{(\tan^2\alpha_x + 1)}.$$

The resolution on the Cherenkov polar angle per photon is given by,

$$\sigma_{\theta c}^2 = \tan^2\theta_c\left[\delta^2(n_g)+\delta^2(t_p)+\sigma_{\alpha_x}^2\tan^2\alpha_x\right].$$

As a typical numerical example, assume that

$$\tan\theta_c = 1.083, \text{ (i.e., a } \beta = 1 \text{ particle in fused silica)}$$

$$\delta(n_g) = 0.015, \text{ (i.e., a bi-alkali photocathode response curve)}$$

$$\delta(t_p) = \frac{1}{L_p}\left(\frac{100\text{ps}}{5065\text{ps}}\right) = \frac{0.02}{L_p},$$

where L_p is the photon propagation length in meters, and the photodetector resolution is assumed to be 100 ps. We also assume that $\sigma_{\alpha x} = 0.005$ rad.

Figure 5 shows the results of this calculation of Cherenkov angular resolution per photon as a function of photon propagation length. It should be noted that this particular choice of track angles (that is, zero track dip angle) is the most attractive region for measuring angles with time focusing, and there is relatively little dependence on α_x. However, one can never obtain better than about 16 mrad resolution per photon due to the dispersive component of the group index.

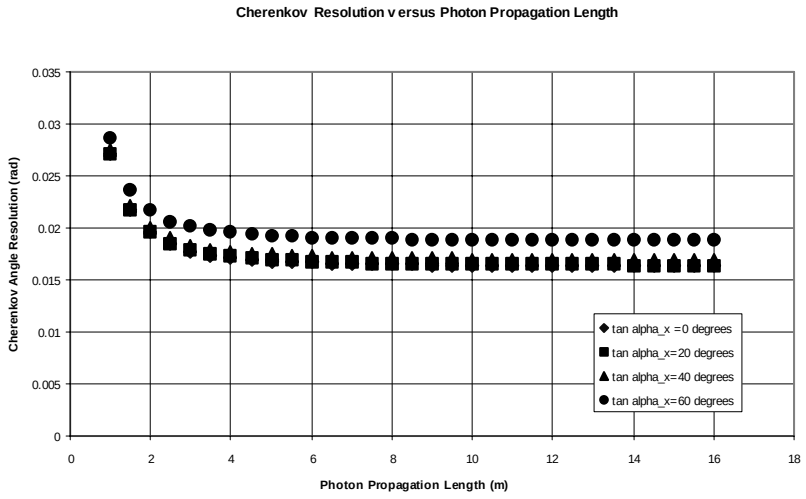

Figure 5. Cherenkov polar angle resolution versus photon propagation length for the special case described in the text. The track is entering the bar normally in both projections.

It is instructive to view the same features plotted as the measured time resolution versus the distance from the track to the detector along the bar for a number of different photon emission angles in the x-plane as shown in Fig. 6.

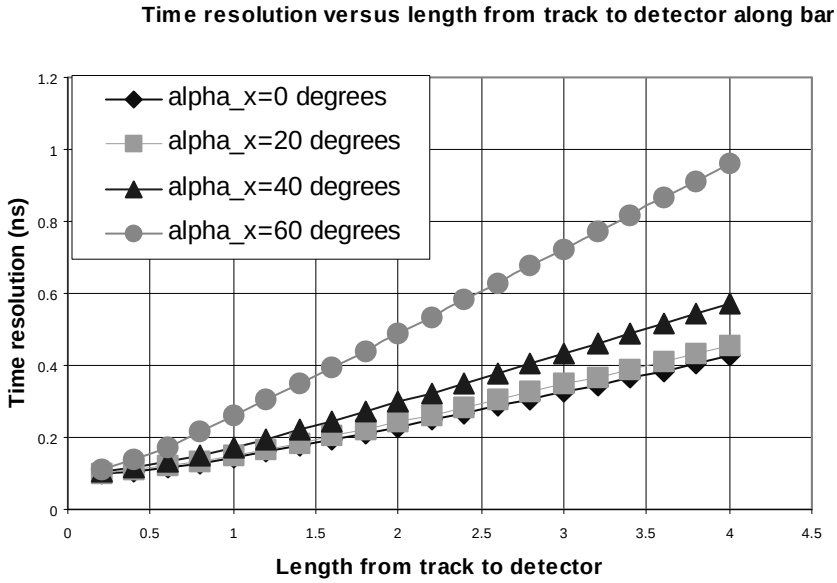

Figure 6. Observed time resolution versus length along the bar from track to detector expected for the particular case described in the text. The track enters the bar normally in both projections.

4.4 Detectors

The availability of detectors continues to be "the" crucial element for design. Conventional PMTs remain hard to beat for the price-to-performance ratio. In the last few years, metal channel PMTs have become available that may allow a more elegant "lens-focused" design. These may be becoming competitive in cost and performance, although it is not quite obvious if an adequate packing fraction can be obtained for the imaging requirements of a 3-D device. The newest flat panel PMTs by Hamamatsu [21] may provide a solution to this problem. Hybrid PMTs could also be a promising alternative for the future [19]. Other potential technologies, such as Avalanche Photodiodes [16], visible light gas detectors, VLPCs, and MCP-PMTs are more speculative. Although it is clearly difficult to imagine using a Transition Edge Sensor (TES) [20] since it requires 40 mK temperatures, it is an exciting new high-efficiency device that has the amazing feature that it can measure the energy resolution of a visible photon to about 0.15 eV. This could

reduce the chromatic term in the resolution equation by over a factor of ten (see Sec. 5.1.2 below). On the other hand, it is a slow detector, and would not allow one to take full advantage of the timing properties of DIRCs. Another way to reduce the production chromatic smearing term is described below in Sec. 5.1.2.

4.5 Combinations of Design Elements

The design elements discussed above can be "mixed and matched," but only some combinations make sense. In general, to obtain the best performance and background rejection in most modern experimental environments, it seems best to use detectors that have relatively high precision in both space and time.

As an exercise, consider the design elements of the BaBar DIRC:

1. Light production: fused silica.
2. Light transport: two-dimensional (pipe).
3. Imaging principle: two-dimensional pinhole.
4. Detector: two-dimensional in space, conventional PMT, timing used primarily to resolve ambiguities and backgrounds; nonmodular matching between detectors and bars reduces pixel count.
5. Expected performance: 4σ π-K separation to ~ 4 GeV/c (depending on track dip angle).

Another version of this counter might use similar bar-boxes to those in the BaBar DIRC but they might contain only one "plate" style DIRC bar (about 40 cm in width) with a pixilated array detector like the following:

1. Light production: fused silica.
2. Light transport: one-dimensional (plate style).
3. Imaging principle: fully 3-D; proximity focused in wide plate dimension; reflective lens focused in the narrow dimension; fast timing used to measure the chromatic term, resolve ambiguities (including the side bounce ambiguities), and resolve backgrounds (see section 5 below).

4. Detector: closely packed, fast two-dimensional pixilated Flat Panel PMTs (64 6x6mm pixels per PMT) with good timing (~100 ps; non-modular matching between detectors and bars reduces pixel count).
5. Expected performance: 4σ π-*K* separation to ~ 5 GeV/c (depending on track dip angle).

In contrast, suppose one wished to design an inexpensive DIRC for a medium energy fixed-target experiment. One might consider design elements such as the following:

1. Light production: acrylic.
2. Light transport: one-dimensional (plate) downstream of the target.
3. Imaging principle: proximity focused in the wide plate dimension; reflective focused through a molded plastic lens in the narrow pin-hole dimension; timing used mostly to resolve ambiguities and reject backgrounds.
4. Detector: metal channel PMT with 1×64 pixels (1 cm $\times$ 1 mm pixels).
5. Expected performance: 4σ π-K separation to ~ 4 GeV/c, but with limited angular coverage.

5. Resolution Issues

In a simple model, the resolution on the Cherenkov angle for a given track σ [θ_c(tot)] is given by

$$\sigma[\theta_c(\text{tot})] = \frac{\sigma[\theta_c]}{\sqrt{N_{pe}}}, \tag{10}$$

where N_{pe} is the total number of photons detected, and the angular resolution on the projected track ($\sigma[\alpha_{Track}]$) is assumed to be sufficient [$\sigma[\alpha_{Track}] << \sigma[\theta_c(\text{tot})]$ so it does not contribute to the overall resolution. The error on each individual photon $\sigma[\theta_c]$ is given in terms of the design components discussed in Section 4 as [1,2];

$$\sigma[\theta_c] = \sqrt{\sigma[\theta_{Production}]^2 + \sigma[\theta_{Transport}]^2 + \sigma[\theta_{Imaging}]^2 + \sigma[\theta_{Detection}]^2}\ , \tag{11}$$

The dominant smearing term at production ($\sigma[\theta_{Production}]$) is the so-called production chromatic term ($\sigma[\theta_{Chromatic}]$). This term arises from the fact that the refractive index $n(\lambda)$ is a function of photon wavelength, as described by Eq. (1). The value of ($\sigma[\theta_{Chromatic}]$) is about 5.4 mrad for the BABAR DIRC detector or any other detector with similar photon wavelength bandwidth. Other production smearing terms, such as trajectory distortion due to bending in the magnetic field, or multiple scattering in the radiator material are much smaller, at least at high momentum where good resolution is required to separate πs from Ks.

Transport smearing ($\sigma[\theta_{Transport}]$) may be caused by various flaws in the DIRC radiators, such as non-parallel sides, non-planar surfaces, and non-orthogonal sides and faces. Due to effects of these kinds, the resolution contribution from this term tends to grow as the square root of the propagation length. In BaBar DIRC, the most difficult effect of this kind to control was the side-to-face orthogonality, which contributes around 2-4 mrad per photon for a bar at the production specification limit. In principle, such effects can be made much smaller with different production methodology (at a higher cost), or by using a one-dimensional transport design to limit the number of side bounces.

It is convenient to consider the last two terms ($\sigma[\theta_{Imaging}]$, $\sigma[\theta_{Detection}]$) together. The basic principles have already been described in section 4.3. In principle, angular resolution derived from positional information can be made "arbitrarily" good to match requirements for a particular performance limit. In particular, the imaging component that comes from the bar size in a pin hole focusing scheme, such as the one used by BaBar, can be made small with lens focusing, and the number of detector pixels and the standoff distance are essentially arbitrary choices. It makes economic sense to choose focusing methods and detector configurations that balance the various resolution components.

Excellent single photoelectron time resolution is required to contribute in a meaningful way to equivalent single photon angular resolution. For example, for a BaBar-style DIRC, one needs a time resolution of about 200 ps per photon to be somewhat (i.e., within about a factor of two)

competitive with the positional photon information for a track at a zero degree track dip angle (see Figure 5). At larger track dip angles, the performance will be less competitive. Because of the chromatic dispersion in the travel time, it is not feasible (at least with the detection bandwidth of a bi-alkali PMT) to obtain a much better resolution from the time dimension, unless the photon wavelength can be measured (see below).

5.1 DIRC Performance Limits

For a $\beta \approx 1$ particle of momentum (p) entering a radiator with index of refraction (n), the number of σ separation (N_σ) between particles of mass (m_1) and (m_2) is approximately

$$N_\sigma \approx \frac{\left(m_1^2 - m_2^2\right)}{\left(2p^2\sigma[\theta_c(\mathrm{tot})]\sqrt{n^2-1}\right)}. \qquad (12)$$

The large index of refraction in the DIRC radiator makes the term $\sqrt{n^2-1}$ rather large (at least compared to gas radiators). Thus, the DIRC will have good performance only in the low and medium momentum regions. In particular, obtaining good resolution much above 4 GeV requires excellent angular resolution. For example, 4σ separation between pions and kaons requires a resolution on $\sigma[\theta_c\ (\mathrm{tot})]$ of about 1.5 mrad at 4 GeV/c, and about 0.25 mrad at 10 GeV/c.

The fundamental limits on the DIRC technique are primarily (1) N_{pe}; (2) chromatic smearing; and (3) practically, but less fundamentally, systematic limits on bar production quality and alignment. In the following, we briefly review how one might mitigate each of the first two components.

5.1.1 Photon Statistics

In principle, one could increase the bar thickness to increase the photoelectron number, although this would increase the material in the particle's path. Solid-state detectors could also attain two to

three times the photon detection efficiency of typical PMTs, and thus increase the number of photoelectrons observed substantially. However, in itself, an increase in statistics leads to a rather modest improvement in performance since the resolution only improves as the square root of the number of photons, in the best case. As an example, consider a very optimistic case where the transverse angles are sufficiently well measured that the individual photon resolution is dominated by the 5.4 mrad per photon production chromatic smearing of a fused silica radiator, working with a bi-alkali photocathode with a borosilicate window, and where the radiator is sufficiently thick to give 100 photoelectrons. Even so, the 4σ separation limit between πs and Ks is just above 6 GeV/c.

5.1.2 Mitigating Chromatic Smearing

It seems impractical to apply chromatic correction in the focusing system, or to find a radiator with significantly less dispersion than fused silica. However, the high efficiency of a solid-state detector could allow one to reduce the energy range of accepted Cherenkov photons. Somewhat counter-intuitively, this can actually improve the total resolution substantially in a DIRC designed so that the chromatic term dominates, even though such a restriction limits N_{pe} substantially. For example, the total contribution $\sigma[\theta_c\ (\text{tot})]$ from the chromatic term is reduced by a factor of 2.5 when the photon energy range is restricted between 600 and 450 nm compared to the case where all photons between 600 nm and 300 nm are accepted, even though the number of photons observed is reduced by nearly a factor of four!

The “ideal” solution to the chromatic smearing would be a detector that measures the photon energy directly. In principle, the TES device described above could do this, but is slow and would be very hard to implement. It seems more practical to use the large dispersion of n_g, as described earlier, to measure the photon wavelength directly in a 3-D DIRC [22]. That is, by comparing the individual photon flight time with its measured angle, the photon wavelength can be calculated. This allows the refractive index at production to be rather precisely calculated so that the chromatic piece of the production term can be substantially reduced. Figure 7 shows that the measurement of photon wavelength done is this way can be quite accurate if the time resolution is good (100ps). Looked at in the Cherenkov angle space, this is equivalent to reducing the smearing due to chromaticity to less

than 0.2 mrad for a photon travel length of 6 m. The large chromatic dispersion of the group velocity actually works in one's favor in this case!

In fact, even with a time resolution like that of BaBar (~1.6 ns), one can measure the ~5.4 mrad chromatic production term to ~200 %/L(meters) (i.e., for typical lengths of 3-6 meters, ~3.6-1.8 mrad). Of course, this reduction in the chromatic term is not very helpful in the present BaBar DIRC, as the precision of the angular measurement is dominated by the imaging piece.

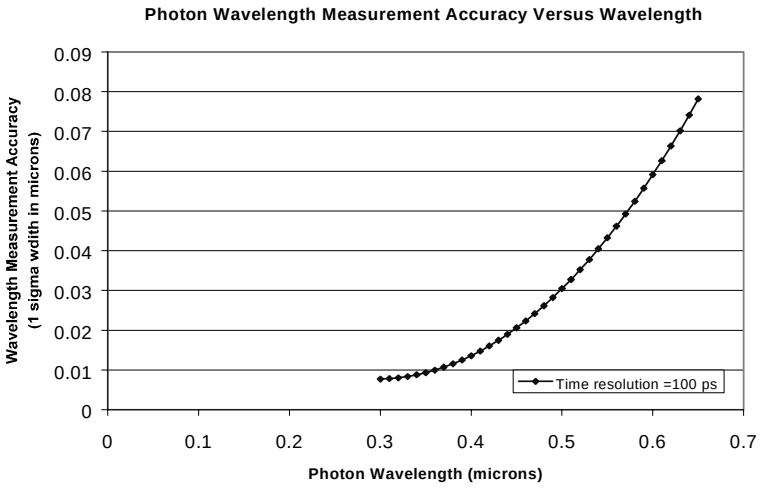

Figure 7. Resolution on the wavelength measurement versus wavelength per detected photon for an assumed time resolution of 100 ps at a propagation length of 6 meters. This calculation assumes that the transverse propagation angles (α_x, α_y) are sufficiently well measured that the time resolution is the only important term.

6. Summary

DIRCs are robust, fast particle identification devices, well-suited to high-radiation environments. The first generation BaBar DIRC has been operating with colliding beams since May 1999, with performance that is quite near that predicted from Monte Carlo simulation. The design of elegant second generation DIRCs either for new experiments or possible upgrades to BaBar depends greatly on the availability of appropriate photon detectors. Though such detectors would allow more

flexible designs, the momentum range of application for DIRCs is inherently limited. The "natural" momentum separation range for good π/K separation in a DIRC is up to about 4-5 GeV/c. It is plausible, but quite difficult, to increase this range by another factor of about two.

ACKNOWLEDGMENTS

I would like to thank all of the members of the DIRC BaBar collaboration, whose work to build and then analyze data from this new device has been instrumental to increasing my understanding of essential features of this type of detector. I would like to give special thanks for discussions on specific items addressed in this paper to Dave Aston, Richard Blankenbecler, Mark Convery, Gautier Hamel de Monchenault, Andreas Hoecker, David Leith, Brian Meadows, Al Odian, Moishe Pripstein, Jochen Schwiening, Stephan Spanier, Jaroslav Va'Vra, Christophe Yeche, and Marco Zito.

BIBLIOGRAPHY

1. B. Ratcliff, BaBar NOTE 92; "The B Factory Detector for PEP-II: A Status Report", published in Proceedings of the International Conference on High Energy Physics, 1889-1896 (1992); and SLAC-PUB-6047 (1993), published in Tsukuba B Factories, 331-341 (1992).
2. P. Coyle *et al*., Nucl. Instrum. and Methods A **343**, 292 (1994).
3. D. Aston *et al*., IEEE Trans. Nucl. Sci. **42**, 534-538 (1995) and SLAC-PUB-6731 (1994).
4. C. Lu *et al*., Nucl. Instrum. and Methods A **371**, 82-86 (1996).
5. T. Kamae *et al*., Nucl. Instrum. and Methods A **382**, 430-440 (1996).
6. H. Staengle *et al*., Nucl. Instrum. and Methods A **397**, 261-282 (1997).
7. Kichimi *et al*., Nucl. Instrum. and Methods A **371**, 306-310 (1994).

8. M. Akatsu *et al*., DPNU-99-08 (1999), and T. Ohshima, Nucl. Instrum. and Methods A **453**. 331-335 (2000).
9. See, for example, J. Schwiening *et al*., SLAC-PUB-8590 (2000), invited talk presented at 30th International Conference on High-Energy Physics (ICHEP 2000) Osaka, Japan, and I. Adam *et al*., Nucl. Instrum. and Methods A **453**. 301-307 (2000).
10. See, for example, G. Lynch, B. Ratcliff and J. Veillet, private communication.
11. B.N. Ratcliff and S. Spanier, Nucl. Instrum. and Methods A **433**, 456-463 (1999).
12. I. Tamm, J. Phys. U.S.S.R. 1,439 (1939).
13. H. Motz and L. I. Schiff, Am. J. Phys., **21** 258-259 (1953).
14. See, for example, J. D. Jackson, "Classical Electrodynamics", 4th Ed., 211(1965).
15. G. Kettenring, Nucl. Instrum. and Methods **131**, 451-456 (1975).
16. R. Wilson, Nucl. Instrum. and Methods A **433**, 487-491(1999).
17. K. Honscheid, M. Selen, and M. Sivertz, Nucl. Instrum. and Methods A **343**. 306-310 (1994).
18. I. Adam *et al*., SLAC-PUB I -7707, Nov. 1997, and IEEE Trans.Nucl.Sci.45: 450-455 (1998).
19. A. Braem *et al*., Nucl. Instrum. and Methods A **433**, 153-158 (1999).
20. B. Cabrera *et al*., Applied Physics Letters **73**, 735-737 (1998).
21. Hamamatsu Photonics K.K., http://www.hamamatsu.com/.
22. This approach has been broadly discussed within the BaBar DIRC group, and has been particularly emphasized by Brian Meadows.

Corrosion of Glass Windows in DIRC PMTs

P. Bourgeois[1] and J. Va'vra[2]

1: Cente d'Etude de Saclay, DA{NIA-SPP, F91191 Gif-sur-Yvette CEDEX, France
2: Stanford Linear Accelerator Center, Stanford University, Stanford, CA 94309, USA

Abstract

The DIRC photon detector contains ~11,000 photomultipliers (PMTs), which are submerged in ultra-pure water. This note reports on glass corrosion R&D conducted with PMTs in pure water. We conclude that only a limited number (~50) of the PMTs in water are affected by rapid corrosion, while a majority of the 11,000 PMTs should last, according to our measurements, for another ten years. The observation of PMT glass corrosion is based on visual observations, X-ray surface analysis, ESCA surface analysis, weight analysis, transmission measurement, as well as detailed water trace element analysis. We also correlate these observations with DIRC measurements of water pH factor, resistivity, temperature, transmission, and BaBar analysis of Bhabha and di-muon events. We also compare DIRC water purity with that of the Super Kamiokande and K2K experiments, which also use ultra-pure water. We provide empirical proof that corrosion, in our particular Borosilicate type of PMT glass window, occurs at high rate when the glass has no Zn content.

1. Introduction

DIRC is using EMI 9125FLB17 1.125" diameter PMTs made by Electron Tube Ltd. (ETL). The PMT front glass window is made of B53 Borosilicate glass (also called E53C). B53 is specified as a low background glass because it has no potassium (K). One should also add that the front glass is different than the side glass (see Section 6). There is ~11,000 PMTs of this type in the photon detector. The PMT front windows are sitting in water to minimize photon losses. The front window is only 1.2 ± 0.1 mm thick. The window type and its thickness were chosen to maximize a response at very low wavelengths. In retrospect, DIRC could have used a thicker window because the EPOTEK-301-2 optical epoxy, used to glue quartz bars together, cuts the wavelength acceptance below 290 nm. However, that was not initially realized.

In principle, ultra-pure water is very corrosive because it is hungry for ions. This creates certain electrostatic pressure pushing a migration of ions from any surface surrounding water. Therefore, when designing an experiment in water, one has to worry about corrosion of all components, including the vessel (in DIRC we call it the SOB, for standoff box), plumbing, and glass windows of PMTs. The pure water is required in an experiment such as DIRC to reach good optical transmission in 1 m of length, as well as a bacteria-free environment.

Examples of experiments using a large number of PMTs submerged in ultra-pure water are the DIRC, Super Kamiokande, K2K, SNO, Sudan, Milargo, etc. Typically, the PMTs are submerged in water to minimize photon losses due to windows and couplings.

It is certainly tempting to argue at this point that there is already enough experience running glass PMTs in clean water, and therefore one does not have to worry, arguing PMT manufacturers already know. Unfortunately, this argument is incorrect. We have found that there is a relatively low level of understanding, from a theoretical point of view when questions are raised about under what such condition a glass will corrode. However, since several experiments have been running for the past 3-4 years with very large number of PMTs in water, the relevant empirical experience is slowly emerging, and DIRC certainly will contribute to the data in this area. Nevertheless, we would always recommend performing exhaustive corrosion tests for a particular choice of glass formulation.

When the DIRC vessel (SOB) was opened and drained in October 1999, we noticed that many of the PMTs front glass windows had a "milky" or "frosty" appearance. Figure 1 shows examples of corroded PMTs, and, for comparison, one that is clear. We found that only the glass face was corroded, i.e., the PMT sides were not affected at all. The "frosty" PMT had deep surface fractures resembling a frosty window in winter. The "milky" surface appears to be slightly cloudy, and visible only under direct light. For example, if a "milky" PMT is

submerged in water, the problem is almost unnoticeable. This is because water provides good optical coupling even to corroded surfaces. A "frosty" PMT is slightly more noticeable in water. We did a visual accounting[1] of all affected PMT in the entire SOB during the October shutdown, and the result is that about two-thirds of them are in the "milky" category, and the number of "frosty" PMTs is ~50. One should also point out that to date, we do not have an independent account of the number of bad PMTs, i.e., verified by the manufacturer.

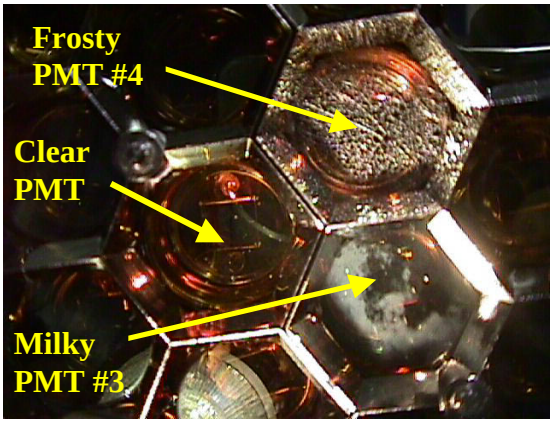

Figure 1. Example of a "milky" PMT (labeled as #3), and a "frosty" PMT (labeled as #4), observed in the SOB during October 1999, when water was drained out of the vessel.

A subsequent DIRC data analysis found no deterioration of the relative efficiency of the "milky" or "frosty" PMTs compared to "clear" PMTs, which confirms that water provides a good coupling to these surfaces. In fact, a lab test on a "frosty" PMT yielded normal results, i.e., no after-pulsing, which would indicate worsening vacuum. The long-term behavior of relative efficiency is still being investigated.

We have removed a number of "frosty" and "milky" PMTs from the SOB during the October 1999 shutdown, for subsequent surface analysis at the ETL Company, Saclay, and SLAC. We briefly outline the sequence of various major developments:

(a) First, by using an electronic microscope at SLAC, the problem was identified as glass corrosion of the PMT front window, characterized by a depletion of sodium ions [2].

(b) ETL confirmed this explanation by measuring the glass composition after immersion in hot water and comparing it to the nominal composition [3,4]. The measurement is done by X-ray fluorescence. The X-rays probe the surface composition to a depth between 10-100 μm. Results are given in Table 1. The surface composition of the glass has been modified as a result of immersion for 31 days at 83.5°C. In particular, the fraction of alumina, boron, and silicate (Al_2O_3, B_2O_3 and SiO_2) constituents has increased after immersion because other constituents, and especially sodium, have been leached from the surface layer.

(c) Most importantly, ETL discovered that the "frosty" PMTs were in fact those PMTs, which had mistakenly received a window made out of the wrong material [3,4]. The glass material had no zinc, and was identified as X-glass (or E47.2-type glass, which is used by ETL for other applications), instead of the nominal B53 glass, which is required for its better resistance to corrosion when submerged in the ultra-pure water. A subsequent test conducted at SLAC using the ESCA analysis confirmed that indeed the "frosty" PMTs had no zinc in the first 50Å below the surface [5]. Table 1, provided by the ETL Company, gives the glass composition before and after immersion of the wrong type of glass in water. For this glass, not only the sodium, but also the boron was depleted. The company found that windows made out of X-glass are already frosty after five days of being submerged in hot water at 83.5°C, which corresponds according to ETL, to about 5 months at ambient temperature, as we discuss later. This is a crucial result on which to base

[1] The determination of what PMT should be labeled "milky" versus "frosty," as well as locating them in the SOB, was done by J. Va'vra and A. Hoecker during the October 1999 shutdown [1]. Unfortunately, to this date, there is no other direct source of information on how many PMTs are affected. For example, after one year of operation the DIRC data analysis, is still unable to distinguish which are the "clear," "milky," or "frosty" PMTs. Similarly, the PMT manufacturer did not provide the information of how many PMTs were made out of the "wrong" type of glass.

the argument that the SOB PMTs, made out of X-glass have already become “frosty” by the time of the October 1999 shutdown, and therefore, we count all.

(d) Tests performed in Saclay verified the ETL scaling law of glass corrosion in B53 material. Even more importantly, the Saclay data shows a loss of the PMT detection efficiency, which could be explained by either the window transmission degradation, the quantum efficiency loss, or gain drop. The loss of the detection efficiency may be consistent with a 2-3% loss of photons we seem to detect in DIRC data from BaBar, both in the Bhabha and the di-muon events.

(e) Many other tests at Saclay, ETL, and SLAC were performed to check for overall consistency.

Table 1. ETL Co. analysis of B53 and X-glass windows under various conditions.

Component	B53 glass ref. glass [% by wt]	B53 glass immersed for 30 days, 83.5°C	B53 glass normalized to SiO_2 **	X-glass ref. glass	X-glass immersed for 30 days, 83.5°C	X-glass normalized to SiO_2 **
SiO_2	62.70	66.10	62.70	69.60	92.40	69.60
NaO_2	7.50	1.00	0.95	8.70	0.90	0.68
Al_2O_3	6.80	7.30	6.92	4.20	5.10	3.84
ZnO	2.90	2.70	2.56	0.00	0.000	0.00
BaO	3.10	2.40	2.28	0.00	0.20	0.15
CaO	0.70	0.80	0.76	0.00	0.70	0.53
B_2O_3 *	15.90	19.10	18.12	17.20	0.00	0.00
Total	99.60	99.40	94.29	99.70	99.30	74.80

Notes: * Fitted by difference

** Normalized to maintain the SiO_2 composition constant.

2. Tests Performed at the Electron Tube Ltd. (ETL)

2.1. Overview

This section describes tests performed at ETL [3,4]. The goal of the study is to quantify the rate of material loss of the glass in order to answer the question of whether the PMTs could survive ten years in the DIRC SOB vessel without imploding. The study was performed in hot de-ionized water in order to accelerate their aging effect. The acceleration factors applied have been measured by a separate study.

In addition, X-ray fluorescence analysis of the immersed and non-immersed glass windows has been used to measure the composition of the glass in order to improve the understanding of the weight loss mechanisms, as already mentioned in the introduction.

2.2. Experimental Setup

2.2.1. “Thirty Day” Trial

B53 (also called E53C by ETL in these tests) glass window samples (2.93cm dia. and 0.12cm thick) were immersed in de-ionized water for 31 days at 83.5°C. The windows were positioned flat on the base of an immersed perforated polypropylene beaker to enable the whole surface area of the window to be exposed to attack by water. The de-ionized water was changed daily. First, water in system A was replaced with fresh de-ionized water from our in-house supply. Then the water in system B was replaced with water previously in system A. System A had four B53 windows immersed in de-ionized water with a mean conductivity of 6.21 $\mu S.cm^{-1}$, and a pH, measured at 20°C, of 7.26 ± 0.14. The system B had also four B53 windows, immersed in “24-48 hour aged” water with a mean conductivity of 12.80 $\mu S.cm^{-1}$, and a pH, measured at 20°C, of 7.12 ± 0.02. A non-immersed window was used as a reference standard for weighing purposes.

2.2.2. “Five Day” Trials

Three B53 glass windows and three X-glass windows (also called E47.2 by ETL) were immersed in de-ionized water for a period of five days at various temperatures in the range of 30°C to 85°C. The B53 samples

were immersed at temperatures of 73.0 and 82.6°C and the X-WINDOW samples were immersed at temperatures of 33.2 and 73.0°C. The mean conductivity was 3-12 $\mu S.cm^{-1}$.

The apparatus was similar to the one used for the 30-day test with the exception that windows were fixed in position and mounted vertically using polypropylene fastenings in order to maximize exposure of both faces to attack by water. Also, glass types were separated based on composition and the de-ionized water was not re-cycled between beakers.

2.3. Results and Analysis

2.3.1. Results for B53 Glass Windows – "Thirty-Day" Immersion Trial

The weight loss in system B is greater than the weight loss in system A throughout the experiment, and this is likely to be due to the greater conductivity of the water in system B; however, the increased dissolution rate is relatively small (10-30%). The dissolution rate decreases by a factor of 2.5 to 3 during the experiment. A possible explanation is that the weight loss mechanism evolves from rapid ion exchange with the water-electrolyte into slow dissolution of the lattice.

Taking the average weight loss per day per unit surface area of B53 glass as $1.36\ 10^{-05}$ $g.day^{-1}.cm^{-2}$ for system A (the surface area of the tested windows is $14.6cm^2$), and the surface area of a typical window sealed onto a PMT tube as $7cm^2$, then the weight loss for the active surface area of the window is 0.1 mg/day at 83.5°C or 0.005% of the typical mass of a window (2 grams). This is equivalent to an average daily loss of thickness of 57 $nm.day^{-1}$, or 0.005% of the original window thickness (see Table 2).

Table 2. Weight loss of B53 glass windows (mg).

	Day 0	Day 10	Day 21	Day 31	Uncertainty
Average weight of window (A)	1 946.44	1 943.27	1 941.48	1 940.29	0.05
Average weight of window (B)	1 903.92	1 899.61	1 897.66	1 896.27	0.05
Ave. weight loss / window /day (A)		0.317	0.163	0. 119	0.01
Ave. weight loss / window /day (B)		0.431	0.178	0. 139	0.01

2.3.2. Results for B53 and X-Glass Windows – "Five Day" Immersion Trials

As the dissolution of glass is generally slow at ambient temperature, it is conventional to measure the glass dissolution rate V at more than one elevated temperature T. The results can then be modeled using the Arrhenius equation in order to derive the activation energy Q for dissolution of the glass: $V = V_0 \exp(-Q/RT)$, where V_0 is the baseline dissolution rate and R the universal constant. So a plot of lnV against 1/T produces a straight line graph of slope -Q/R. The acceleration factor at increased temperature is deduced and then used to predict the performance of the glass at ambient temperature.

The measurements performed at different temperatures are shown in Table 3.

Table 3. Average weight loss per window and per day after five days immersion (mg).

	33.2°C	73.0°C	82.6°C	Uncertainty
X-glass window	0. 32	2.87	N/A	0.02
B53 glass window	N/A	0.33	0.64	0.02

Table 4 presents a comparison of the dissolution rate results for B53 windows during the five-day and thirty-day immersion trials at ~83°C. The dissolution rate for the five day immersion trial is higher than the rates measured in the thirty-day trial. This is as expected as the five-day trial will favor the initial ion-exchange weight-loss mechanism that will be faster than lattice dissolution. The analysis of the dissolution rates using data from the thirty day trial uses the average dissolution rate for simplicity, though it is noted that more sophisticated models of the dissolution rate could be constructed from these results.

Table 4. Average dissolution rates for B53 glass windows for the "five day" trial at 82.6°C and "31 day" trial at 83.5°C (10^{-5} g.day^{-1}.cm^{-2}).

5 day trial		31 day trial				
5 days	uncertainty		Days 0-10	Days 10-21	Days 21-31	uncertainty
82.6°C			83.5°C	83.5°C	83.5°C	
4.40	0.12	(A)	2.17	1.11	0.82	0.06
		(B)	2.95	1.22	0.95	0.06

Results for the activation energy and acceleration factors for the B53 and X-glass windows are calculated from the five day immersion study and summarized in Table 5. The reference temperature used for the calculation of the acceleration factor **AF** is T_{ref} = 20°C.[2] We can calculate an accelerator coefficient **c** allowing the calculation of the acceleration factor at different temperatures with regard to a given reference temperature by the following formula:

$$AF(T) = c^{((T-T_{ref})/10))} \qquad c = AF(T)^{(10/(T-T_{ref}))}$$

Table 5. Activation energy **Q**, accelerating factor **AC,** and acceleration coefficient **c**.

Temperature **T**	Activation Energy **Q**	Acceleration Factor **AF**	Acceleration Coefficient **c**
[°C]	[kJ/mol.]		
B53 glass			
82.6	71.2	170	2.27
X-glass			
73.0	485	21	1.78
83.5		34	

2.3.3. Pressure Test

ETL selected ten PMTs and removed 2% of the front window thickness using air jet alumina powder. These ten PMTs were then immersed in water for one hour at 2.8 atm and survived the test. According to the manufacturer's experience, this test is equivalent to more than 20 years of operation at normal pressure. This principle has been used by the SNO experiment to test the strength of their large PMTs.

2.3.4. Tests determining that the "Frosty" PMT glass is a wrong type of glass.

TLC immersed six PMTs in 84°C water with partial circulation (three PMTs in the first tank, and the other three in the second tank. Daily fresh water was added in the first tank and old water went into the second tank). Voltage was off during this test. In addition, four B53 glass coupons were placed in the first tank, and four B53 coupons into the second tank. The tests lasted 30 days. At the end of this period, five PMTs were partially "milky" and one PMT was "frosty." The window coupons were slightly "milky" on both surfaces. The window coupons showed no transmission loss (measured in Saclay), and QE of one "milky" PMT (S/N262438) showed no significant change. However, QE of the "frosty" PMT (S/N 268885) was significantly different from the measurement before water exposure. In addition, the weight loss in the windows was ~6g/m^2, and the weight loss of the "frosty" PMT was ~90g/m^2. Table 6 shows the chemical composition of various glasses as measured by back-scattered X-rays.

The column labels in Table 6 have the following meaning:

(a) B53 is data sheet composition of a B53-type glass,
(b) A is B53 glass from the batch supplied to the DIRC group (not immersed in water),
(c) B is B53 glass from the batch supplied to the DIRC group (after 30 days in water at 84°C),
(d) X is "low background" glass used in other PMT types at ETL,
(e) C is from "frosty" window cut off from PMT S/N268885 after 30 days in water at 84°C (inside surface),
(f) D is from "frosty" window cut off from PMT S/N268885 after 30 days in water at 84°C ("frosty" outside surface).

[2] The SOB water-return temperature is typically 26-28°C.

Table 6. Chemical composition of different PMT glasses used in ETL tests:

Analysis	B53	A	B	X	C	D
SiO_2	65.5%	62.7%	66.1%	69.6%	74.3%	92.4%
NaO_2	7.7	7.5	1.0	8.7	7.9	0.9
Al_2O_3	6.2	6.8	7.3	4.2	4.1	5.1
ZnO	2.0	2.9	2.7	0.0	0.0	0.0
BaO	3.0	3.1	2.4	0.0	0.0	0.2
CaO	0.5	0.7	0.8	0.0	0.0	0.7
B_2O_3	15.0	15.9	19.1	17.2	13.3	0.0

The conclusion from tests (e) and (f) is that the "frosty" PMT window (S/N 268885) is not B53 glass (it has no Zn) and is most probably X-glass. According to ETL, the B53 glass turns "milky" with the loss of sodium, while the "frosty" window has lost sodium and boron. **Therefore, it is argued that some DIRC PMTs turned "frosty" because a small number of X-glass windows mistakenly were mixed with the B53 glass windows in the DIRC PMT production.** Thus far, the company has not produced an independent estimate indicating how many PMTs with the "wrong" type of glass are in the DIRC. Figure 2 shows (see also section 2.3.5) the extent of the corrosion in "frosty" and "milky" PMT windows (cross-sectional view). One can clearly see that the "frosty" corrosion is much larger. The "frosty" window shows a uniform depth of attack up to 15% of the window thickness after 30 days in 84ºC water. The depth of the attack on the "milky" window is entirely concentrated on the surface and it is too thin to be resolved optically even after 30 days in 84ºC water. Figure 3(a) shows that there was no effect on the QE measurement of "milky" PMTs; however, there was some effect on "frosty" PMTs, as seen on Fig. 3(b). Figure 4 shows a correlation between the "frosty" PMTs removed from the SOB in the October 1999 shutdown and ETL's serial numbers. It would appear that the largest group came as a cluster or two, which indicates a bad batch and a continuous problem.

(a) (b)

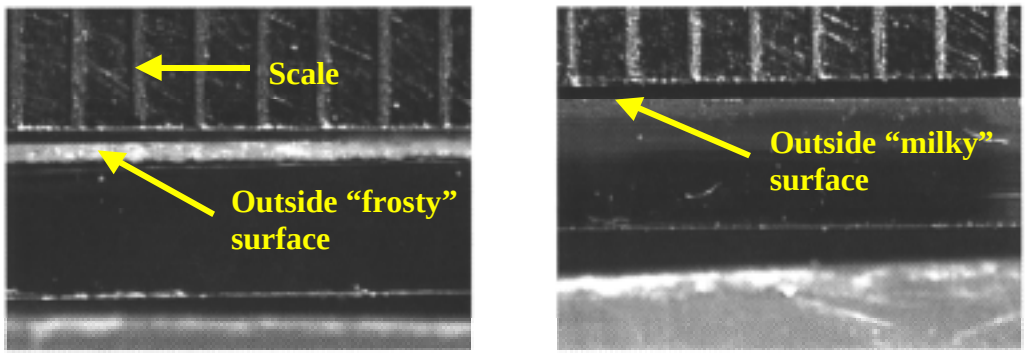

Figure 2. (a) Image of a sectioned X-glass window cut from a PMT after immersion in de-ionized 83.5°C water for 31 days. The thickness of the frosted region is 0.018 cm. (The rule spacing is 0.5 mm). The crazed edge is observed at the top. (b) Image of a sectioned B53 window cut from a PMT after immersion in de-ionized 83.5°C water for 31 days. There is no evidence of penetrative etching of the glass. The "milky" side is on top.

2.3.5. Discussion of ETL Results

The acceleration factor and the weight loss data from the five day trials can be used to calculate that 0.7% of the B53 window thickness will be lost after immersion for ten years at 20°C. If the weight loss data from the 31 day trials is used with the same acceleration factor, then approximately 0.1% of the window thickness will be lost. The difference between these two predictions is most probably due to the changing mechanism of weight loss from the glass as a function of time from ion exchange to congruent lattice dissolution. As ETL considers that there is a significant risk of implosion if greater than 50% of the window thickness is lost; there is

negligible risk of failure for PMTs with B53 windows. This is confirmed by the image of a sectioned B53 window, which shows no etching after 31 days at 83.5°C, equivalent to 14 years at 20°C [see Figure 2(b)].

X-ray fluorescence analysis of the surface of X-glass windows has shown that ion exchange or penetrative etching, as shown on Figure 2(a), dominates the weight loss mechanism. The X-ray analysis has been combined with the five-day weight loss measurements and the relevant acceleration factor to derive the 10 year etch depth as 48% of the original window thickness. Given that the calculated acceleration factors may vary depending on the local environment, the calculations suggest there is a sizeable risk of failure of the X-glass windows after 10 years.

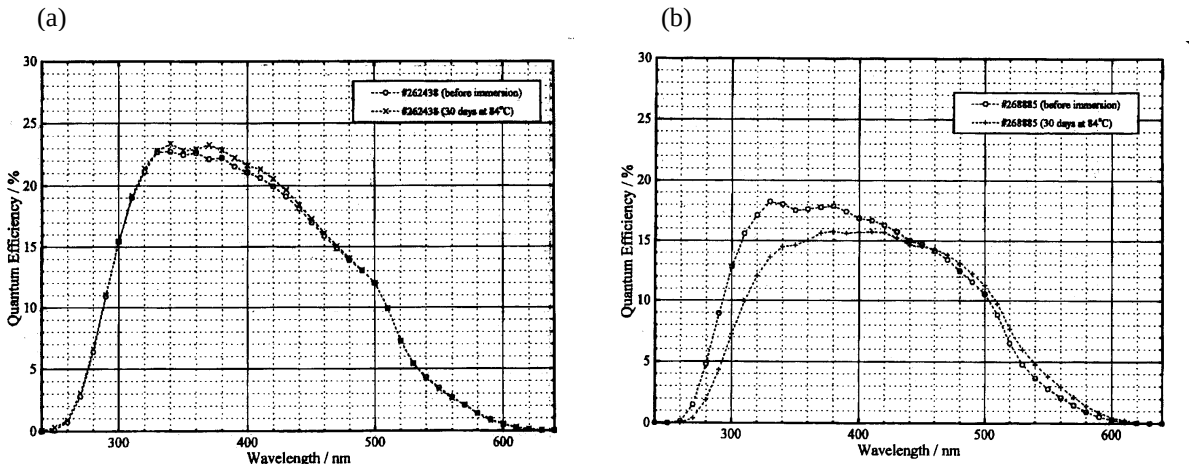

Figure 3. (a) No effect on measurement of QE of "milky" PMT exposed to water at 84°C for 30 days.
(b) Some effect on measurement of QE of "frosty" PMT exposed to water at 84°C for 30 days.

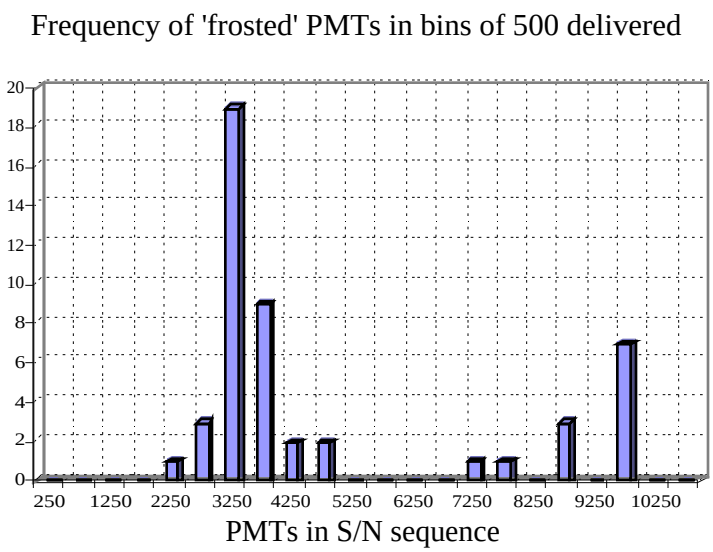

Figure 4. ETL company's estimate how the "frosty" PMTs taken out of SOB correlate with serial number production. It appears that most of them came as one bad batch.

2.3.6. Conclusion of ETL Tests

The acceleration factors calculated from the five-day immersion trials predict that PMTs with B53 glass windows will loose less than 1% of the window thickness after a 10 years immersion at 20°C. Therefore, there is no significant risk of envelope failure for PMTs with B53 windows.

The analysis of X-glass windows shows that up to 50% of the window thickness may be compromised after immersion for 10 years at 20°C. Therefore, there is a sizeable risk of implosion after 10 years for PMTs with X-glass windows. It is likely that the etching rate may vary in differing environments, so it is suggested that a PMT with an X-glass window could be removed and sectioned to determine the local etch rate.

The analysis of DIRC "frosty" PMTs shows that the front window glass has the same composition as the X-glass, which were mixed with the B53 windows in DIRC PMT production by mistake. The X-glass has no Zn, which causes excessive depletion of Na and B elements, and subsequent corrosion. The "milky" PMTs are made of the correct B53 glass, which has tolerable rate of corrosion over 10 years in BaBar. This means that out of 10 800 PMTs in SOB, only 50 are made of wrong glass.

According to ETL's test results, all "wrong glass" PMTs would turn "frosty" by the time of the October 1999 shutdown, i.e., we would have counted them all. This is an extremely important statement because we do not have an independent method to estimate how many of the X-glass windows we have in the system.

4. Tests Performed at Saclay

4.1. Overview

This section describes tests performed at Saclay [4]. Glass corrosion was not the main worry of the DIRC group initially, assuming that the manufacturer understood such problems well at this point of time, and we can simply specify when ordering PMTs [6]. Saclay performed only tests related to water pollution triggered by the PMT's material, and the emphasis was made on the helium tests and the sensitivity to the magnetic field [7]. Initial PMT glass corrosion tests were performed in parallel to the light-catcher coating corrosion and the socket gluing tests in Orsay. No obvious visual effects on the PMT front glass were observed at that time. After the October 1999 discovery of PMT front-glass corrosion, one PMT from the Orsay sample was also analyzed at SLAC. It was found that there was indeed sodium depletion in the front-glass window; however, the glass was obviously the B53 glass, and did not suffer from the gross corrosion. In retrospect the problem, judged by visual observation only, would not have been discovered during the Orsay tests.

The main emphasis in the tests performed at Saclay was in the area of photo-detection, and to also check for weight and transmission losses.

4.2. Experimental Setup: Water Station

The need to understand the long-term PMT glass behavior over 10-years of operation required that corrosion studies be performed in hot water in order to accelerate the effect, similarly to the above mentioned ETL tests. This method is typically used in industry to study chemical and mechanical characteristics of glass. For temperature increase by every 10 °C, an acceleration factor of 2-2.5 is obtained. This factor is entirely empirical, depending on what we are studying. In the Saclay tests, we have used a factor of two as a conservative acceleration coefficient (see Section 4.3.2). As we discussed in Section 2.3.1, ETL Co. empirically measured the acceleration factors of 2.3 and 1.8 for the B53 and X-glass respectively, based on the weight loss rates at different temperatures.

A small ultra-pure water station, with a recirculation capability, is used in the Saclay tests. The water is filtered, de-ionized and goes through an UV lamp to kill bacteria. The water resistance at the inlet of the test container, with no circulation, is ~4 MΩ, and ~18 MΩ after the purification. For comparison, the DIRC SOB water resistance is between 8 (return from SOB) and 18 MΩ (supply to SOB). We also measure the resistance and pH factor of water samples taken from the PMTs stainless steel vessel, containing seven PMTs, in similar geometry as in the DIRC.

The temperature in the purification station could not exceed 40°C. In order to keep the water temperature at sufficiently high levels inside the vessel, recirculation was not continuous. Instead, only 3 hours three times a day initially, and later only once a day after having tested that the water quality stays good enough (checking that the resistance is greater than 1 MΩ, and no bacteria peak absorption is observed in the water transmission).

The vessel has been put in a thermostatic box and we periodically measured the temperature at different levels (see Fig. 5). The supply water resistance was 19 MΩ, and 1MΩ to 10 MΩ in the vessel. The pH factor was close to seven after water purification, and about 6-7 in the vessel.

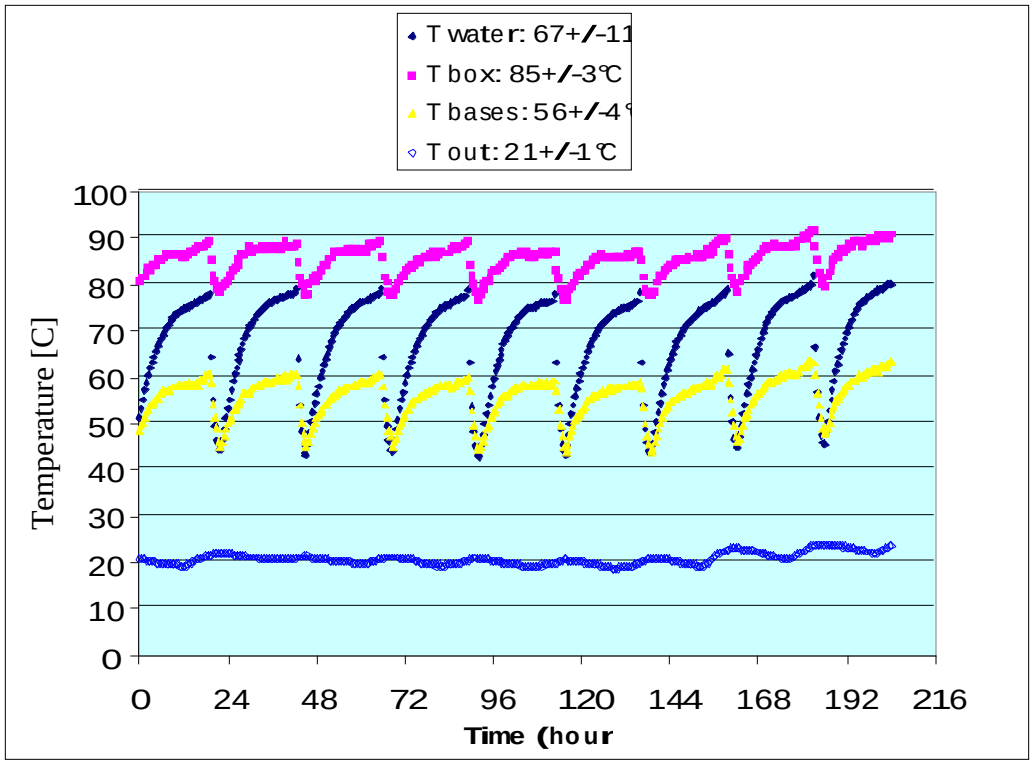

Figure 5. Temperature evolutions between two measurements on the PMTs, the average value of the water temperature has been used to determine the acceleration factor.

4.3. Experimental Setup: Measurement of PMTs

The seven PMTs were immersed in hot water and illuminated in the same manner as the DIRC PMTs during the calibration procedure [8,9,10]. We have used a blue LED, pulsed at 1kHz. To facilitate the measurement, we did not work at the single photoelectron level, but instead work with more than 10 photoelectrons in a Gaussian mode using directly the average value of the peak. To check the possible fluctuation of the LED, the light has been split and we have used a monitoring PMT (2020) at room temperature. The high voltage of the different PMTs (1140 to 1380 V) has been adjusted to have approximately the same LED amplitude. The LEDs were switched only during the measurement, but the PMTs have always stayed on.

The PMT gain correction due to temperature variation was calibrated out using a single-photoelectron peak measurement shown in Table 7 and Fig. 6, because of a possible PMT gain change towards the end of its life.

Table 7. PMT gain correction as a function of temperature.

PMT #	Slope (%/°C)
1	-0.55
2	-0.50
3	-0.33
4	-0.59
5	-0.37
6	-0.31
7	-0.34

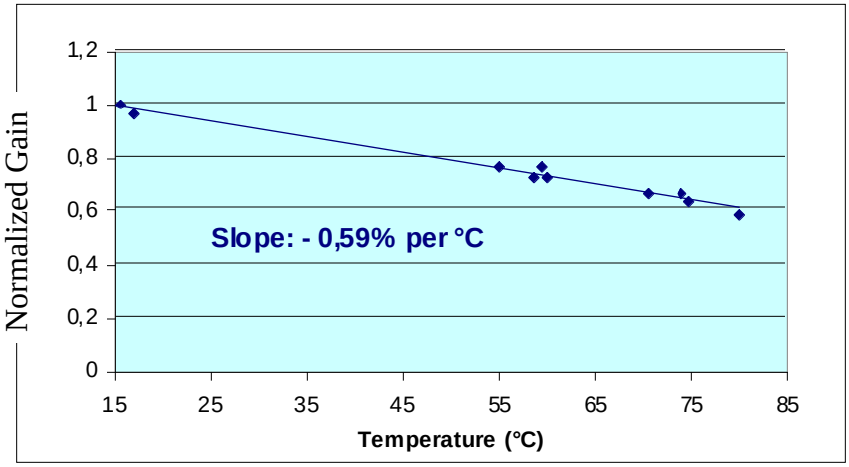

Figure 6. Normalized PMT gain versus the temperature of the water in which it has been immersed.

4.4. PMTs Corrosion Results

For this test, we have used nine PMTs, which are listed in Table 8. Two PMTs, #3 ("frosty") and 7 ("milky"), were tested at the St. Gobain Company who analyzed the composition of the glass confirming the results of ETL.

Table 8. PMTs used in Saclay glass corrosion tests.

PMT #	PMT serial number	Origin
1	264829	Clear PMT removed in IR6
2	259755	Clear PMT removed in IR6
3	268882	Frosty PMT removed in IR2
4	255830	Milky PMT removed in IR2
5	268886	Frosty PMT removed in IR2
6	258106	Clear PMT from Orsay
7	258203	Clear PMT from Orsay
3'	268887	Frosty PMT removed in IR2
7'	050372	ETL free PMT sample grounded at Orsay

Table 9. Saclay PMT glass corrosion test results.

Run	Start of test	End	Time (days)	Mean temp. (°C)	Accel. Time (months)	Observations
1	11/09/99	12/20/99	40	66.8	17	End of test of PMTs # 3 and 7
2	01/16/00	02/16/00	30	66.6	12	Start of test of PMTs # 3', 7' and four B53 windows
3	02/17/00	06/27/00	131	63.5	62	Death of PMT # 7' (grounded) Water changed on 03/23/00
4	06/28/00	07/28/00	29	66.2	11	Death of PMT # 5 (frosty)

The tests started in November 1999 and ended in August 2000. The "grounded" PMT #7' was dead after 110 days (a 52-month equivalent, with the SOB at 28°C). At the end, and before its death, PMT #5, labeled as "frosty" in the SOB, started displaying the "Christmas tree" effect,[3] which lasted about ten days. This caused

[3] "Christmas tree" is a condition when a PMT starts shining light uncontrollably. ETL explains that such condition may occur when either a PMT vacuum is slightly compromised or internal breakdown occurs [11].

some loss in PMT response due to loss of gain[4] and efficiency. However, we cannot be certain if the loss is due to quantum efficiency loss, or due to transmission loss given that the photon flux was not calibrated absolutely. Table 9 shows corrosion test results prior to the "Christmas tree" effect.

We have taken pictures of PMTs at different stages of the corrosion test - see Figures 7-10. One can see that four clear PMTs become rapidly milky, followed by scratches appearing on the window surfaces. The "frosty" PMTs become progressively frosted, spreading to the edges of the window. One can also see that the characteristic color of the photocathodes disappear on the dead PMTs, as if the surface was wet.

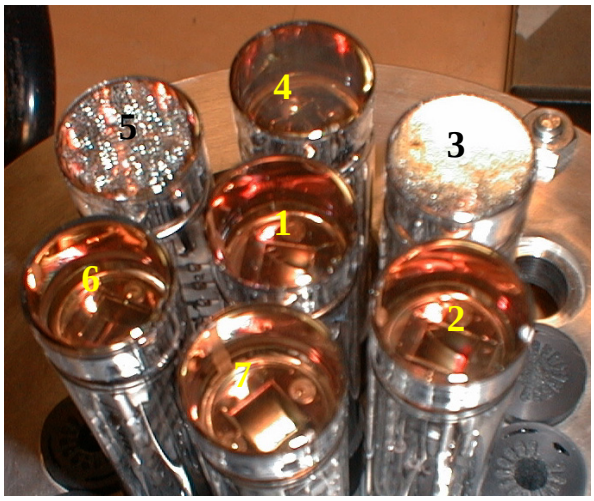

Figure 7. Appearance of seven PMTs, as the beginning of the corrosion test. One can see four "clear" PMTs on the bottom, two "frosty" on each side, and one "milky" at the top right-hand side.

Figure 8. The same PMTs as in Fig. 7, after the first immersion in hot water for up to 40 days (equivalent to 17 months at 28°C). Notice that the four "clear" PMTs shown in Fig. 7 became "milky."

[4] PMT 9125 aging, which is a slight decrease of output in time, is due to: (a) when the PMT is on, the dominant mechanism is a gain change approximately linear with the charge drawn. Typically the gain decreases to 50% after an anode draws a charge in the range of 200-400 Coulombs. (b) when the PMT is off, the quantum efficiency also degrades with the same 200-400 Coulombs at half-life. Given that the cathode current is many orders of magnitude smaller than the anode current, the loss of quantum efficiency is usually negligible in comparison to the gain [12].

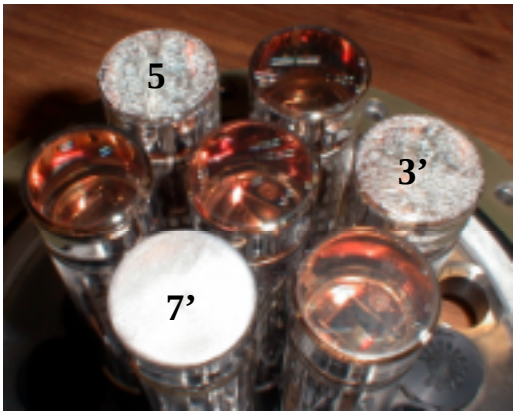

Figure 9. The same PMTs as in Fig. 7, after the second immersion in hot water for 30 days (equivalent to 12 months at 28°C). Scratches appeared on four “milky” PMTs, and edges of the “frosty” PMT # 5 also became “frosty.” It is the first immersion for PMT #3’ and 7’.

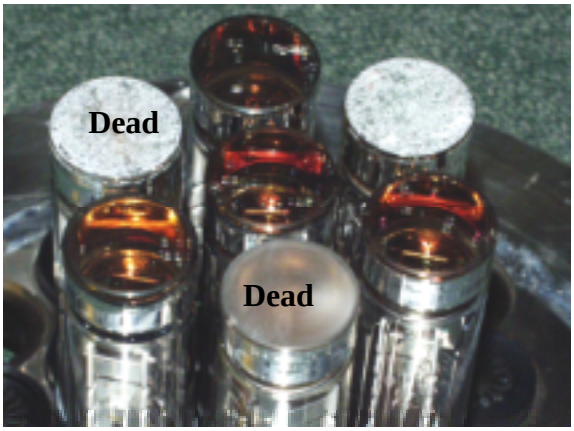

Figure 10. The same PMTs as in Fig. 7, after the third and fourth immersion in hot water for 174 days (equivalent to 82 months at 28°C); it is the second and third immersion for PMT #3’ and 7’. There are more scratches on four of the “milky” PMTs and the “frosty” PMT appears much more “frosty” when dry.

The results of the detection efficiency measurements with the LED flasher are summarized on Fig. 11. The data shows an overall drop in response, although one can see an initial increase in several PMTs. This increase is not entirely understood. One possibility is that some of the PMT front-glass was not entirely clean and the pollution washed away slowly (these PMTs were used at CERN in another test). A reason why we believe in this hypothesis is that the PMTs kept in clean conditions, such as the PMTs removed from the SOB, did show the initial rise in response. A less likely, although still a possible explanation of the initial increase in response, is that the PMTs operated at high temperature during the test and some developed instability due to the evaporation of photocathode and/or coating of other surfaces. In any case, after certain point in time, all PMTs show a gradual drop in response to the LED photon flux (PMT #3 showing the smallest slope). The time used in Fig. 11 is the accelerated time calculated by using the mean temperature and the acceleration factor of two per 10°C, taking 28°C as a reference temperature of the SOB. Using the mean temperature between two measurements introduces a systematic error of about 25% (we have done the exact calculation on 200 hours and found an accelerated time of 164 days instead of 131 days calculated with the mean temperature). Another point is that we have also used one acceleration factor for two different types of glasses.

Table 10 summarizes the results shown in Fig. 14, taking only the downward trend into account. The PMTs with B53 glass have an efficiency loss of 0.16-0.51% per month, which would translate to a loss of response of 19-61% in ten years. The loss in response is not only due to the window transmission loss but probably also due to photocathode aging. The gain change was corrected using a single-electron gain measurement.

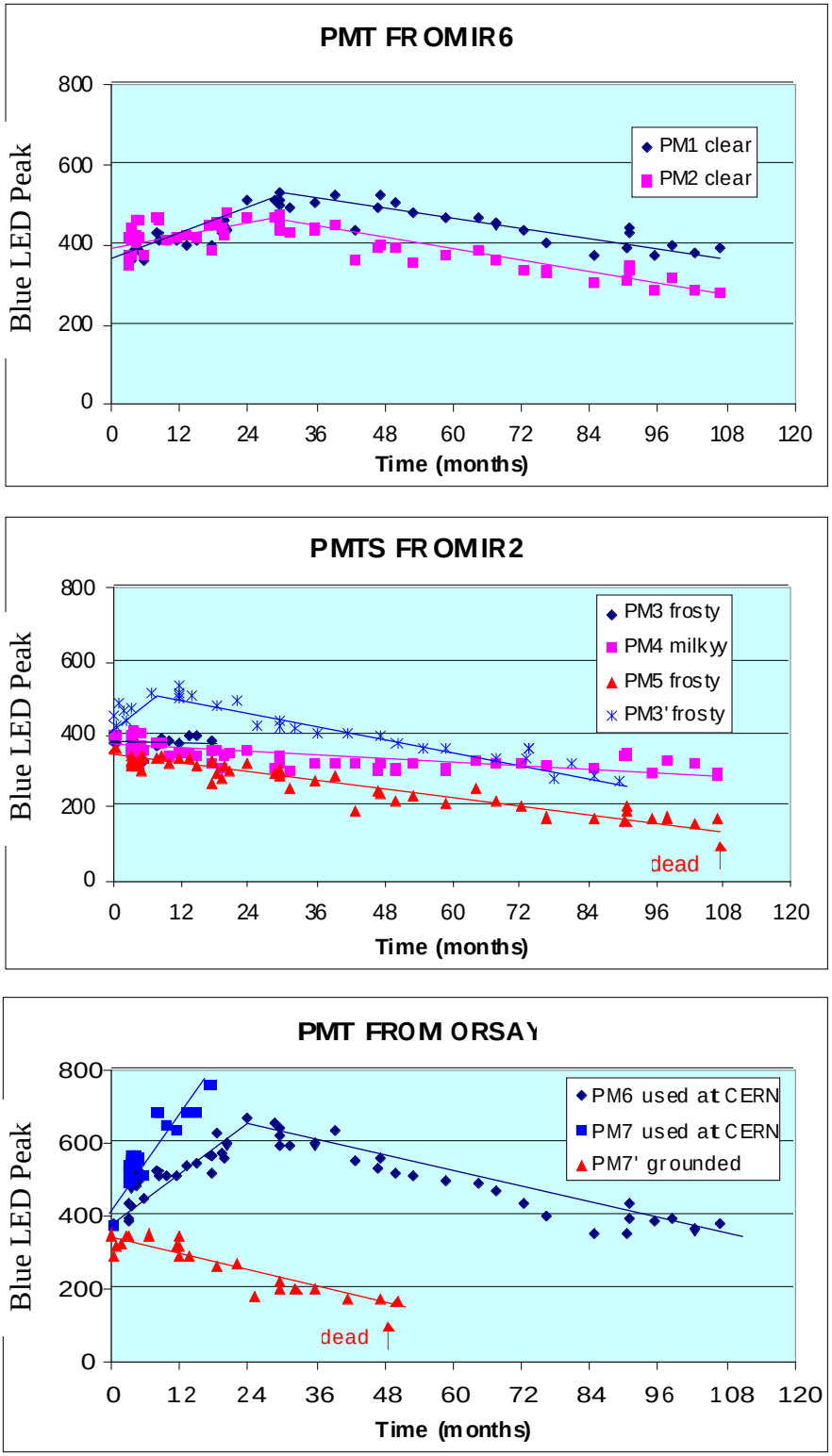

Figure 11. The PMT detection efficiency change as a function of time. Time was scaled to the SOB temperature of 28°C (taking into account the acceleration factor). The PMT response was measured using the blue LED producing ~10 photoelectrons on average.

Table 10. Slope describing the downward trend in PMT efficiency in Fig. 11.

PMT #	Condition	Slope (%/month)
1	Clear, then milky	-0.33
2	Clear, then milky	-0.39
3'	Frosty	-0.48
4	Milky	-0.16
5	Frosty	-0.53
6	Clear, then milky	-0.51
7'	Grounded	-0.96

Figure 12 shows that average number of Cherenkov photoelectrons per ring, as reconstructed from the Bhabha events, droping steadily as a function of the BaBar run number with a slope of 2-3%/year [13]. A similar result, shown in Fig. 13, was obtained from the di-muon events [14]. Both of these results confirm that we are probably dealing with a real loss of efficiency in the DIRC detector. Although these two results are still preliminary, it suggests a possible correlation with the Saclay results shown in Fig. 11.

The PMT gain drops after a certain accumulated anode charge is collected. For example, we can estimate the average anode charge assuming a BaBar run of 12 months duration, rate of 100kHz/PMT, the average single photoelectron pulse of ~25mV amplitude and 10ns duration, on a 50 Ohm load. We obtain the total anode charge of ~8 Coulombs per PMT per year. If we use the information disclosed [12] in Footnote 4, we may be actually consistent with the measured 2-3% efficiency drop shown on Figures 12 and 13, i.e., the observed efficiency drop is due to the PMT gain drop, i.e., due to a dynode aging process. If the efficiency loss is due to the PMT gain loss, and as long as it is only 2-3% loss per year, it can be easily corrected by a voltage adjustement. However, allowing large charge doses, for example the "Christmass tree" effect, for a long period of time could be dangerous. On the other hand, the cathode accumulated charge is a tiny fraction of the anode charge (for the above example is only ~4.6×10^{-7} Coulombs/year), which indicates that we are probably not dealing with cathode quantum efficiency drop at BaBar.

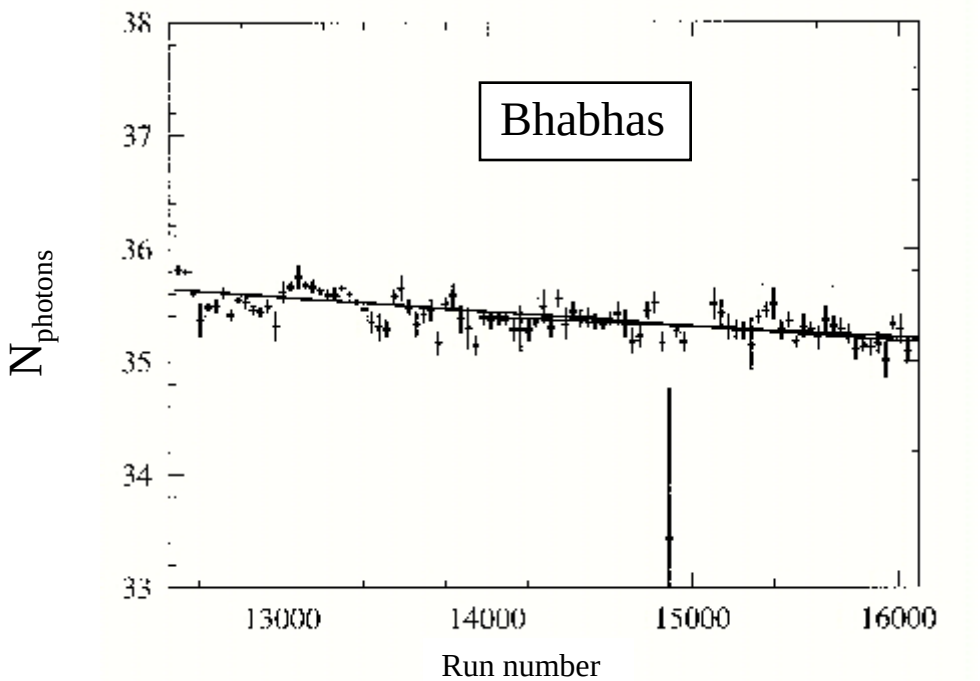

Figure 12. Average number of Cherenkov photons per ring from Bhabha analysis as a function of the BaBar run number [13]. The decline is consistent with 2-3%/year.

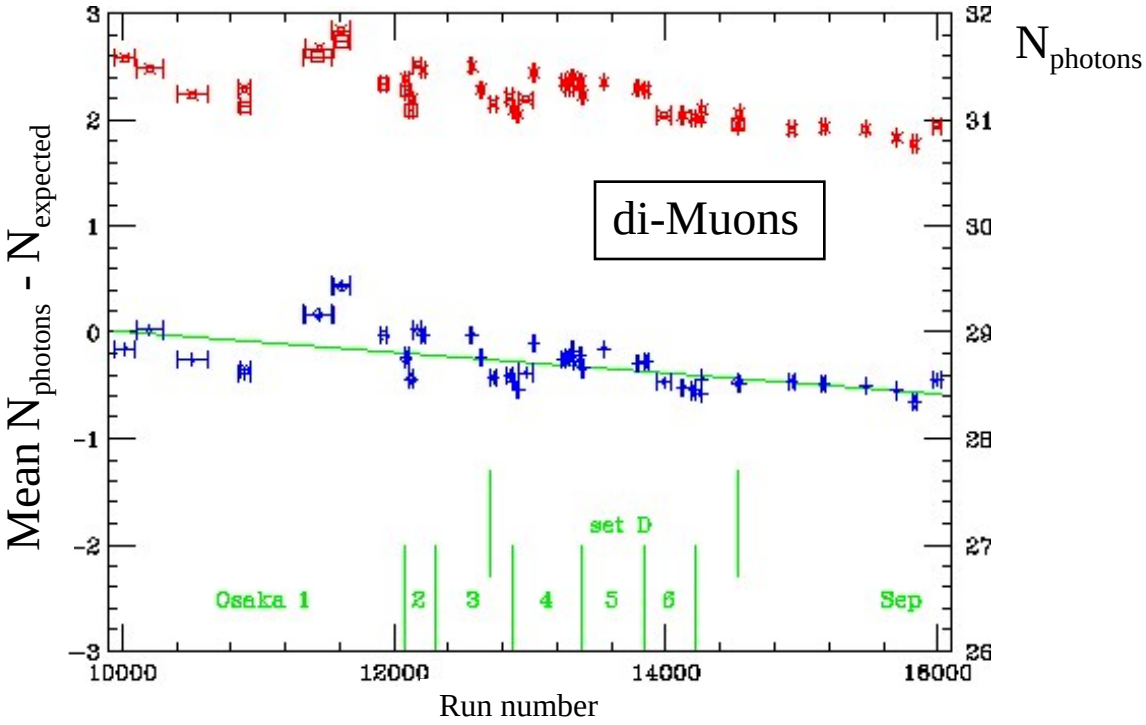

Figure 13. Average number of Cherenkov photons per ring from di-muon analysis (x points) as a function of the BaBar run number [14]. The figure also shows a relative difference from the expected number (+ points). Both curves indicate a decline at a level of 2-3%/year.

4.5. Weight and Transmission Loss

The weight loss measurement was done using front window coupons of B53 glass obtained from ETL Co. Four coupons were placed vertically in the PMT vessel, attached to three pieces of PVDF hose used for the water system, as shown in Figure 14.

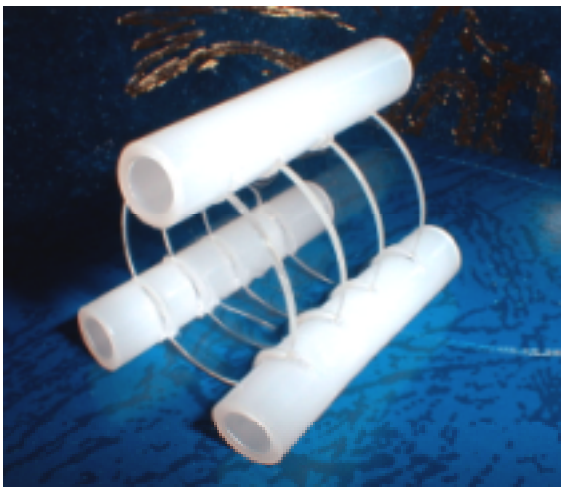

Figure 14. Four B53 glass window coupons with supports.

We have performed two kinds of measurements: (a) the weight loss using a 0.1mg accuracy scale (Sartorius), and (b) the transmission loss between 200 and 850 nm (the spectrometer was made by Perkin Elmer

Co., Model Lambda 16). We have also taken pictures which show milky spots only at the beginning and at the level of the hose contact, then more and more scratches (see Fig. 15).

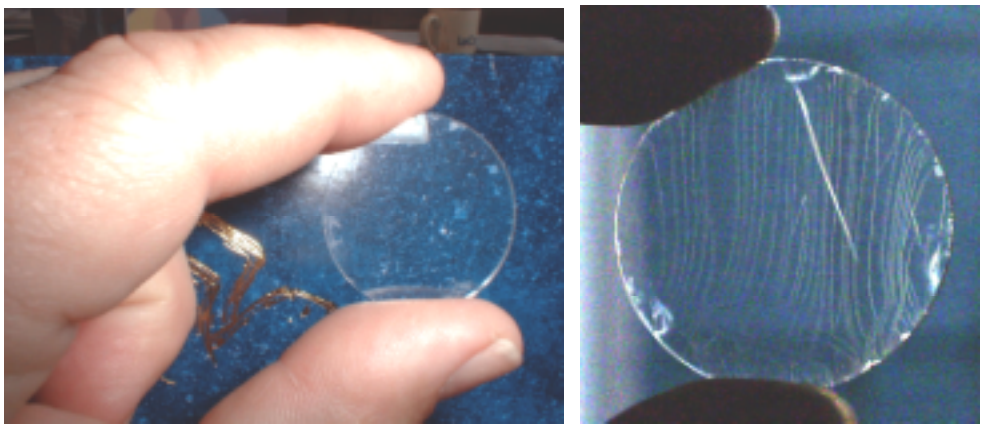

Figure 15. (a) B53 glass window coupon after the first immersion in water, and (b) after the third immersion.

4.5.1. Weight Loss Measurements

Our results compared with those of ETL are not in complete agreement given that testing was not done in the same experimental conditions. For example, the temperature is higher in the ETL data, and the ETL water resistance is lower. Figure 16 and Table 11 summarizes the results of the measurements. The equivalent SOB time has been calculated with an acceleration coefficient of two, and a reference temperature of 28°C; this gives ETL an acceleration factor of 50. However, ETL's conclusion is still valid, i.e., the PMTs equipped with the B53 glass should not implode in 10 years of running.

(a) (b)

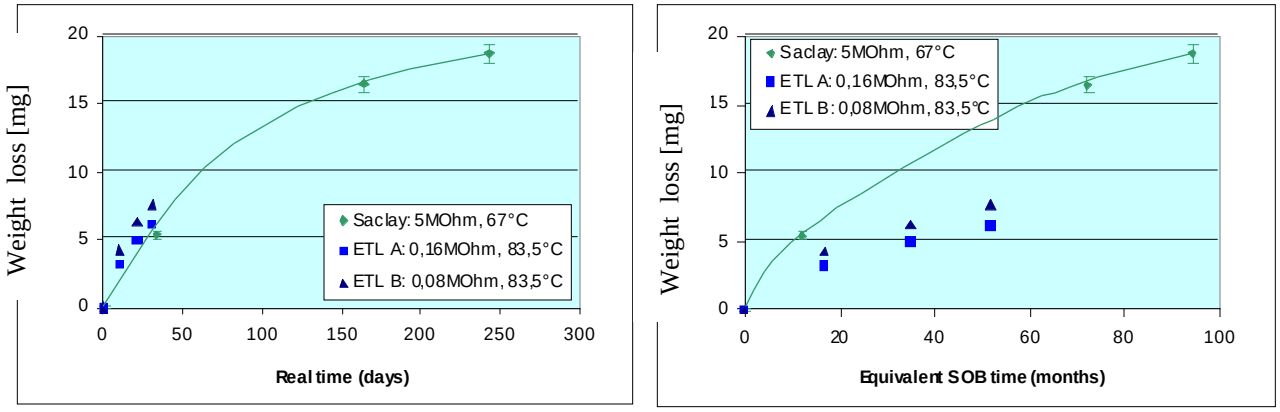

Figure 16. B53 glass coupon weight loss as a function of (a) the real time and (b) the SOB equivalent time.

Table 11. B53 glass coupon weight loss measurements at Saclay and ETL.

SACLAY				ETL			
Real Time (days)	SOB Time (months)	Weight Lost (mg)	Error (mg)	Real Time (days)	SOB Time (months)	A (mg)	B (mg)
0	0	0.0	0.2	0	0	0.0	0.0
33	12	5.4	0.3	10	17	3.2	4.3
164	72	16.4	0.6	21	35	5.0	6.3
243	94	18.6	0.7	31	52	6.1	7.6

4.5.2. Transmission Measurements

Figure 17 shows the transmission loss as a function of wavelength for a reference glass coupon as well as one of four coupons immersed in hot water at different periods of time. Figure 18 shows the mean transmission loss (averaged over four coupons) at three wavelengths as a function of time. Note that corrosion takes place on both faces, so the transmission loss is greater here than in the SOB. Another important point is that the measurements were not done with water directly coupled to the corroded surface, which would definitely improve the transmission, even though the surface is visibly corroded. In that sense, this is a less important result, which is not directly applicable to the DIRC analysis. It only indicates that the glass surface is indeed corroded.

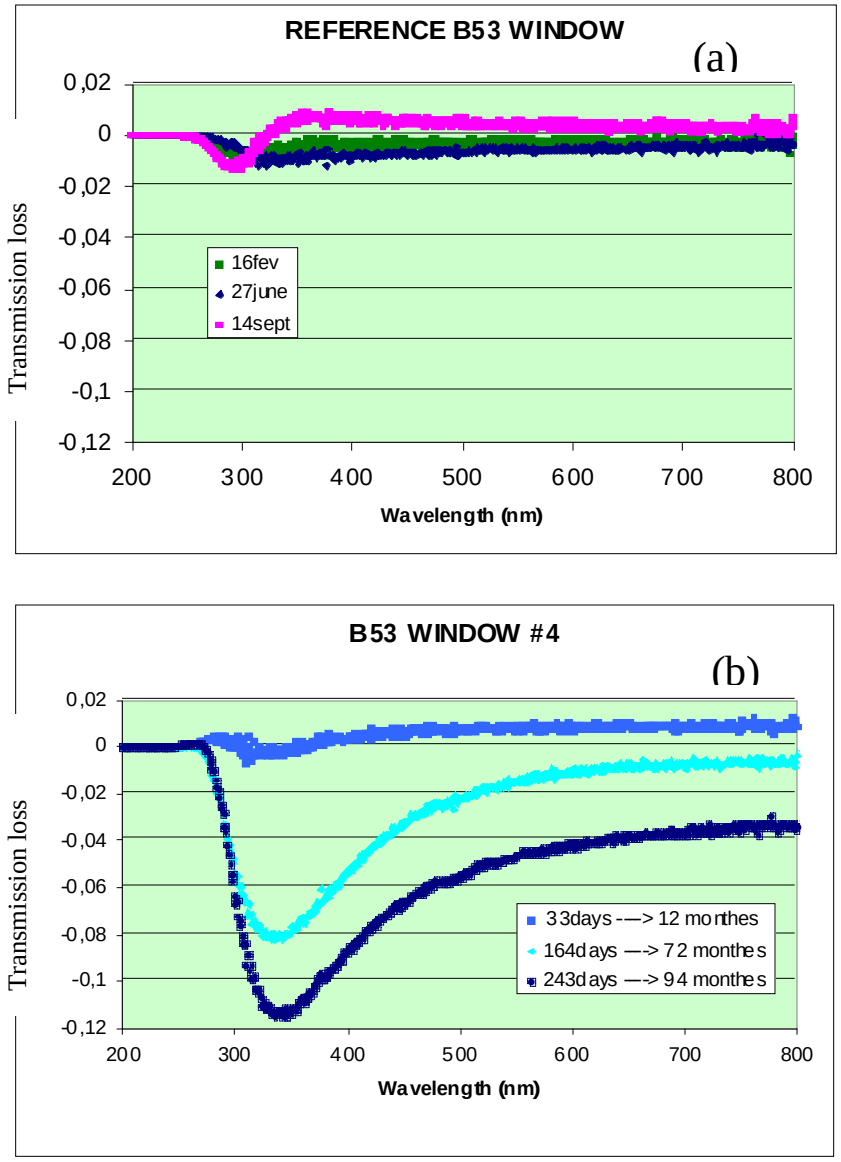

Figure 17. Transmission loss (relative to the initial transmission) for (a) the reference B53 window, and (b) for one coupon immersed in hot water at different periods.

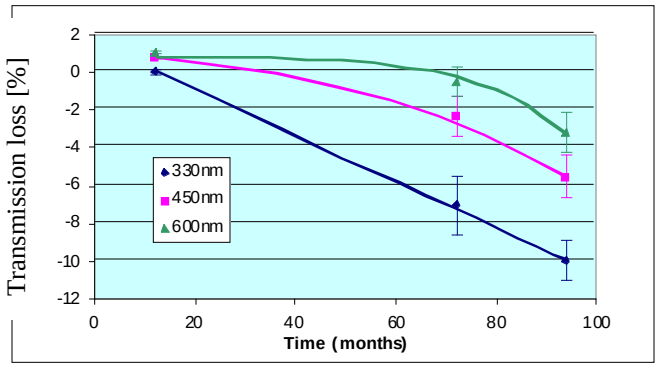

Figure 18. The transmission loss in percentage at different wavelengths.

5.6. Conclusions from Tests at Saclay

The effect of ultra pure water on the PMT glass window has been quantified by studying the corrosion rates in hot water and applying the relevant acceleration factor. We confirm the ETL results that the PMT front window, which is made of B53 glass, will loose less than 1% of its thickness in ten years of operation. Therefore, there is no significant risk of implosion for PMTs with B53C windows. Our measurements, based on scaling from the hot water tests, indicate that the risk of implosion is small in ten years even for the "frosty" PMTs. Saclay plans to make a cross-sectional cuts through the "frosty" PMTs.

We measure a decrease of a few percent in the transmission after ten years equivalent at SOB temperature. However, this measurement was done in air, where the optical coupling is much worse than in water.

We measure a non-negligible loss of detection efficiency, on which we can put an upper limit ranging from 20 to 60% per ten years of operation. The loss of the detection efficiency could be explained by a loss of either the window transmission or the PMT quantum efficiency (in this measurement, the PMT gain variation was calibrated out). The efficiency loss measured in Saclay would represent an addition to the possible PMT gain loss due to the total accumulated anode charge mentioned in Section 4.4. However, one should add that the Saclay test did not measure a possible loss of the quantum efficiency in warm water.

5. Tests Performed at SLAC

5.1. Overview

This section describes tests performed at SLAC. They include periodic visual observations of the status of PMT glass faces viewed through the window ports of the SOB, taking pictures of PMTs removed from the SOB vessel, X-ray and ESCA surface analysis of PMT glass, detailed SOB water trace element analysis, and a long-term test of front PMT glass coupons. We used the water analysis to check if the sodium and boron levels are consistent with the known corrosion of the PMT glass. We also include other measurements, which SLAC performs regularly, such as the water transmission at 266, 325, and 442nm, water pH factor, water resistivity, and SOB water temperature. The results of this work are described in the following sections.

5.2. Visual Observation of PMT Glass Through the Ports in the SOB Vessel

We can only see gross effects when viewing a corroded glass through the SOB port, while the vessel is full of water. This is due to the good optical coupling of water to glass surface, even if it is corroded. We have performed periodic checks over the past ten months. There was no observable degradation detected.

5.3. Electron Microscope Pictures of PMTs Removed from the SOB Vessel

Figure 19(a) shows an electron microscope picture of a "frosty" PMT, designated as #4 in Fig. 1. The surface is full of small fractures, which seem to be peeling off the surface underneath. Some of the fracturing occurs when the PMT is subjected to vacuum forces in the electron microscope. For example, Figure 19(b)

shows an example of such fracturing on a “milky” PMT, designated as #3 in Fig. 1. It is believed that it occurred in the vacuum. The thickness of the fracture shown on Fig. 19(b) is 1-2 microns. Another example is shown on Fig. 20, which shows PMT #10, which was neither “milky” nor “frosty” and was removed from the SOB by mistake. It also developed crazing when subject to forces in vacuum. This indicates that any PMT, which was subjected to water for more than ~6 months, must not be stressed excessively in any way. This result led us to a major decision not to open the SOB unless it is absolutely necessary.

(a) (b)

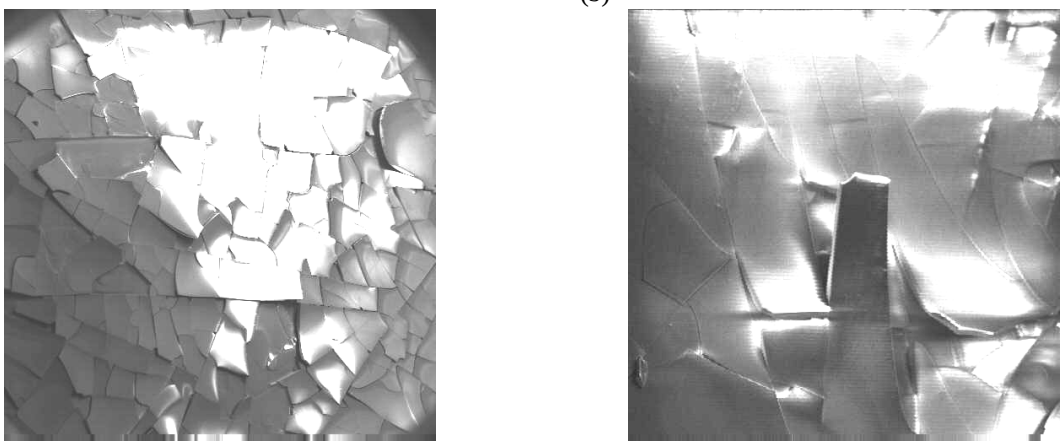

Figure 19. (a)“Frosty” PMT, designated as #4 in Fig. 1, developed crazing already in the SOB. (b) This picture indicates that a “milky” PMT, designated as #3 in Fig. 1, can develop crazing when placed in the electron microscope vacuum. The thickness of the fracture is 1-2 microns.

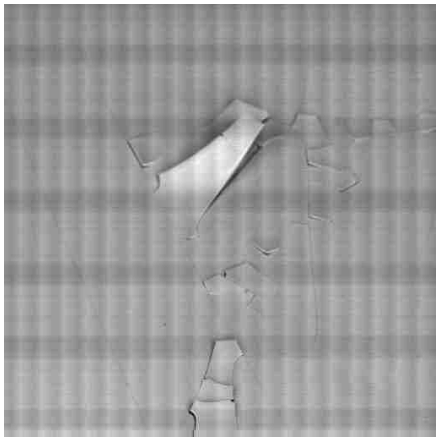

Figure 20. PMT #10, designated as “clear” and nearly perfect, was removed from SOB by mistake (it was neither “milky” nor “frosty”). It developed crazing when subjected to vacuum forces in the electron microscope. This led us to conclude that we should minimize any stresses, such as unnecessary water draining, SOB opening, etc.

5.4. Surface X-Ray Analysis of PMT Glass

This technique uses an electron beam (~15 keV) and measures a spectrum of the recoiled X-rays. Figure 21 shows a typical X-ray spectrum taken at accelerating voltage of 15 kV. A simulation, shown in Fig. 22, shows the electron beam penetrating 1-2 microns in glass at 15kV, i.e., probing the few microns at the surface. At the same time, the electron beam lateral spread is about 1-2 micron when it stops. Therefore, a sampling volume at this voltage is a cube of the size of a few microns. This is an important result because several conclusions, based on the X-ray analysis and presented in Section 5.4.1, only apply to a small depth.

One can clearly identify major peaks of O, Na, Si, C, and Al in Fig. 21. These peaks will be used in Section 5.4.1 to analyze the sodium depletion in front-glass. It is difficult to see Zn using our electron microscope, because the Zn and Na peaks are close to each other. At 15 kV, Zn has two X-ray lines, a dominant one is at 1.010 keV and a weaker one is located at 8.638 keV (less than 10% intensity). Na has only one line at 1.041 keV. This was verified by using calibration targets containing either ZnO or NaF_2. In all our PMT front glass analysis of "milky" or "frosty" tubes we did not have any hints of the 8.638 keV line, which would indicate a presence of Zn. One should add that there was no peak corresponding to Rhenium, which would indicate that the light catcher plating is coming off.

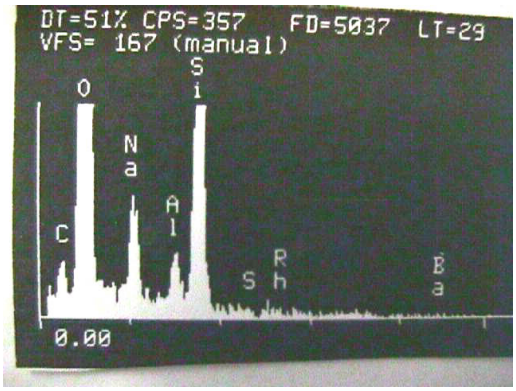

Figure 21. Elemental composition of a reference glass as measured in the electron microscope operating a 15 kV. electron beam strikes a PMT front glass surface and recoil X-ray spectrum is measured. One can clearly recognize major components of glass: O, Si, Na, Al and C.

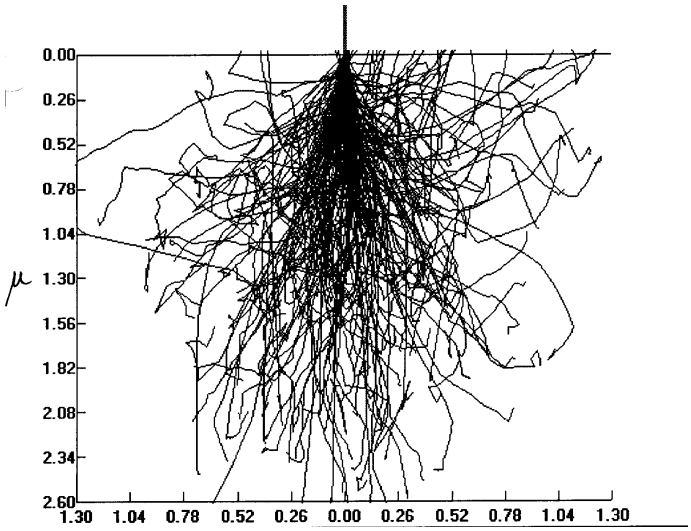

Figure 22. Monte Carlo simulation of motion of 15 KeV electron in SiO_2 using the commercial program "Flight Simulator" (courtesy of B. Kirby).

5.4.1. Sodium Depletion of PMT Front-Glass Taken out of the SOB Vessel

Figure 23 shows a sequence of points along the PMT envelope where the primary electron beam strikes. For each point we have taken, the X-ray spectrum is similar to that shown in Figure 21. As one follows the sequence of points, shown in Fig. 23, one slightly changes the solid angle for the X-ray detection. This was calibrated out by using a Na/Si ratio, assuming that the Si component is changing only slightly.

Figure 24 shows the result as a ratio of X-ray peak areas of Na and Si for a "milky" PMT #6 (S/N 050038) (taken out of SOB during the October 1999 shutdown), normalized by the same peak area ratio for a brand new PMT (this PMT was not immersed in the water at all). One can see that points 5-14, which are located on the

front PMT glass surface, clearly shows sodium depletion relatively to points 1, 2, 3, 4, and 15, which are located on the glass side of the PMT, as shown on Fig. 23. The side glass has a different composition than the front glass (see Section 6).

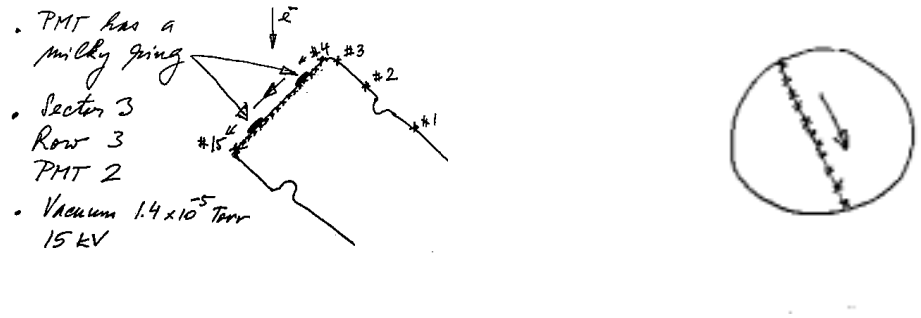

Figure 23. A sequence of points along the PMT glass, where the electron beam hit and the X-ray scan was taken to check for sodium depletion.

Another analysis performed under a flake of PMT #4, similar to that shown in Fig. 19(b), indicates no sodium depletion. However, on top of the flake sodium depletion is detected. A typical flake, only a few microns thick is indicative that sodium depletion extends to depths of only a few microns (see Fig. 19b). This result is consistent with the penetration depth of 15 keV electron beam in SiO_2, as simulated in Fig. 22 by a computer program. The measurement of sodium depletion under the flake was possible since the PMT was placed into the electron microscope at an angle. The result is also consistent with the rate of removal, based on the water purity tests described in Section 5.6.

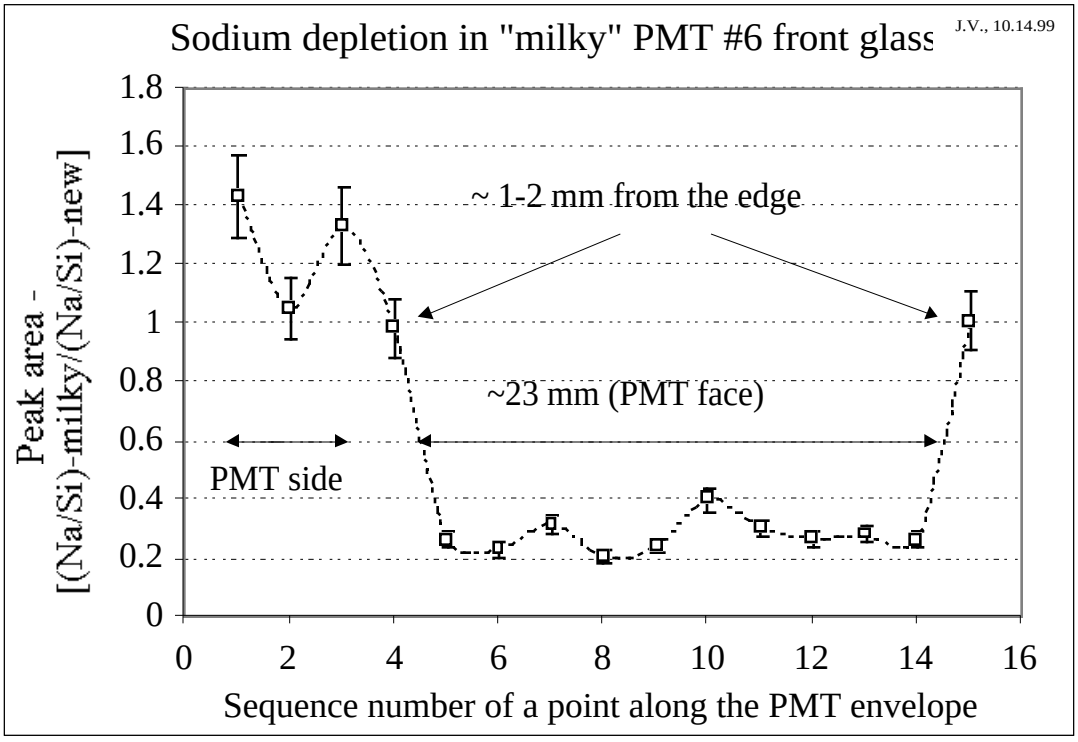

Figure 24. Sodium depletion in the front glass of PMT #6 (S/N 254776) judged as having a "milky" surface, and removed from the SOB during October 1999 shutdown. A sequence of numbers follow the glass envelope as described on Fig 23. The Si X-ray peak was used as the normalization of the X-ray detector response due to the changing solid angle during the surface sweep.

Figure 25 shows similar sodium depletion, although to a lesser extent. The front PMT glass surface (#1 or S/N 050038) used in early verification tests at Orsay, is designed to show that there is no water induced PMT glass corrosion. Indeed, one can confirm that there was no visual effect. However, more precise X-ray tests show that corrosion is present in terms of sodium depletion on the front of the PMT glass.

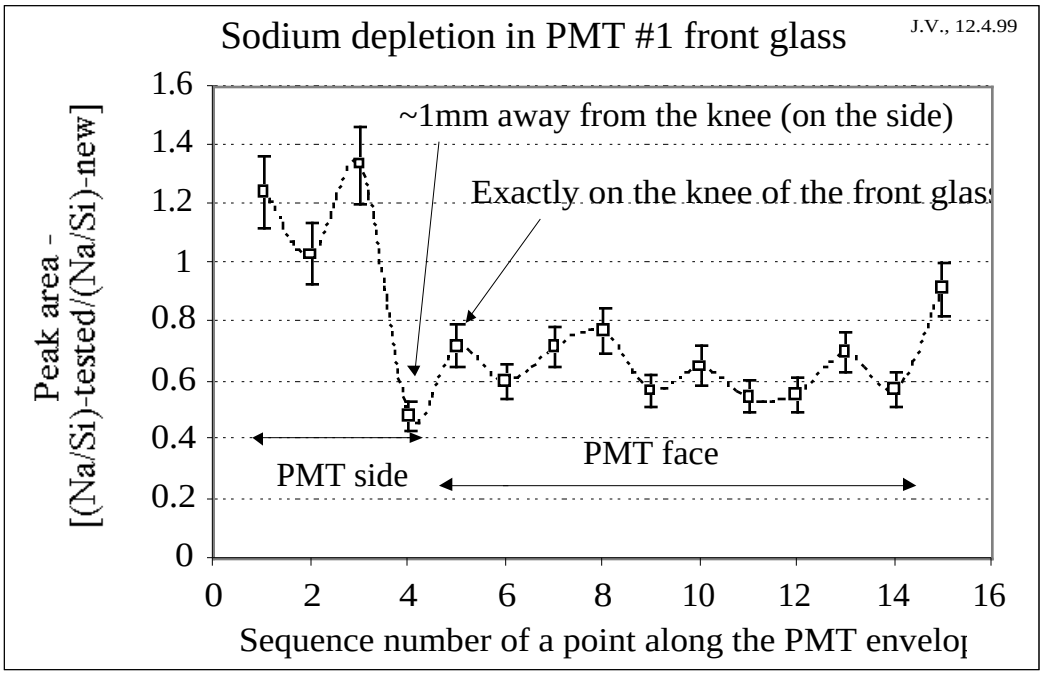

Figure 25. Sodium depletion in the front-glass of PMT #1 (S/N 050038) used in early tests at Orsay to verify the absence of glass corrosion by water. A sequence of numbers follows the glass envelope as described on Fig. 23. The Si X-ray peak was used as a normalization of the X-ray detector response due to solid angle changes during the surface sweep.

5.5. ESCA Analysis of the Front-Glass PMT Taken out of the SOB Vessel

This technique uses a very soft X-ray beam (1.487 keV) and measures a spectrum of the recoiled electrons. The soft X-ray beam probes only ~50Å of the glass volume, which is a major difference from the electron beam-based X-ray analysis (see Section 5.4). The X-ray analysis probes 2-3 microns of glass volume at 15kV. Another technical difference is that the ESCA spectrometer vacuum chamber is much smaller, and one needs to cut front PMT glass to do the front glass analysis.

The analysis was done on several tubes: (a) “milky” PMT #6 (S/N 254776), (b) “milky” PMT #8 (S/N 255140), and (c) “frosty” PMT #4 (S/N 268893). The last two were broken up to allow a cross-sectional analysis of the front glass. Figure 26 clearly shows that Zn is present in the front glass of the “milky” PMT #6, although we do not see any Na, because it is already depleted from the front surface. Figures 27 and 28 show that both elements, Zn and Na, are present in the “milky” PMT #8. This means that zinc is present not only on the outside surface (Fig. 27), but also in the volume (Fig. 28). This is evaluated as consistency proof that the “milky” appearance corresponds to B53-type glass, which confirms the ETL results. On the other hand, Fig. 29 shows that we clearly do not see Zn in the “frosty” PMT #4, although we do see Na. This agrees with the ETL observation that only the “frosty” PMTs do not have Zn element in the front glass. The milky PMTs, as well as all clear PMTs, do have Zn in the form of ZnO. Our tests were done on PMTs taken out of the SOB vessel in IR-2 after being immersed in water for ~8 months at temperatures between 26-28^{o}C.

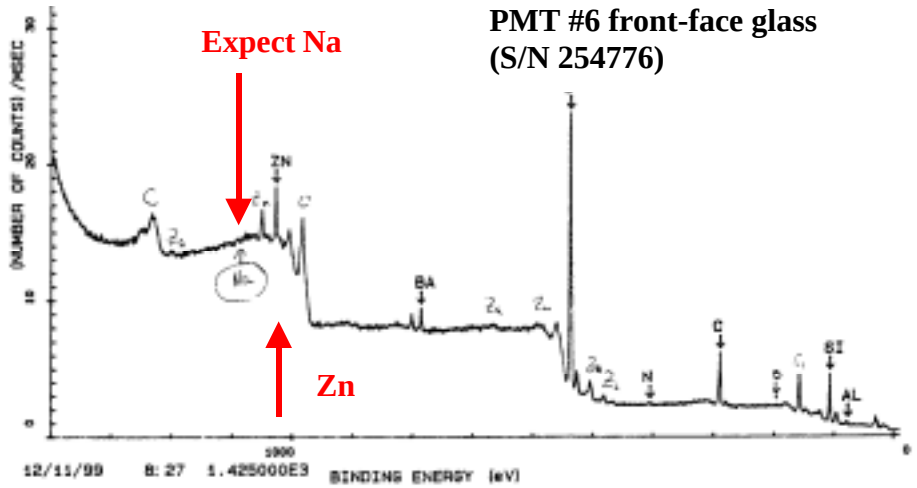

Figure 26. ESCA analysis of front-face glass of PMT #6 (S/N 254776), which was judged as "milky," and removed from the SOB vessel during the October 1999 shutdown. Zn is clearly detected, which is taken as a proof that the glass was indeed B53 glass. This result is consistent with the "milky" appearance; however, there is no sign of Na.

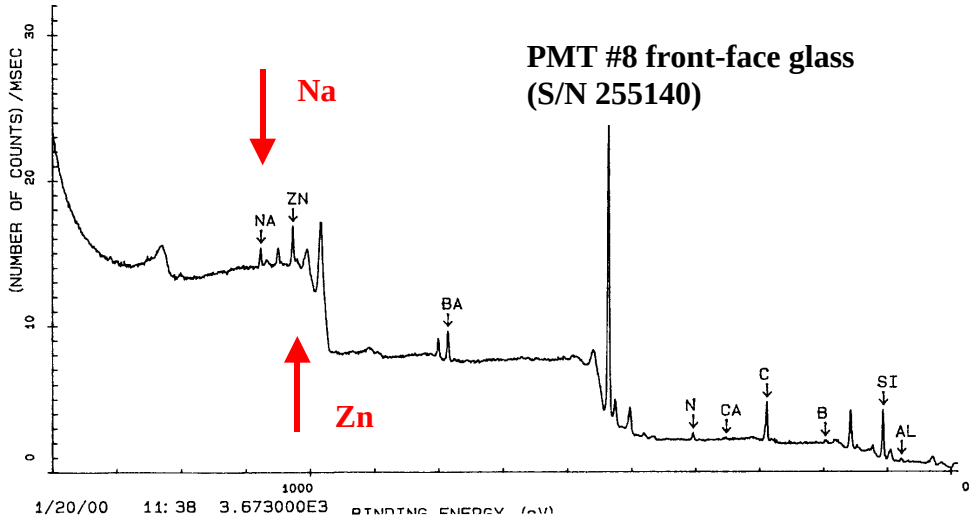

Figure 27. ESCA analysis of front-face glass of PMT #8 (S/N 255140), which was judged as "milky" and removed from the SOB vessel during the October 1999 shutdown. Both elements, Zn and Na, are clearly detected.

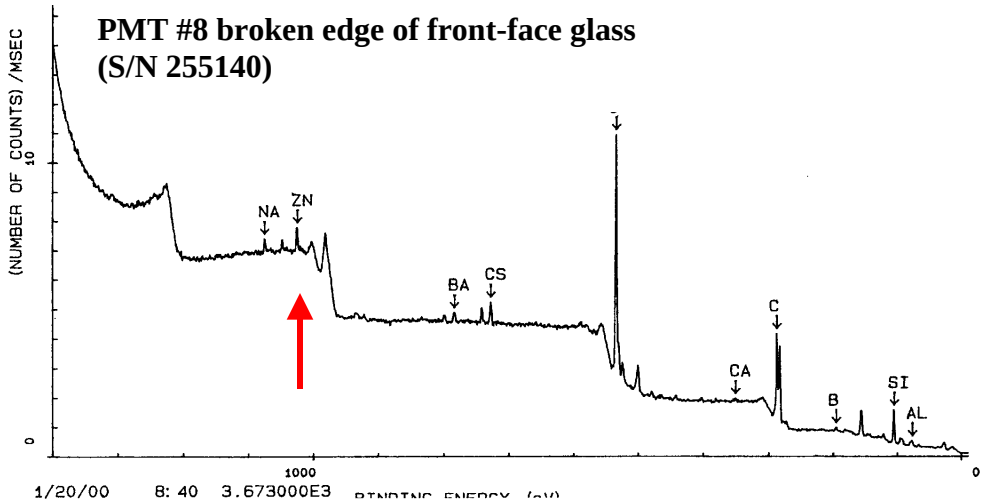

Figure 28. ESCA side analysis of the broken edge of the front face glass of PMT #8 (S/N 255140), which was judged as "milky," and removed from the SOB vessel during the October 1999 shutdown. Both elements, Zn and Na, are clearly detected in the volume of the front glass. This means that the glass is B53-type glass, which meets the required glass type.

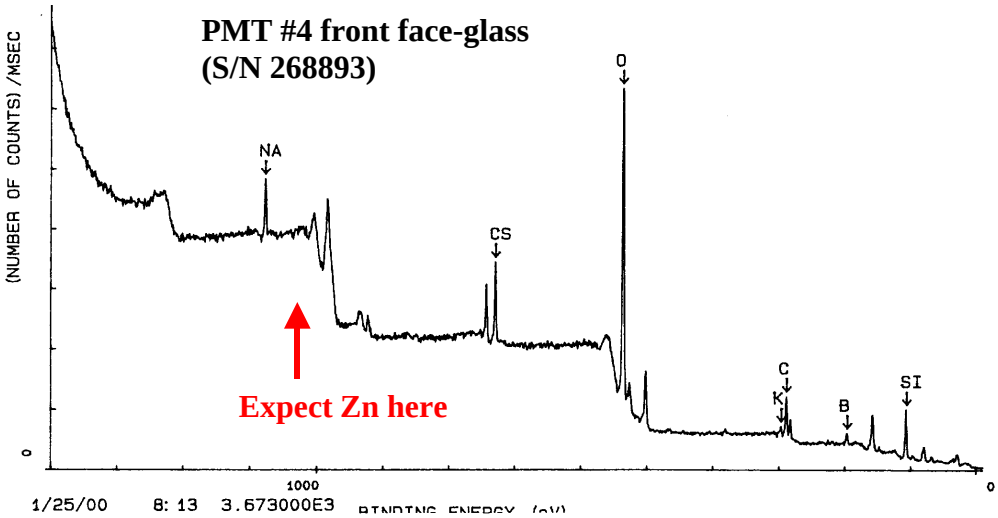

Figure 29. ESCA analysis of front face glass of PMT #4 (S/N 268893), which was judged as "frosty," and removed from SOB vessel during the October 1999 shutdown. Clearly, we see no sign of Zn. This confirms the ETL observation that "frosty" PMTs do not have Zn, because they are made with the wrong X-type glass.

5.6. Water Analysis and Its Relationship to Glass Corrosion

If elements of the PMT glass are leaching into water, we should be able to detect them in precision water analysis. Today, a modern water analysis is capable of determining impurities at a level of 0.001-0.010 ppb. As we will see, with this level of precision it is possible to verify that sodium from the front PMT glass is indeed leaching into the water, i.e., verify conclusions from the X-ray analysis described in Section 5.2.1. By doing periodic water analysis, it is then possible to determine if the leaching is constant, improving, or deteriorating.

Table 12 shows results of trace metal analysis, detection limits, and bacteria count in the supply and return of the SOB water in IR-2, which were performed ~8 months apart. Our experience with the detection limits indicate that the quoted number, especially frequently found elements such as sodium, could exceed its nominal quoted value by a factor of 2-3 on any given measurement trial. Variations can be caused by a sampling technique, presence of people, sample bottle contamination, etc. The water sampling and the analysis were done by the Balazs Co.[5] We were especially interested in elements, which are present in the PMT glass, such as sodium, boron, and silicone. The difference between supply and return water samplings in November 1999 indicate 0.28 ± 0.14 ppb of Na, 0.3 ± 0.1 ppb of B, and 0.3 ± 1 ppb of Si, where the error margin is given as twice the detection limit shown in Table 1. In August 2000, these differences changed to 0.44 ± 0.14 ppb of Na, 0.4 ± 0.1 ppb of B, and 0.0 ± 1 ppb of Si. For all practical purposes, we can neglect Si as a significant result given its very large errors.

According to ETL, the B53 glass turns "milky" with loss of sodium, while the "frosty" window has loses of sodium and boron (see Section 2.3.4.). If we assume this, we may determine two different scaling rates. One rate for the sodium leaching from all PMTs in the DIRC, and another rate for the boron leaching from only "frosty" PMTs, which are made of X-glass. There are only 50 such PMTs in the DIRC system.

From Table 12, we conclude that the leaching rates of Na and B are constant during the past eight months within errors. We can also use the results from Table 12 to estimate the depth of the PMT front glass affected by Na and B leaching. Table 13 shows results of this calculation. The analysis of the Na leaching indicates that we are removing this element from the front PMT glass at a rate of 3-4 μm/PMT/year. This is consistent with the electron microscope surface analysis of the "milky" PMTs that were taken out of the SOB in October 1999. At this rate of removal, and assuming that it will continue to be constant in the future, the PMTs with B53 glass should last ~10 years from the point of view of implosion danger. The analysis of the B leaching, assuming that boron only comes out of "milky" PMTs, indicates that we are removing this element from the front PMT glass at a rate of ~800μm/PMT/year. This is much larger than the ETL measurement (see Fig. 2). At this rate of removal, the "frosty" PMTs would have already imploded. Clearly, the boron model's assumption that only "frosty" PMTs leach may not be entirely correct. It would be more consistent with our observations to assume that boron leaches similarly to sodium, i.e., from all PMTs with B53 glass (see Table 13 for details).

Table 14 shows SLAC's measurements of the water pH factor, resistivity, transmission, and temperature during water samplings shown in Tables 12 and 13. Clearly, these variables are not sensitive to the level of impurities seen in the water analysis.

It is useful to compare the DIRC water quality with other experiments, for example, such as Super Kamiokande (SK) or K2K, which have been successfully running already for the past 2-4 years with a very large number of PMTs in ultra-pure water. Table 15 shows the impurity level in water of SK and K2K experiments, compared with the DIRC water purity shown in Table 12. If one takes, for example, sodium in their water, it is comparable with our level; however, in their case, there is no evidence suggesting that they are leaching it from PMTs (supply is higher than return). Perhaps, one could argue that the K2K experiment could be leaching calcium and aluminum, elements present in their PMTs. However, there is no visual evidence of PMT window glass corrosion in the two experiments [15]. Table 16 shows their typical operating parameters, such as water flow, pH factor, resistivity, and water temperature. Judging from a similarity in water resistance between DIRC, SK, and K2K, it appears that the water quality is rather similar.

Worthy of note is that the SK and K2K experiments are running considerably cooler than we do, which certainly helps to keep low bacteria levels, and also helps to reduce chemical reactivity in water. A low bacteria level is important from the point of view of corroded surface. Bacteria "likes" to reside in various cavities, and we certainly would not want them to be "residing" in PMT window glass, which would reduce photon transmission. Therefore, it we were pleased to see low-bacteria count in the SOB water return during our last measurement – see Table 12.

[5] Balazs Analytical Laboratory, 252 Humboldt Court, Sunnyvale, CA 94089-1315.

Table 12: Trace metal water analysis of DIRC water performed by the Balazs Analytical Laboratory.

Parameter	Test type	DL(det.lim)	Units	SUPPLY	RETURN	SUPPLY	RETURN
				11/30/99	11/30/99	8/21/00	8/21/00
Bacteria/100ml	Bacteria-ASTM	1	cfu	*,*,*	>500,>500	*,*,11	*,16,66
Aluminum (Al)	Trace Metals by ICP-MS	0.003	ppb (ug/l)	*	*	0.004	*
Antimony (Sb)	Trace Metals by ICP-MS	0.002	ppb (ug/l)	*	*	*	*
Arsenic (As)	Trace Metals by ICP-MS	0.005	ppb (ug/l)	*	*	*	*
Barium (Ba)	Trace Metals by ICP-MS	0.001	ppb (ug/l)	*	*	0.005	0.002
Beryllium (Be)	Trace Metals by ICP-MS	0.003	ppb (ug/l)	*	*	*	*
Bismuth (Bi)	Trace Metals by ICP-MS	0.001	ppb (ug/l)	*	*	*	*
Boron (B)	Trace Metals by ICP-MS	0.05	ppb (ug/l)	2.9	3.2	1.8	2.2
Cadmium (Cd)	Trace Metals by ICP-MS	0.003	ppb (ug/l)	*	*	*	*
Calcium (ca)	Trace Metals by ICP-MS	0.2	ppb (ug/l)	*	*	*	*
Cerium (Ce)	Trace Metals by ICP-MS	0.001	ppb (ug/l)	*	*	*	*
Cesium (Cs)	Trace Metals by ICP-MS	0.001	ppb (ug/l)	*	*	*	*
Chromium (Cr)	Trace Metals by ICP-MS	0.004	ppb (ug/l)	*	*	*	*
Cobalt (Co)	Trace Metals by ICP-MS	0.001	ppb (ug/l)	*	*	*	*
Copper (Cu)	Trace Metals by ICP-MS	0.003	ppb (ug/l)	*	*	*	*
Dysprosium (Dy)	Trace Metals by ICP-MS	0.001	ppb (ug/l)	*	*	*	*
Erbium (Er)	Trace Metals by ICP-MS	0.001	ppb (ug/l)	*	*	*	*
Europium (Eu)	Trace Metals by ICP-MS	0.001	ppb (ug/l)	*	*	*	*
Gadolinium (Gd)	Trace Metals by ICP-MS	0.001	ppb (ug/l)	*	*	*	*
Gallium (Ga)	Trace Metals by ICP-MS	0.002	ppb (ug/l)	*	*	*	*
Germanium (Ge)	Trace Metals by ICP-MS	0.003	ppb (ug/l)	*	*	*	*
Gold (Au)	Trace Metals by ICP-MS	0.006	ppb (ug/l)	*	*	*	*
Hafnium (Hf)	Trace Metals by ICP-MS	0.001	ppb (ug/l)	*	*	*	*
Holmium (Ho)	Trace Metals by ICP-MS	0.001	ppb (ug/l)	*	*	*	*
Indium (In)	Trace Metals by ICP-MS	0.001	ppb (ug/l)	*	*	*	*
Iridium (Ir)	Trace Metals by ICP-MS	0.002	ppb (ug/l)	*	*	*	*
Iron (Fe)	Trace Metals by ICP-MS	0.02	ppb (ug/l)	*	*	*	*
Lanthanum (La)	Trace Metals by ICP-MS	0.001	ppb (ug/l)	*	*	*	*
Lead (Pb)	Trace Metals by ICP-MS	0.003	ppb (ug/l)	*	*	*	*
Lithium (Li)	Trace Metals by ICP-MS	0.002	ppb (ug/l)	*	*	*	*
Lutetium (Lu)	Trace Metals by ICP-MS	0.001	ppb (ug/l)	*	*	*	*
Magnesium (Mg)	Trace Metals by ICP-MS	0.002	ppb (ug/l)	*	*	*	*
Manganese (Mn)	Trace Metals by ICP-MS	0.002	ppb (ug/l)	*	*	0.002	*
Mercury (Hg)	Trace Metals by ICP-MS	0.02	ppb (ug/l)	*	*	*	*
Molybdenum (Mo)	Trace Metals by ICP-MS	0.004	ppb (ug/l)	*	*	*	*
Neodymium (Nd)	Trace Metals by ICP-MS	0.001	ppb (ug/l)	*	*	*	*
Nickel (Ni)	Trace Metals by ICP-MS	0.004	ppb (ug/l)	*	*	*	*
Niobium (Nb)	Trace Metals by ICP-MS	0.001	ppb (ug/l)	*	*	*	*
Osmium (Os)	Trace Metals by ICP-MS	0.002	ppb (ug/l)	*	*	*	*
Palladium (Pd)	Trace Metals by ICP-MS	0.002	ppb (ug/l)	*	*	*	*
Platinum (Pt)	Trace Metals by ICP-MS	0.009	ppb (ug/l)	*	*	*	*
Potassium (K)	Trace Metals by ICP-MS	0.1	ppb (ug/l)	*	*	*	*
Praseodymium (Pr)	Trace Metals by ICP-MS	0.001	ppb (ug/l)	*	*	*	*
Rhenium (Re)	Trace Metals by ICP-MS	0.003	ppb (ug/l)	*	*	*	*
Rhodium (Rh)	Trace Metals by ICP-MS	0.001	ppb (ug/l)	*	*	*	*
Rubidium (Rb)	Trace Metals by ICP-MS	0.001	ppb (ug/l)	*	*	*	*
Ruthenium (Ru)	Trace Metals by ICP-MS	0.002	ppb (ug/l)	*	*	*	*
Samarium (Sm)	Trace Metals by ICP-MS	0.002	ppb (ug/l)	*	*	*	*
Scandium (Sc)	Trace Metals by ICP-MS	0.01	ppb (ug/l)	*	*	*	*
Selenium (Se)	Trace Metals by ICP-MS	0.02	ppb (ug/l)	*	*	*	*
Silicon (Si)	Trace Metals by ICP-MS	0.5	ppb (ug/l)	2.8	3.1	*	*
Silver (Ag)	Trace Metals by ICP-MS	0.001	ppb (ug/l)	*	*	*	*
Sodium (Na)	Trace Metals by ICP-MS	0.007	ppb (ug/l)	0.014	0.29	0.14	0.44
Strontium (Sr)	Trace Metals by ICP-MS	0.001	ppb (ug/l)	*	*	*	*
Tantalum (Ta)	Trace Metals by ICP-MS	0.004	ppb (ug/l)	*	*	*	*
Tellurium (Te)	Trace Metals by ICP-MS	0.004	ppb (ug/l)	*	*	*	*
Terbium (Tb)	Trace Metals by ICP-MS	0.001	ppb (ug/l)	*	*	*	*
Thallium (Th)	Trace Metals by ICP-MS	0.006	ppb (ug/l)	*	*	*	*
Thorium (Th)	Trace Metals by ICP-MS	0.003	ppb (ug/l)	*	*	*	*
Thulium (Tm)	Trace Metals by ICP-MS	0.001	ppb (ug/l)	*	*	*	*
Tin (Sn)	Trace Metals by ICP-MS	0.005	ppb (ug/l)	*	*	*	*
Titanium (Ti)	Trace Metals by ICP-MS	0.002	ppb (ug/l)	*	*	*	*
Tungsten (W)	Trace Metals by ICP-MS	0.005	ppb (ug/l)	*	*	*	*
Uranium (U)	Trace Metals by ICP-MS	0.002	ppb (ug/l)	*	*	*	*
Vanadium (V)	Trace Metals by ICP-MS	0.003	ppb (ug/l)	*	*	*	*
Ytterbium (Yb)	Trace Metals by ICP-MS	0.001	ppb (ug/l)	*	*	*	*
Yttrium (Y)	Trace Metals by ICP-MS	0.001	ppb (ug/l)	*	*	*	*
Zinc (Zn)	Trace Metals by ICP-MS	0.005	ppb (ug/l)	*	*	*	*
Zirconium (Zr)	Trace Metals by ICP-MS	0.005	ppb (ug/l)	*	*	*	*

Table 13. Leaching rate of Na and B based on results shown in Table 12.

1) Assume that Na is leaching from windows of all PMTs:

Parameter	Value on 12/13/1999	Unit
Na level (out-in)	0.276	ppb
SOB water volume	6	m^3
Water flow	18	m^3/day
PMT window dia.	2.5	cm
Single PMT area	4.9	cm^2
Total PMT area	5.39	m^2
Leaching rate of Na+	0.004968	g/day
Leaching rate per pmt	4.51636E-07	g/(pmt*day)
Leaching rate of Na2O	6.08727E-07	g/(pmt*day)
Na2O content in glass	0.1338	g/cm^3
Leaching rate	4.54953E-06	cm^3/(pmt*day)
Depth removal	9.28476E-07	cm/(pmt*day)
Depth removal	3.388936496	um/(pmt*yr)

2a) Assume that Boron is leaching from windows of all PMTs:

Parameter	Value on 12/13/1999	Unit
B level (out-in)	0.3	ppb
SOB water volume	6	m^3
Water flow	18	m^3/day
PMT window dia.	2.5	cm
Single PMT area	4.9	cm^2
Total PMT area	5.39	m^2
Leaching rate of B+	0.0054	g/day
Leaching rate per pmt	4.90909E-07	g/(pmt*day)
Leaching rate of B2O3	1.66909E-06	g/(pmt*day)
B2O3 content in glass	0.3345	g/cm^3
Leaching rate	4.98981E-06	cm^3/(pmt*day)
Depth removal	1.01833E-06	cm/(pmt*day)
Depth removal	3.716898092	um/(pmt*yr)

2b) Assume that Boron is leaching from only "frosty" PMTs:

Parameter	Value on 12/13/1999	Unit
B level (out-in)	0.3	ppb
SOB water volume	6	m^3
Water flow	18	m^3/day
PMT window dia.	2.5	cm
Single PMT area	4.9	cm^2
Total PMT area	0.0245	m^2
Leaching rate of B+	0.0054	g/day
Leaching rate per pmt	0.000108	g/(pmt*day)
Leaching rate of B2O3	0.0003672	g/(pmt*day)
B2O3 content in glass	0.3345	g/cm^3
Leaching rate	0.001097758	cm^3/(pmt*day)
Depth removal	0.000224032	cm/(pmt*day)
Depth removal	817.7175803	um/(pmt*yr)

Table 14. Various test results performed at SLAC, which correspond to the timing of the water samples measured by Balazs Analytical Laboratory (this is addendum to Tables 12 & 13).

IR2 WATER QUALITY 1-st TEST RESULTS					
SLAC measurements of water transmission, pH factor, water resistivity and temperature ---->					
Parameter	**Unit**	**Results**		**Results**	
Date		12/13/99		8/21/00	
pH SUPPLY	PH Ffactor	6.7		6.5	
pH RETURN	PH factor	6.3		6.6	
R-water SUPPLY	Mohm.cm	13.4		18.5	
R-water RETURN	Mohm.cm	8.3		9.7	
T-water temp.	deg C	24.3		27.1	
Water flow	One volume change every	8 hours		24 hours	
Trans. (442nm)	%/meter	99.14	+- 0.1	98.09	+- 0.02
Trans. (325nm)	%/meter	98.56	+- 0.7	98.05	+- 1.7
Trans. (266nm)	%/meter	91.23	+- 1.3	91.86	+- 0.8
Comment		Old filters		New filters	
UV lamp		185 nm		260 nm	

Table 15. Water composition in Super Kamiokande (SK) and K2K experiments, which also use pure water [15].

K2K and Super Kamiokande, water sampled by Dr. Mine on May 21, 1999								
Parameter	Reference	K2K supply	K2K return	SK supply	SK return	SK 20 m	SK 37 m	Units
	3/21/99	3/21/99	3/21/99	3/21/99	3/21/99	3/21/99	3/21/99	
Aluminum (Al)	< 0.1	0.2	1.7	< 0.1	< 0.1	< 0.1	< 0.1	ppb (ug/l)
Calcium (ca)	0.23	0.073	2.4	0.11	0.82	0.29	0.29	ppb (ug/l)
Copper (Cu)	< 0.01	< 0.01	< 0.01	< 0.01	< 0.01	< 0.01	< 0.01	ppb (ug/l)
Iron (Fe)	< 0.01	0.04	0.26	< 0.01	0.03	0.03	< 0.01	ppb (ug/l)
Magnesium (Mg)	0.05	0.005	0.24	< 0.005	0.016	0.03	< 0.005	ppb (ug/l)
Sodium (Na)	0.054	0.28	0.13	0.34	0.29	0.3	0.36	ppb (ug/l)

Note: List only elements they have measured.

Table 16. Water parameters for K2K and Super Kamiokande (SK) experiments [15].

Parameter	K2K	S. K.
Date	3/21/99	3/21/99
pH SUPPLY	6	6
pH RETURN	6	6
R-water SUPPLY	16	18
R-water RETURN	9	10
T-water temp.	12	12
Water flow	2-3 day	2 month

5.7. Long-Term Test of PMT Front-Glass Coupons in the SOB Water Return

We have decided to place twelve PMT front-glass window coupons into the SOB vessel water return. The coupons were supplied by ETL as B53 glass, which is known to contain Zn. Neither Saclay nor SLAC obtained the X- glass coupons, and thus, we could not verify its corrosion rate independently of ETL. The coupons were placed into KYNAR holders (a special plastic which is resistant to water corrosion), as shown in Fig. 30. The holders were inserted in a LEXAN container with N_2 atmosphere above water. The container was placed in a thermally insulated housing, and the temperature was controlled at 30°C. This is close to the SOB water temperature, which is 26-28°C. Therefore, no extrapolation is necessary. We report results obtained after ~8 months of the coupons being immersed in water. We have confirmed this by running an ESCA analysis – see Figure 32. One major result of the back scattered X-ray analysis, shown in Fig. 31, is that Na is almost completely depleted from the first few microns of the glass. This is also verified in the ESCA analysis shown in

Fig. 32, which is sensitive up to the first ~50Å. The glass coupons appeared clear, as judged by visual inspection, when removed from the water. However, we have observed crazing when the coupons were placed in vacuum during surface analysis, as shown in Fig. 33. The crazing affected coupons independently, whether they were pumped on or not during the test, and appeared obvious to the naked eye. One could qualify it as "milky" rather than "frosty" surface from the point of view of our earlier discussions. The flakes appear to be very shallow and few microns thick. In other words, a PMT would operate normally, and with water coupling, we would not see any deterioration of efficiency. This result would be consistent with the ETL manufacturer's finding that it is Zn, which prevents "frosting" development in this particular glass material. We still observe Na depletion and the front window turns "milky;" however, these corrosion effects are much smaller, and DIRC would operate well over the next ten years.

(a) (b)

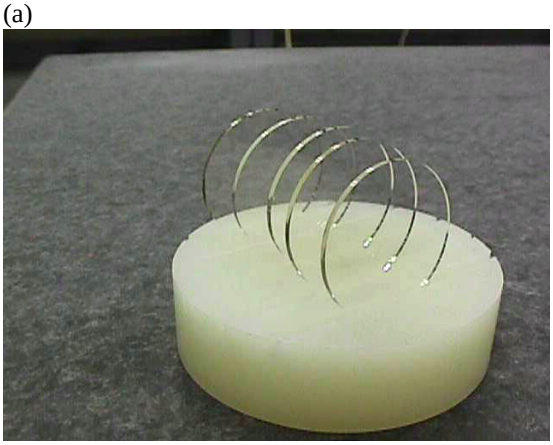

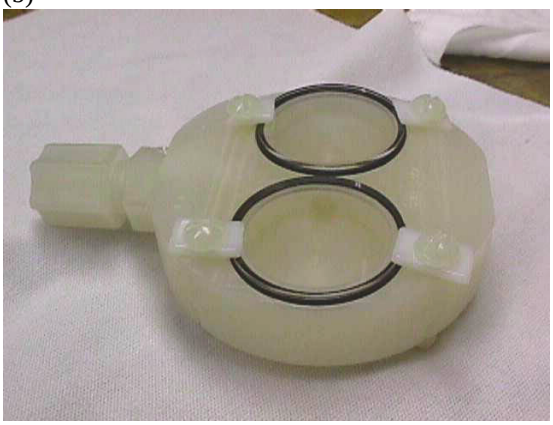

Figure 30. (a) A five-coupon setup placed in the SOB water return. (b) A two-coupon setup, which was pumped on.

(a)

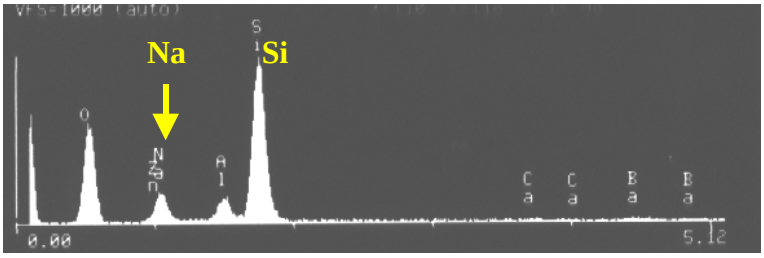

(b)

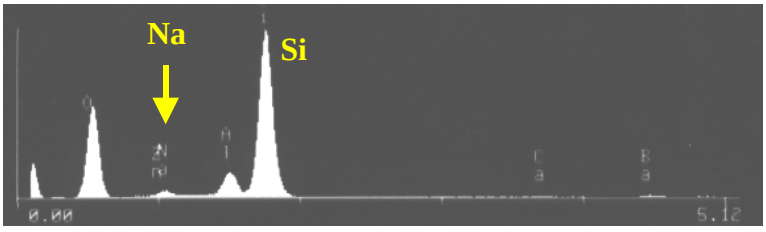

Figure 31. (a) X-ray analysis of the PMT front glass coupon A1, before the water test was started. The Na element is clearly detected. (b) The same coupon after eight months in the SOB water return. From the relative ratio of the Na/Si peak areas, it is clear that the Na line is depleted.

(a)

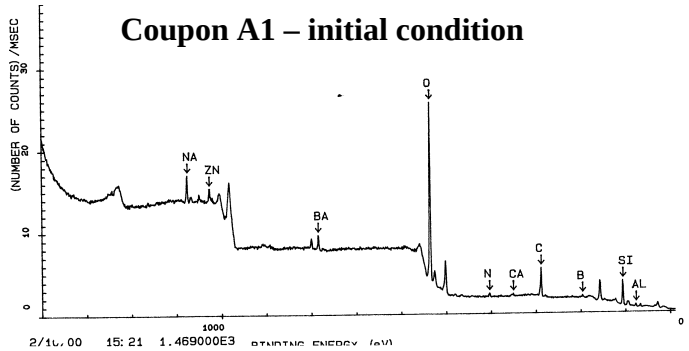

(b)

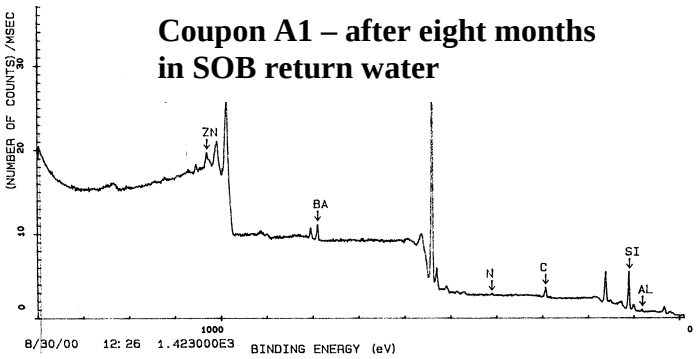

Figure 32. (a) ESCA analysis of the PMT front glass coupon A1, prior to the water test. Both elements, Zn and Na, are clearly detected. This proves that this particular glass has traces of Zn present. (b) The same coupon after eight months in the SOB water return. The Na line is completely missing. The Zn line is still present.

(a) (b)

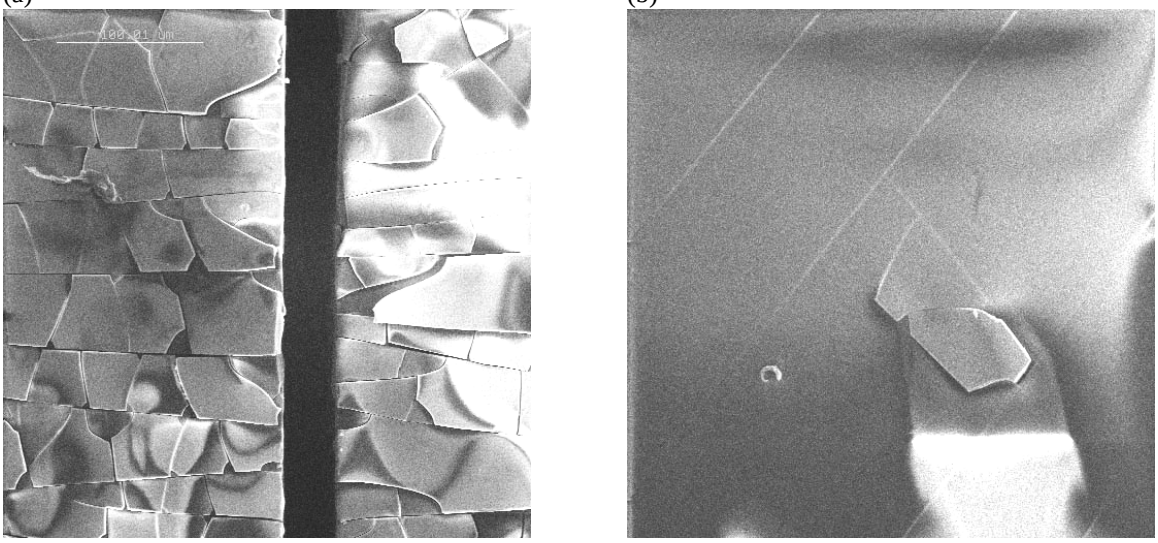

Figure 33. (a) Electron microscope picture of the PMT front glass coupon near the edges of C3 (left) and C5 (right) coupons. C5 coupon was subject to vacuum, C3 was not. They seem to be affected similarly. This type of surface gives a "milky" appearance as discussed elsewhere. (b) A similar picture of the middle C3 coupon, although the corrosion level is generally lower. The "milky" appearance is spotty in the middle of the coupon.

5.8. Conclusion of Tests at SLAC

The SLAC analysis, by using the electronic microscope has determined that sodium depletion affects only the front window glass for both "milky" and "frosty" PMTs. The PMT side glass is not affected.

Similarly, it was determined that using ESCA analysis, that the "frosty" PMTs, do not contain Zn, thus confirming the ETL result indicating that the PMT material made out of X-glass, was added into production in error.

A long-term test of the B53 glass coupons, placed in SOB return water at 30°C, which is close to our operating temperature of 26-28°C in IR-2 (and therefore no scaling is required), shows corrosion levels to be consistent with that of the "milky" PMTs. The sodium is also depleted from the first few microns of surface. Such corrosion, although clearly visible if the glass is not coupled to water, will not represent a disaster for the DIRC from the point of view of possible PMT implosion.

Any time a "milky" PMT was subject to vacuum with the electron microscope, it developed additional crazing. This is a warning that the front PMT glass is very fragile, because of its depleted sodium. Therefore, the PMTs in the SOB must not be subjected to mechanical forces, which includes water draining or door openings.

A trace analysis of the water shows that the amount of sodium present in water is consistent with the sodium leaching from the front PMT glass, and represents a rate of removal of about 3-4 μm/PMT/year. This is consistent with the visual corrosion observed with the electron microscope on the "milky" PMTs.

The water analysis in the DIRC indicates a steady reduction of bacteria levels, which is a necessary condition to guarantee good transparency given the degree of glass corrosion.

The water analysis also indicates that the DIRC does not have excessively pure water compared to other experiments such as K2K or Super Kamiokande.

6. Discussion

The purpose of this section is to point out that the "Zn hypothesis" may not be the "all explaining" recipe, and the answer may lie in the detailed understanding of particular "glass" chemistry. For example, Table 17 shows that in the Pyrex type of glass, as used in Super Kamiokande, there is no Zn at all, and there is no corrosion of the PMT glass window [15]. Apparently, Zn is necessary in some Borosilicate glass formulations. Both ETL and us certainly did observe a very large corrosion level of the X-glass window, which was added to the DIRC PMT production in error (see Sections 1 and 2). If the correct B53 glass is used for the windows, the corrosion is much smaller (only a sodium depletion causing "milky" surfaces). However, we did not see any Na leaching or corrosion on the sides of the glass body of the DIRC PMTs [16], which is also a Borosilicate glass, and has no Zn nominally – see Table 17. Of course, the side glass comes as a tube and goes through a completely different process. Another example is the experience of Philips Photonics with the so called ZK(N)7 glass, which contained a very large amount of Zn (see Table 17), with extremely large rates of corrosion observed in humid air [17]. Therefore, it appears that glass corrosion is dependent on a very delicate balance of various glass ingredients, and Zn may play a significant protection role only if present at the correct quantity. In the case of the DIRC PMTs, the front window glass requires a few percent of Zn in order to limit the corrosion rate, based on the empirical observations which have been presented in this paper.

Based on our experience, we would always recommend that one performs as exhaustive a corrosion test as possible for particular choices of glass formulation.

Table 17. Comparison of PMT glass composition in various experiments or tests by the PMT manufacturers.

Company	Experiment	Glass name	PMT portion	SiO2	Al2O3	B2O3	Li2O	Na2O	K2O	BaO	CaO	As2O3	Sb2O3	ZnO
Hamamatsu	Super Kamiokande	Pyrex	face	80	2.1	14.1	0.1	3.7	0.12	-	-	-	-	-
Hamamatsu	Internal R&D test			-	-	-	-	5.5	-	-	-	-	-	-
Hamamatsu	Internal R&D test			67.5	3	19	0	0.4	9	-	-	-	-	-
Hamamatsu	Internal R&D test			65	0	14	0	0.1	0.06	-	-	-	-	-
Philips Photonics	A special PMT	ZK(N)7	face	60.8	5.6	14	-	7.4	0.003	-	-	0.1	0	11.2
Electron Tube Ltd.	DIRC detector	Borosilicate (B53)	face	65	6	15	-	6	-	3	1	-	-	4
Electron Tube Ltd.	DIRC detector	Borosilicate	side body	71	7	11	-	6	1	2	1	-	-	-
Electron Tube Ltd.	DIRC detector	Borosilicate	pin area	73	5	13	-	8	0.1	-	-	-	-	1
Electron Tube Ltd.	Internal PMT	X glass	window	69.6	4.2	17.2	-	8.7	-	0	0	-	-	0

7. Overall Conclusion

We believe that the DIRC detector has about 50 "frosty" PMTs out of 11,000, where glass will be corroded to such an extent that over a 10-year period there may be a danger of implosion or vacuum loss. The ETL Co. explains that during the production a wrong type of glass was included, namely the so called X-glass, instead of B53 glass. The X-glass does not contain Zn, which according to ETL makes it weaker in terms of rapid leaching of sodium and boron resulting in "frosty" PMTs. In this paper we have provided independent experimental evidence supporting this hypothesis. The rest of the DIRC PMTs used B53 glass, which contains Zn, and this in turn limits the sodium and boron depletion to acceptable levels. There is still glass corrosion up to 30-50 μm of depth after ~10 years of operation, which is believed to be acceptable from the point of view of the danger of implosion.

DIRC's data seems to indicate a non-negligible loss of detection efficiency at a level of 2-3% per year, both in Bahbha and di-muon events. Based on the Saclay test results, this loss could be explained by either window transmission or PMT quantum efficiency loss; however, the PMT gain loss cannot be excluded. A simple estimate of the total PMT accumulated anode charge would favor the PMT gain loss explanation as a dominant factor. Of course, the small PMT gain change can be easily corrected by a corresponding change in voltage. More studies are needed to understand this in more detail.

Acknowledgment

We would like to thanks R. Aleksan, V. Lepeltier, and G. Vasseur for their very valuable help in efforts to understand the PMT glass corrosion problem. We also thank B. Kirby and his group at SLAC, for running the electron microscope and ESCA analysis spectrometer and for providing many useful suggestions for the SLAC-based analysis. We thank A. Hoecker for his help in sorting out tube glass corrosion appearances during the October 1999 shutdown, and B. Ratcliff for suggesting using the water analysis results to check the consistency of the PMT corrosion rates. We also thank R. Reif for his help to set up the long-term glass coupon test at SLAC.

References:

1. A. Hoecker, *http://www.slac.stanford.edu:/~hoecker/IR2/frostyPMT.html*, October 1999.
2. J. Va'vra, BaBar *Hypernews note #595*, October 5, 1999.
3. Electron Tubes Limited, *Water immersion tests,* July 2000.
4. P. Bourgeois et al., BaBar *Hypernews note #993*, September 28, 2000.
5. J. Va'vra, *BaBar Hypernews note #764*, January 29, 2000.
6. The Saclay group, *PMT specifications and EMI 9125*, BaBar DIRC note 32, March 1996.
7. Ph.Bourgeois, M.Karolak and G.Vasseur, *Performance of the photomultiplier tubes used in the DIRC of BaBar: effect of a magnetic field and of helium*, Nucl.Inst.Meth. A442 (2000) 105.
8. P. Bourgeois et al., *Results of the PMT sector test at Saclay*, BaBar DIRC note 116, January 1999.
9. P. Bourgeois et al., *The light generator crate of the DIRC calibration system*, BaBar DIRC note 118, March 1999.
10. P. Bourgeois et al., *Results of the tests of the optical fibers and the diffuser for the DIRC calibration system*, BaBar DIRC note 119, March 1999.
11. T. Wright, ETL, private communication.
12. R. McAlpine, ETL technical Director, private communication.
13. A. Hoecker, *http://www.slac.stanford.edu/~hoecker/plots/nphot_bhabha.gif*.
14. D. Aston, BaBar *Hypernews note #986*, September 22, 2000.
15. S. Mine, K2K experiment, KEK, Japan, private communication.
16. J. Va'vra, *BaBar Hypernews note #700*, December 18, 1999.
17. Esso Flyckt, Photonis, private communication.